学位論文

Spectroscopic studies of the electronic structures of 122-type superconductors and ferromagnetic semiconductors

(122 型超伝導体および強磁性半導体の電子構造の分光研究)

平成 27 年 12 月博士（理学）申請

東京大学大学院理学系研究科

物理学専攻

鈴木　博人

Abstract

Iron-based superconductors (FeSCs) which exhibit the highest transition temperature (T_c) of $\sim$ 55 K have been extensively studied since their discovery in 2008. In spite of the fact that all the FeSCs share the iron-pnictide/chalcogenide planes like the CuO_2 planes in the cuprates, the T_c's and the superconducting gap structures differ between materials and dopants. In particular, superconductors with line nodes in the superconducting gap have attracted much attention. Nodal superconductivity in FeSCs is unconventional in that the presence of line nodes is determined not only by the symmetry of the order parameter but also by sign change of the s-wave order parameter under the C_4 point-group symmetry.

$BaFe_2(As_{1-x}P_x)_2$ (Ba122P), an isovalently-substituted FeSC, exhibits evidence for quasiparticle excitations well below T_c from various experimental probes including penetration depths, nuclear magnetic resonance, and thermal conductivity. Since the discovery, the identification of the nodal superconducting gap structure has been the central focus of FeSC research. However, a consensus has not been reached because of mutually inconsistent experimental results. To gain further insight into the nodal superconductivity in the P-doped 122 compounds and consequently to solve the dispute on Ba122P, we have performed angle-resolved photoemission spectroscopy study of the three-dimensional gap structure of $SrFe_2(As_{1-x}P_x)_2$ (Sr122P) in Chap. 3. Reflecting the smaller atomic radius of Sr than Ba, Sr122P has a more three-dimensional electronic structure along the k_z direction. We observed that, while the three hole Fermi surfaces (FSs) show orbital-dependent superconducting gaps, the electron FSs show almost isotropic and k_z-independent superconducting gaps. We conclude that there exists a sign change around the Z-X line on the outer hole FS around the Z point, which leads to the presence of line nodes. We also found that the spectral weight of the coherence peak is the largest for the inner hole FS.

Chapter 4 is devoted to time- and angle-resolved photoemission spectroscopy (TrARPES) of the parent compound $BaFe_2As_2$. $BaFe_2As_2$ exhibits stripe-type spin-density- wave (SDW) antiferromagnetic (AFM) order at the Neél temperature (T_N) of 138 K. Below T_N, the band structure of the paramagnetic state is folded by the ordering vector $(\pi/a, \pi/a, 2\pi/c)$. Our motivation is to optically excite the AFM ordered state by a pump pulse at a low temperature and to search for an ultrafast phase transition to the paramagnetic states and subsequent relaxation back to the SDW state. For this purpose, we have employed a new TrARPES apparatus that utilizes the rare-gas higher harmonic generation with photon energy $h\nu$ in the vacuum ultraviolet regime. We observed electronic modifications from the folded band

structure within $\sim$ 1 ps after the pump pulse, which we interpret as the melting of SDW.

Chapter 4 is devoted to soft x-ray spectroscopic studies of a new diluted magnetic semiconductor (DMS) which has the same crystal structure as the Ba122-type FeSC. DMSs have attracted much attention as a candidate for future spintronics devices after the discovery of ferromagnetism in Mn-doped GaAs (GaMnAs). However, the limited chemical solubility of the magnetic element Mn and the uncontrollability of the carrier density independently of the magnetic element concentration are major obstacles to systematic material design.The newly-found DMS $Ba_{1-x}K_x(Zn_{1-y}Mn_y)_2As_2$, which has the same crystal structure as the FeSC $BaFe_2As_2$, circumvents these problems and realizes the ferromagnetic transition temperature as high as 230 K and, therefore, understanding its basic electronic structure has been highly desired. In the latter half of this thesis, I have studied the electronic properties by soft x-ray spectroscopies.

First, I show by x-ray absorption and resonance photoemission spectroscopy that the doped Mn has the valence of 2+ and that the Mn $3d$ partial density of states has greatly similarity to that of GaMnAs. Ferromagnetic correlation between $S = 5/2$ local magnetic moments mediated by hole carriers is therefore considered to create ferromagnetism. In addition, I present soft x-ray angle-resolved photoemission spectroscopy (ARPES) of $Ba_{1-x}K_x(Zn_{1-y}Mn_y)_2As_2$ single crystals. Due to the longer probing depth of soft rays than vacuum-ultraviolet light, we have successfully observed bulk band dispersions. Also, by tuning the photon energy to the Mn L_3 edge, we selectively enhanced Mn $3d$-related electronic states, and found that the Mn $3d$ impurity band is formed below the Fermi level as in GaMnAs. On the other hand, the metallic transport may predominantly occur in the host valence band, rather than in the impurity band as in GaMnAs.

Second, I present x-ray magnetic circular dichroism (XMCD) and resonant inelastic x-ray scattering (RIXS) studies using Mn $L_{2,3}$ edge. XMCD directly reveals the spin and orbital magnetic moments by the application of spectral sum rules. RIXS reveals electronic excitations of the Mn impurity. We observed ferromagnetic XMCD signals with the spin moment of $0.45\mu_B$/Mn and the nearly quenched orbital moment of $0.05\mu_B$/Mn. However, the line shape is typical of the high-spin configurations of d^5. These results indicate the presence of competing antiferromagnetic and ferromagnetic interactions between Mn local spins. RIXS spectra show broad peaks from 6 eV to 1 eV in energy loss which originate from d-d orbital excitations from the ground states. From the comparison with the RIXS spectra of GaMnAs, we conclude that both the pure $3d^5$ and charge-transferred $3d^5\underline{L}$ electron configurations constitute the ground state of Mn in $Ba_{1-x}K_x(Zn_{1-y}Mn_y)_2As_2$.

Our studies have thus explicitly demonstrated that the $ThCr_2Si_2$-type crystal structure with chemical flexibility is an ideal stage both for high-temperature super-

conductivity and for carrier-induced ferromagnetism.

Contents

Chapter 1

Introduction

1.1 Iron-based superconductors

1.1.1 Iron-based superconductor family

The discovery in 2008 of superconductivity in Fe-based pnictides [1] was among the most significant breakthroughs in condensed matter physics during the past decade. Major efforts by the condensed matter community have been devoted in the few years to the understanding of the normal state properties of these materials, the superconducting pairing mechanism, and the symmetry and structure of the pairing gap.

The family of Fe-based superconductors (FeSCs) is already quite large and keeps growing. Fig. 1.1 shows the crystal structures of Fe-based superconductors. It includes various types of materials: 11-type Fe-chalcogenides $FeTe_{1-x}Se_x$, 111 systems such as LiFeAs, 1111 systems RFeAsO (R=rare earth element), 122 systems XFe_2As_2 (X=alkaline earth metals). The key ingredient for superconductivity is a quasi-two-dimensional layer consisting of a square lattice of iron atoms with tetrahedrally coordinated bonds to either phosphorus, arsenic, selenium or tellurium anions that are staggered above and below the iron lattice.

Long-range antiferromagnetic (AFM) order is also shared in the parent compounds of FeSCs. As shown in Fig. 1.1 (b), the iron sublattice undergoes a stripe-type AFM ordering. This AFM state is termed as spin-density-wave (SDW) state, due to the metallic transport of the system. The finding of the SDW states came from the neutron scattering experiments. Figure 1.2 shows the temperature dependence of squared magnetic moment determined from elastic neutron scattering profile at $\boldsymbol{Q} = 1.53$ Å^{-1} of LaFeAsO, which corresponds to the AFM ordering vector [3]. The power-law temperature dependence demonstrates the second-order AFM phase transitions, and the saturated magnetic moment per Fe is $\sim 0.35\ \mu_B$. While the structural transition occurs at 150 K, the Neel temperature is 138 K. In

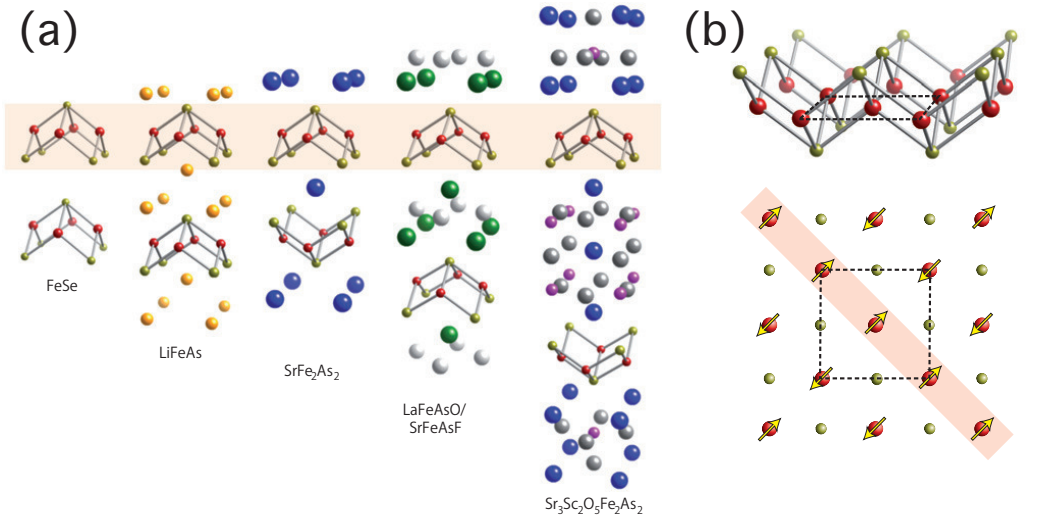

Figure 1.1: Crystallographic and magnetic structures of iron-based superconductors [2]. (a) Five tetragonal structures on which superconductivity emerges. (b) Fe-As layer shared among iron-based superconductors. Dashed line indicates the size of the unit cell, which includes two iron atoms due to the staggered pnictogen/chalchogen positions. The ordered spin arrangement in FeAs-based materials is indicated by arrows.

the orthorhombic state, the distance between the iron atoms with ferromagnetially aligned nearest-neighbour spins shortens by approximately 1% as compared with that of the perpendicular direction.

Superconductivity emerges by carrier doping to the SDW parent compound. Figure 1.3 shows the phase diagrams of $LaFeAsO_{1-x}F_x$ [4] and $Ba(Fe_{1-x}Co_x)_2As_2$ [5]. F doping to LaFeAsO and Co doping to $BaFe_2As_2$ introduce additional electrons. In the underdoped side, the tetragonal-to-orthorhombic lattice distortion proceeds the SDW magnetic ordering upon cooling. When the SDW order is suppressed, SC domes appear. In $Ba(Fe_{1-x}Co_x)_2As_2$ ($0.04 < x < 0.06$), there is a region where SDW and superconductivity coexist.

Because of the combination of strong bonding between Fe-As sites, the geometry of the $FeAs_4$ tetrahedra plays a crucial role in determining the electronic and magnetic properties of these systems. For instance, the As-Fe-As tetrahedral bond angle is an important parameter for optimizing T_c: the optimal T_c are found when this geometry is close to that of regular tetrahedron $\sim$109.47° [6].

The spin dynamics in the SC state was studied by inelastic neutron scattering. Fig. 1.4 (a) shows the imaginary part of the spin susceptibility $\chi''(\boldsymbol{q}, \omega)$ of $Ba(Fe_{1.85}Co_{0.15})_2As_2$ in the SC state ($T = 4$ K) and the normal states ($T = 60$ and 280 K) [7]. In the normal state (60 K), broad spectrum of $\chi''(\boldsymbol{q}, \omega)$ with its peak at 20 meV is observed, and it has a linear ω dependence for $\omega \to 0$. In the higher

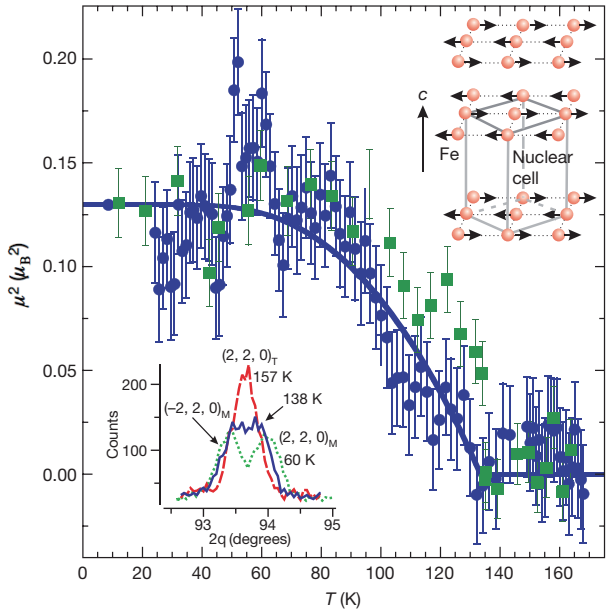

Figure 1.2: (a) Temperature dependence of order parameter of LaFeAsO at $\boldsymbol{Q} = 1.53$ Å^{-1} determined by neutron scattering. Figure reproduced from Ref. [3].

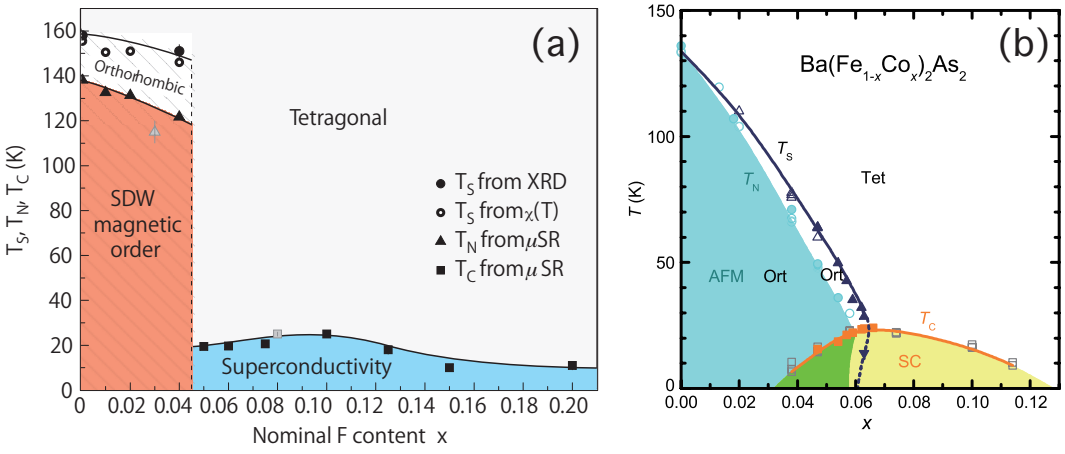

Figure 1.3: (a) Phase diagram of $LaFeAsO_{1-x}F_x$ [4]. Magnetic and superconducting transition temperatures are determined by μSR experiments. (b) Phase diagram of $Ba(Fe_{1-x}Co_x)_2As_2$ [5].

temperature 280 K, the intensity is suppressed and $\chi''(\boldsymbol{q},\omega)$ does not show a peak below 30 meV. In the superconducting state (6 K), we observe the redistribution of spectral weight to $\hbar\omega_{\text{res}} = 9.5$ meV, which is smaller than the SC gap 2Δ. This mode is called "resonance peak", whose intensity is determined by the coherence factors in the superconducting gap. An anomaly at T_c observed in the temperature dependence of this peak intensity [Fig. 1.4 (b)] demonstrates that the peak is related to superconductivity. While the resonance mode is a consequence of the gap opening and not in itself an evidence of the magnetic pairing mechanism, it imposes an restriction on microscopic theoretical models.

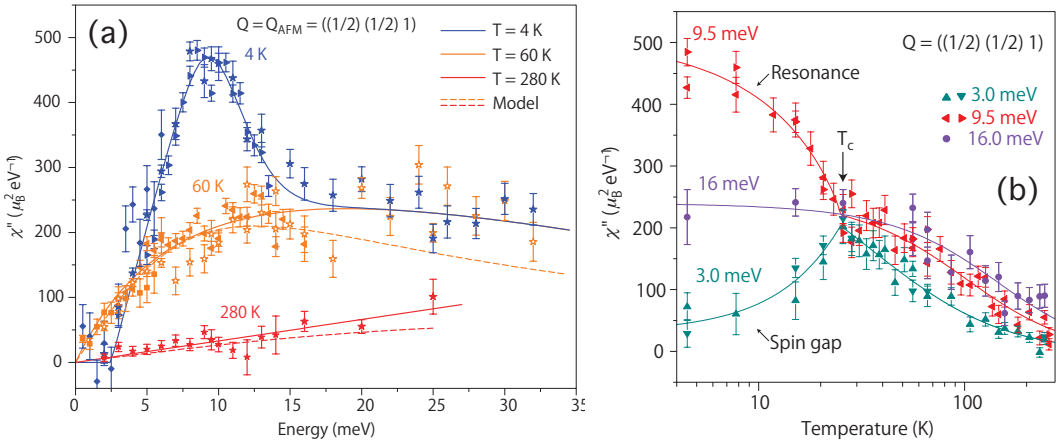

Figure 1.4: (a) The imaginary part of the dynamical spin susceptibility $\chi''(\boldsymbol{q},\omega)$ determined by inelastic neutron scattering. (b) Temperature dependence of $\chi''(\boldsymbol{q},\omega)$ at three different energies: within the spin gap (3 meV), the resonance energy (9.5 meV) and above 2Δ (16 meV). Figures reproduced from Ref. [7].

1.1.2 Symmetry of order parameter and proposed microscopic pairing mechanisms in iron-based superconductors

The pair wave function of the superconductors $\Phi(\boldsymbol{r}_1\alpha, \boldsymbol{r}_2\beta)$ must be antisymmetric under the exchange of its arguments due to the Fermi statistics. In the singlet pairing, it is decomposed into the form $\Phi(\boldsymbol{r}_1\alpha, \boldsymbol{r}_2\beta) = (i\sigma_y)_{\alpha\beta}\Delta(\boldsymbol{r}_1, \boldsymbol{r}_2)$, and the orbital part $\Delta(\boldsymbol{r}_1, \boldsymbol{r}_2)$ becomes symmetric with respect to $\boldsymbol{r}_1$ and $\boldsymbol{r}_2$. In other words, $\Delta(\boldsymbol{R}, \boldsymbol{r}) = \Delta(\boldsymbol{R}, -\boldsymbol{r})$, where $\boldsymbol{R} = \frac{\boldsymbol{r}_1+\boldsymbol{r}_2}{2}$ is the center-of-mass coordinates and $\boldsymbol{r} = \boldsymbol{r}_1 - \boldsymbol{r}_2$ is the relative coordinates. In the momentum space, the parity of $\Delta(\boldsymbol{k})$ is even: $\Delta(\boldsymbol{k}) = \Delta(-\boldsymbol{k})$.

Further, the gap function $\Delta(\boldsymbol{k})$ must correspond to an irreducible representation of the space group of the crystal lattice, or to a superposition of irreducible representation of the form, e.g. "$s + id$". If one neglects the staggering As atoms that do not have significant contribution to the electronic states near E_F, the Fe atoms

form a square lattice and the local symmetry group is C_{4v}. The primitive transformations are (a) $\pi/2$ rotations about the (001) (z-)axis ($R_{\pi/4}$), (b) reflections with the xz ($y = 0$) plane (I_{xz}), and (c) reflections with the diagonal ($x = y$) plane ($I_{x=y}$). One-dimensional irreducible representations of C_{4v} group with even parity are summarized in Table 1.1. Note that the representative states only reflect the behavior under the operations of the C_{4v} group.

Table 1.1: Even-parity irreducible representations of the C_{4v} group.

Informal name	Notation	$R_{\pi/4}$	I_{xz}	$I_{x=y}$	Representative state
s	A_{1g}	$+1$	$+1$	$+1$	const.
g	A_{2g}	$+1$	-1	-1	$xy(x^2-y^2)$
$d_{x^2-y^2}$	B_{1g}	-1	$+1$	-1	x^2-y^2
d_{xy}	B_{2g}	-1	-1	$+1$	xy

We consider the gap function in the FeSCs where hole pockets are at the zone center and electron pockets are at the zone corner. Here for simplicity we ignore the superposition of irreducible representations since there are only a few experimental evidences for the superposition states in few materials (e.g. $Ba_{1-x}K_xFe_2As_2$). Then $\Delta(\boldsymbol{k})$ belongs to one of the irreducible representations listed above. Figure 1.5 shows a schematic illustration of proposed gap symmetries that seem to be relevant in FeSCs. They belong either to the A_{1g} representation ("s-wave") or the B_{1g} representation ("d-wave"). All of the cases (a)-(d) belong to the A_{1g} symmetry. Panel (a) shows the s_{++} wave, where both hole and electron FSs have positive gap. Panel (b) shows the $s_{\pm}$ wave, where the order parameter changes sign between the hole and electron sheets. Both s_{++} and $s_{\pm}$ wave have fully-opened gap, which limit the low-temperature quasiparticle excitations. Panel (c) shows the nodal s_{++} wave. Here, the case where there is fully-opened gap on the hole sheet is sketched. SC gap nodes appear on the electron sheets as a result of anisotropy with in the pockets, and the average gap on them is positive. The nodal $s_{\pm}$ wave shown in panel (d) differs only quantitatively from the nodal s_{++} wave; the average of the SC gap on the electron sheets is negative. The nodes on (c) and (d) result from the qualitative details of the pairing interactions, and are not protected by the symmetry. Panel (e) shows the B_{1g} symmetry (d wave). The sign change under the $I_{x=y}$ operation in B_{1g} symmetry dictates that sign change occurs on the hole FS (symmetry-protected nodes).

Soon after the discovery of $LaFeAsO_{1-x}F_x$, several microscopic models have been proposed. Mazin *et al.* [8] pointed out that the superconductivity in $LaFeAsO_{1-x}F_x$ not only is unconventional but shows a sign change between the multiple FS sheets. Figure 1.6 shows the imaginary and real parts of the noninteracting susceptibility $\chi_0(q,\omega) = \frac{f(\epsilon_k)-f(\epsilon_{k+q})}{\epsilon_k-\epsilon_{k+q}-\omega-i\delta}$ at $\omega \to 0$ and $q_z = \frac{\pi}{c}$ from Ref. [8]. $\mathrm{Re}\chi$, which con-

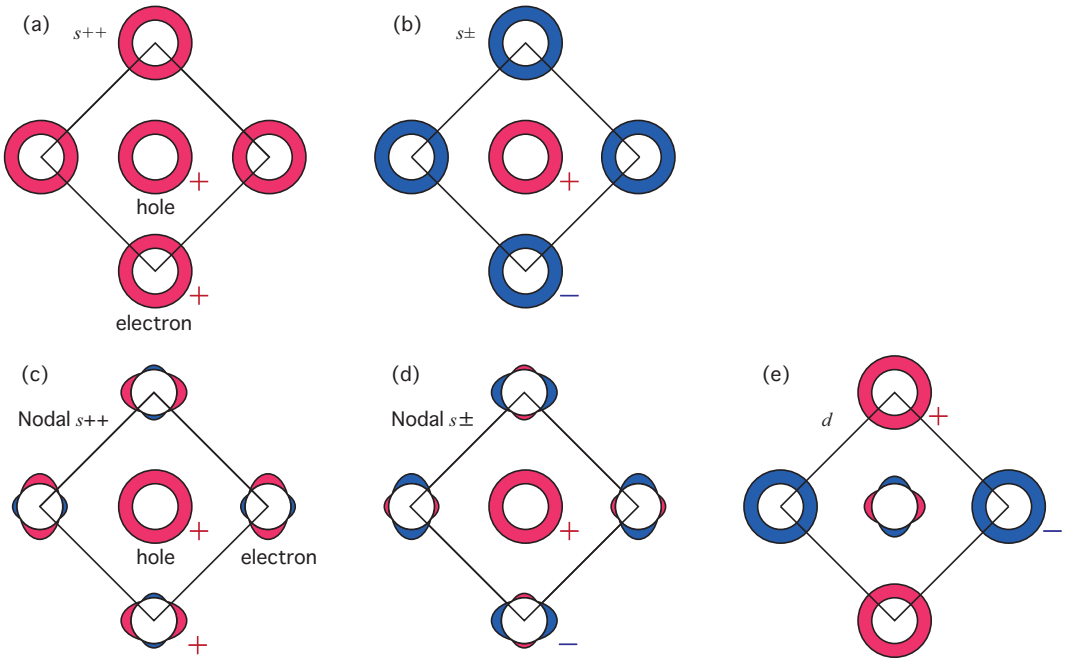

Figure 1.5: Schematic illustration of proposed gap structures in iron-based superconductors with hole pockets at the zone center and electron pockets at the zone corner. The figures are drawn in the unfolded 1-Fe Brillouin zone. (a) s_{++} wave. (b) $s_{\pm}$ wave. (c) Nodal s_{++} wave. Nodes appear on the electron sheets, and the average of the gap function on the electron sheets is positive. (d) Nodal $s_{\pm}$ wave. The average of the gap function is negative. (e) d wave.

trols the pairing interactions, has a strong but broad peak near the M point in the Brillouin zone (BZ) originating from antiferromagnetic spin fluctuations.

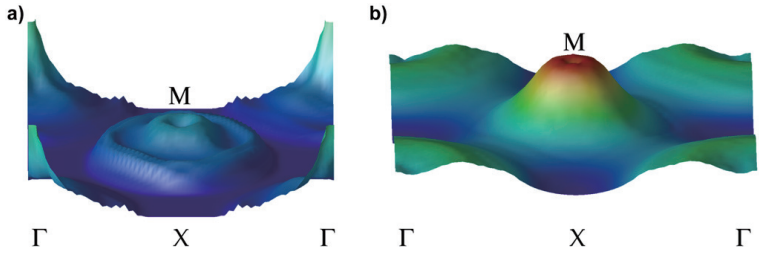

Figure 1.6: The imaginary [(a)] and real [(b)] parts of the noninteracting susceptibility $\chi_0(q, \omega \to 0)$ reproduced from Ref. [8].

Almost simultaneously, Kuroki *et al.* [9] constructed a minimal five-band model

of $LaFeAsO_{1-x}F_x$. The many-body Hamiltonian reads

$$\begin{aligned} H = & \sum_i \sum_\mu \sum_\sigma \varepsilon_\mu n_{i\mu\sigma} + \sum_{ij} \sum_{\mu\nu} \sum_\sigma t_{ij}^{\mu\nu} c_{i\mu\sigma}^\dagger c_{j\mu\sigma} \\ & + \sum_i \Big(U \sum_\mu n_{i\mu\uparrow} n_{i\mu\downarrow} + U' \sum_{\mu>\nu} \sum_{\sigma,\sigma'} n_{i\mu\sigma} n_{i\nu\sigma'} \\ & - J \sum_{\mu\neq\nu} \boldsymbol{S}_{i\mu} \cdot \boldsymbol{S}_{i\mu} + J' \sum_{\mu\neq\nu} c_{i\mu\uparrow}^\dagger c_{i\mu\downarrow}^\dagger c_{i\mu\downarrow} c_{i\mu\uparrow} \Big), \end{aligned} \tag{1.1}$$

where i, j denote the sites and μ, ν the orbitals of Fe $3d$. The parameters ε_μ and $t_{ij}^{\mu\nu}$ are constructed by forming maximally-localized Wannier functions from the density-functional band structure of $LaFeAsO_{1-x}F_x$. For the interaction terms, they took the intraorbital Coulomb $U = 1.2$ eV, the interorbital Coulomb $U' = 0.9$ eV, the Hund's coupling $J = 0.15$ eV, and the pair-hopping $J' = 0.15$ eV. The band structure and FSs of the model are shown in Fig. 1.7 (a) and (b), respectively. The band structures near E_F comprise all the five Fe $3d$ orbitals and thus the inclusion of all the Fe $3d$ orbitals is necessary. Two holelike bands around the (0,0) point form two concentric FSs and electron ones are formed at the $(\pi, 0)$ and $(0, \pi)$ points. They calculated the susceptibility within the random-phase approximation (RPA) as shown in Fig. 1.7 (c). Compared with the noninteracting susceptibility in Fig. 1.6 (b), the peak at $(\pi, 0)$, which originates from the nesting between the α and β_1 FS sheets, is enhanced by the RPA treatment. To evaluate the gap function in the SC state, one has to solve the linearized Eliashberg equation,

$$\lambda \phi_{l_1 l_4}(k) = -\frac{T}{N} \sum_q \sum_{l_1 l_2 l_3 l_4} V_{l_1 l_2 l_3 l_4}(q) G_{l_2 l_5}(k-q) \phi_{l_5 l_6}(k-q) G_{l_3 l_6}(q-k), \tag{1.2}$$

where ϕ_{lm} is the 5×5 matrix gap function and $G(k)$ is the electronic Green's function [10]. The eigenvalue λ is taken as the measure of the strength of the SC instability. Here, the effective singlet pairing interaction is expressed as

$$\hat{V}^s(q) = \frac{3}{2} \hat{S} \hat{\chi}_s(q) \hat{S} - \frac{1}{2} \hat{C} \hat{\chi}_c(q) \hat{C} + \frac{1}{2} (\hat{S} + \hat{C}), \tag{1.3}$$

where

$$S_{l_1 l_2 l_3 l_4} = \begin{cases} U, & l_1 = l_2 = l_3 = l_4 \\ U', & l_1 = l_3 \neq l_2 = l_4 \\ J, & l_1 = l_2 \neq l_3 = l_4 \\ J' & l_1 = l_4 \neq l_2 = l_3 \end{cases}$$

and

$$C_{l_1 l_2 l_3 l_4} = \begin{cases} U, & l_1 = l_2 = l_3 = l_4 \\ -U' + J, & l_1 = l_3 \neq l_2 = l_4 \\ 2U' - J, & l_1 = l_2 \neq l_3 = l_4 \\ J' & l_1 = l_4 \neq l_2 = l_3. \end{cases}$$

Kuroki *et al.* [9] found that the spin fluctuations (the first term in eq. (1.3)) dominate over the orbital fluctuations (the second term) as long as $U > U'$ and focused on the spin susceptibility. By plugging the spin susceptibility into eq. (1.3) and solving eq. (1.2), they obtained the gap functions ϕ_3 (d_{YZ}) and ϕ_4 ($d_{X^2-Y^2}$) as shown in Figs. 1.7 (d) and (e), respectively. The solutions are basically s wave, but change sign between α_1 and β_1/β_2 FSs across the nesting vectors along $(0, \pi)$ and $(\pi, 0)$.

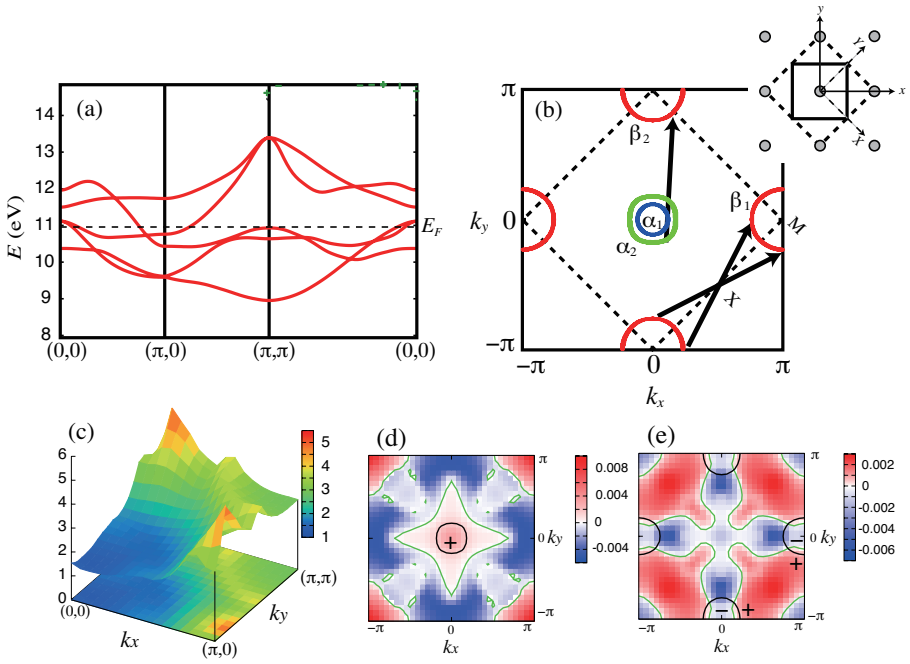

Figure 1.7: (a) Band structure of the five-band model of $LaFeAsO_{1-x}F_x$ in the unfolded Brillouin zone (BZ). (b) Fermi surfaces (FSs) of the five-band model for the filling factor $n = 6.1$. (c) Spin susceptibility χ_s within the random phase approximation (RPA). (d), (e) Gap functions for the d_{YZ} [(d)] and $d_{X^2-Y^2}$ [(e)] orbitals, respectively. Figures reproduced from Ref. [9].

Kuroki *et al.* further performed five-band model calculations on various crystal structures. They have found that the pnictogen height from the Fe square lattice (h_{Pn}) can serve as a possible switch between high-T_c nodeless and low-T_c nodal pairings [11]. Figure 1.8 (a) shows the eigenvalue of the Eliashberg equation as a function of the internal coordinate of the pnictogen atom z_{As} and h_{As}. z_{As} and h_{As} are related by $h_{As} = (z_{As} - 0.5) \times c$. For $h_{As} > 0.65$ Å, nodeless s-wave solutions are more stable than d-wave solutions. On the other hand, for $h_{As} > 0.64$ Å, the s-wave solutions become nodal and the eigenvalues of s and d-waves are almost the same. The monotonic increase of λ demonstrates that the large h_{As} gives rise to high-T_c nodeless pairing while small h_{As} leads to low-T_c nodal pairings. The corresponding gap functions for the s- and d-wave are plotted in Figs. 1.8 (b) and (c). For the s-wave solution, the gap function for $z_{As} = 0.658$ is fully-gapped,

whereas nodes are formed on the electron FS (band 4) for $z_{As} = 0.6304$. For the d-wave solutions, the symmetry determines that nodes appear on the diagonal line on the hole FS (band 3) around the (0,0) point, and the FS around (π, π) point for $z_{As} = 0.658$.

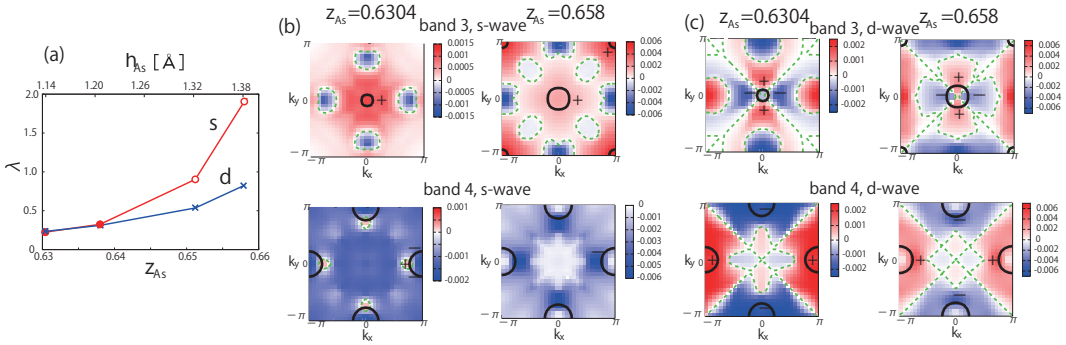

Figure 1.8: (a) s-wave and d-wave eigenvalues of the Eliashberg equation as a function of z_{As} or h_{As}. Open (solid) circles for s-wave indicate that the gap is nodeless (nodal). (b) s-wave gap functions for the model with $z_{As} = 0.6304$ and $z_{As} = 0.658$ for the filling factor $n = 6.1$. (c) d-wave gap functions. Figures reproduced from Ref. [11].

Although the pairing mechanisms based on antiferromagnetic spin fluctuation exchange have successfully explain experimental results, there still are discrepancies for the $s_{\pm}$-wave state. For example, isovalently-substituted materials $BaFe_2(As_{1-x}P_x)_2$ [12] and $SrFe_2(As_{1-x}P_x)_2$ [13] have relatively high T_c's exceeding 30 K with signatures of line nodes in the SC gap, as we will see below. Also, the $s_{\pm}$-wave is expected to be fragile against nonmagnetic impurities due to interband impurity scattering [14, 15]. However, there are reports suggesting that FeSCs are relatively robust against impurities [16]. These facts indicate that the s-wave state without sign reversal can also be a candidate for iron pnictides.

Kontani *et al.* [17] have proposed that the electron-phonon interaction due to the Fe-ion oscillation can induce significant orbital fluctuations and these fluctuations give rise to the strong pairing interaction for the s-wave SC state without sign reversal. The Coulomb potential for a d electron at $\boldsymbol{r}$ from the tetrahedrally surrounding As^{3-} ions is given by

$$U^{\pm}(\boldsymbol{r};\boldsymbol{u}) = 3e^2 \sum_{s=1}^{4} |\boldsymbol{r} + \boldsymbol{u} - \boldsymbol{R}_s^{\pm}|^{-1}, \tag{1.4}$$

where $\boldsymbol{u}$ is the displacement vector of the Fe ion, and $\boldsymbol{R}_s^{\pm}$ is the location of the As^{3-} ions around the Fe 1 (2) ion in the unit cell. The $\boldsymbol{u}$-linear term, which gives rise to the electron-phonon interaction, is expressed as

$$V^{\pm}(\boldsymbol{r};\boldsymbol{u}) = \pm A[2XZu_X - 2YZu_Y + (X^2 - Y^2)u_Z] + O(\boldsymbol{r}^4), \tag{1.5}$$

where $A = 30e^2/\sqrt{3}R^4_{\text{Fe-As}}$. Denoting the Z^2, XZ, YZ, X^2-Y^2 and XY orbitals by 1, 2, 3, 4, 5, respectively, the nonzero matrix elements are obtained as

$$\begin{aligned}
&\langle 2|\, V\, |4\rangle = \pm 2a^2 A u_X/7, \langle 3|\, V\, |4\rangle = \pm 2a^2 A u_Y/7, \\
&\langle 2|\, V\, |2\rangle = \pm 2a^2 A u_Z/7, \langle 3|\, V\, |4\rangle = \mp 2a^2 A u_Y/7,
\end{aligned} \tag{1.6}$$

where a is the radius of the d orbital. The virtual exchange of phonons gives rise to the interaction between electrons in different orbitals. Both for Fe 1 and Fe 2, the phonon-mediated interaction is given by

$$\begin{aligned}
&V_{24,42} = V_{34,43} = (2Aa^2/7)^2 D(\omega_l) \equiv -g(\omega_l), \\
&V_{22,22} = V_{33,33} = -V_{22,33} = -g(\omega_l),
\end{aligned} \tag{1.7}$$

where $D(\omega_l) = \hbar/[M_{Fe}(\omega_l^2 + \omega_D^2)]$ is the phonon Green's function. This interaction enhances the interorbital scattering, which is less dominant in the Coulomb interaction [eq. (1.3)] under the condition $U > U'$.

Kontani *et al.* calculated U-$g(0)$ phase diagram as shown in Fig. 1.9 (a). By using the spin (charge) Stoner factor $\alpha_{s(c)}$, the largest eigenvalue of $\hat{S}\chi^0(\boldsymbol{q}, 0)$ ($\hat{C}\chi^0(\boldsymbol{q}, 0)$), the enhancement factor for $\chi^{s(c)}$ in RPA is expressed as $(1-\alpha_{s(c)})^{-1}$. As U increases, AFM spin fluctuation with the nesting vector $(\pi, 0)$ develops, leading to the $s^{\pm}$ pairing for $\alpha_s < 1$ [9]. On the other hand, as $g(0)$ increases, two different channels exhibit diverging behavior. Figures 1.9 (b) and (c) show the $\chi^c_{ll',mm'}$ for $(ll', mm') = (24, 42)$ and $(22, 22)$, respectively. The former possesses the broad peak around $\boldsymbol{q} = (0, 0)$. This ferro-orbital fluctuations would bring about the softening of the shear modulus [18] and reinforce the ferro-orbital ordering below T_s. The latter is peaked around $(\pi, 0)$, which is induced by multiple scattering along the nesting vector. In the presence of strong orbital fluctuations and when U is small, the s^{++} wave is realized for $\alpha_c < 1$.

As another mechanism of the enhancement of the orbital fluctuations, Onari *et al.* [19] proposed the importance of vertex corrections to the susceptibilities, which are neglected in the RPA treatment. They studied the role of vertex corrections due to the Maki-Thompson and Aslamazov-Larkin (AL) type diagrams. Figure 1.10 shows $\chi^c_{xz}(\boldsymbol{q})$ and $\chi^c_{x^2-y^2}(\boldsymbol{q})$ obtained by self-consistent vertex correction (SC-VC) and RPA for three parameter sets. Compared with RPA, the antiferro-orbital fluctuations at $(\pi, 0)$ in $\chi^c_{xz}(\boldsymbol{q})$ and the ferroorbital fluctuations at $(0, 0)$ are strongly enhanced by the AL term. This result suggests that the orbital fluctuations can play as important a role as spin fluctuations even in the case $U > U'$, and material-specific gap functions can emerge as a result of a competition between spin- and orbital-fluctuations.

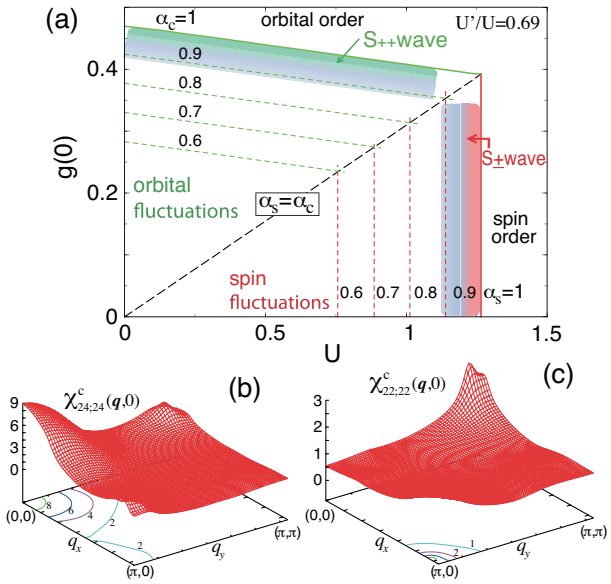

Figure 1.9: (a) U-$g(0)$ phase diagram. (b), (c) $\chi^c_{24,42}$ [(b)] and $\chi^c_{22,22}$ [(c)] for $\alpha_c = 0.97$. Figures reproduced from Ref. [17].

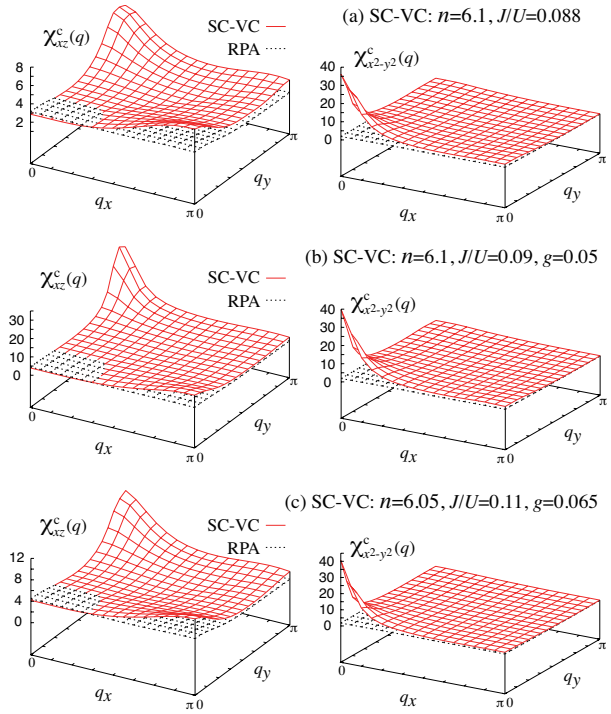

Figure 1.10: $\chi^c_{xz}(\boldsymbol{q})$ and $\chi^c_{x^2-y^2}(\boldsymbol{q})$ obtained by self-consistent vertex correction (SC-VC) and RPA for three parameter sets. Figures reproduced from Ref. [19].

1.1.3 Nodal superconductivity in phosphorous-doped 122 compounds

Superconductivity in FeSCs can also be induced by isovalent substitution of elements in the parent compounds. Here I review physical properties of two phosphorous-doped 122 compounds, $BaFe_2(As_{1-x}P_x)_2$ (Ba122P) and $SrFe_2(As_{1-x}P_x)_2$ (Sr122P), which have attracted attention as nodal superconductors. The investigation into the three-dimensional gap structure of Sr122P in connection with reported data for Ba122P is the main focus of the present thesis.

Figure 1.11 (a) shows the resistivity curves $\rho_{xx}(T)$ of Ba122P with different doping concentrations. The anomaly of $x = 0$ at 137 K corresponds to the structural phase transition (T_0) of the parent compound of $BaFe_2As_2$. With increasing x, the room-temperature resistivity monotonically decreases and the anomaly is replaced by step increase at T_0 and a peak at T_N. For $0.2 < x < 0.7$, superconductivity sets in at lower temperatures with the maximum $T_c = 30$ K at $x = 0.3$, and the SDW and superconductivity coexist between $0.2 < x < 0.27$.

Figure 1.11 (b) shows the resitivity for $0.33 \leq x \leq 0.71$ at low temperatures. At $x = 0.33$, $\rho_{xx}(T)$ exhibits a T-linear dependence in a wide temperature range above T_c. In the Fermi-liquid theory, the resistivity has the temperature dependence of the form $\rho(T) = \rho_0 + AT^{\alpha}$ with $\alpha = 2$; therefore the linear-T behavior demonstrates a typical non-Fermi-liquid behavior. The Hall resistivity R_H of $x = 0.33$ has diverging behavior of the form $-R_H = A/T + B$, which also indicates the non-Fermi liquids. As x is increased, the power-law exponents change from 1 to 2 at $x = 0.71$, where a typical Fermi-liquid behavior is achieved.

The evolution of lattice parameters upon P doping is plotted in the upper panels of Fig. 1.11 (c). All of the a-axis, c-axis, and pnictogen height h_{pn} monotonically shorten with increasing x, reflecting the smaller atomic radius of P than As. Due to the isovalent nature of P and As, the reduction of the lattice parameter by P substation is often termed as "chemical pressure". The bottom panel shows the phase diagram of Ba122P. The SDW order is suppressed with P doping, and superconducting dome appears between $0.2 < x < 0.7$. The normal phase is colored by the exponent of the resistivity power law, α. From the color plot one observes the non-Fermi-liquid transport in the underdoped regime transforms to a typical Fermi-liquid in the overdoped regime.

P doping to $SrFe_2As_2$ also induces superconductivity. Figures 1.12 (a)-(h) show the normalized resistivity of Sr122P ($0 \leq x \leq 1$) [21]. ρ(300K) does not change by annealing process. Resistivity shows anomaly at the structural transition temperature for $x = 0, 0.10$ and 0.25, and superconducting transition has been observed for $0.25 \leq x \leq 0.60$. The annealing process raises the T_0 and T_c.

The phase diagram of Sr122P is shown in Fig. 1.12 (i) and the inset shows a

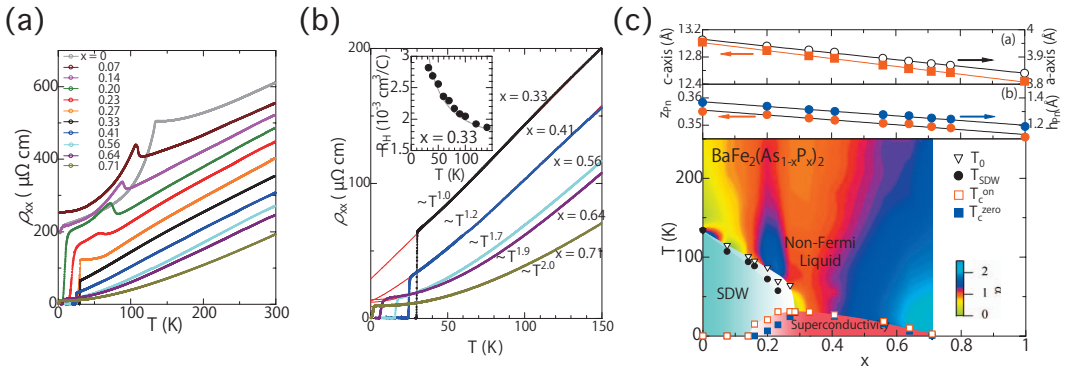

Figure 1.11: (a) DC resistivity of $BaFe_2(As_{1-x}P_x)_2$ for several doping levels x. (b) Low-temperature resisitivity for $x = 0.33, 0.41, 0.56, 0.64$, and 0.71. The red solid lines indicate the fits to power-law behavior. The Hall resistance $-R_H$ of $x = 0.33$ is shown in the inset. (c) Top panels: the evolution of crystal parameters. The a-axis, c-axis and the pnictogen height $h_{\rm pn}$ monotonically shrink with increasing x. Bottom panel: phase diagram of $BaFe_2(As_{1-x}P_x)_2$. The triangles shows the structural transition temperature T_0 and the black circles show the SDW transition temperature T_N. The onset of the superconducting transition $T_c^{\rm on}$ and the zero resistivity temperature $T_c^{\rm zero}$ are displayed by open- and closed-squares, respectively. The color in the background represent the power-law exponent estimated from the resistivity. Figures reproduced from Ref. [20].

comparison between Ba122P and Sr122P [21,22]. The T_N of the parent compound $SrFe_2As_2$ is 197 K, which is as much as 50 K higher than that of $BaFe_2As_2$, and T_N is higher in Sr122P than in Ba122P in the doping range $x < 0.3$, where AFM order is present. In the same way as Ba122P, superconductivity in Sr122P appears as the AFM order is suppressed by P substitution [23]. The T_c of Sr122P reaches up to 30 K (as grown) or 33 K (annealed) at $x = 0.35$ [24], which are comparable to, or higher than, $T_c = 30$ K of $BaFe_2(As_{0.7}P_{0.3})_2$. Superconductivity appears in the range $0.25 < x < 0.5$ for Sr122P, which is narrower than $0.13 < x < 0.74$ for Ba122P.

The three-dimensional electronic structures of Ba122P and Sr122P have been studied by angle-resolved photoemission spectroscopy (ARPES). Figure 1.13 shows the FSs and band dispersions of Ba122P ($x = 0.38$) [25]. Hole FS sheets at the zone center and the electron sheets at the zone corner are resolved. The change of the FSs between Γ and Z point indicates the three-dimensional electronc structure of Ba122P.

Suzuki *et al.* [26] studied the electronic structure of Sr122P ($x = 0.35$). In-plane Fermi surface mapping of Sr122P is shown in Figs. 1.14 (a) and (b). Sr122P has a space group symmetry of I4/mmm and its first Brillouin zone is shown in the inset of (a). There are three hole-like bands crossing E_F around the Z point [panel (c)], while two hole-like bands cross E_F around the Γ point [panel (e)]. There are

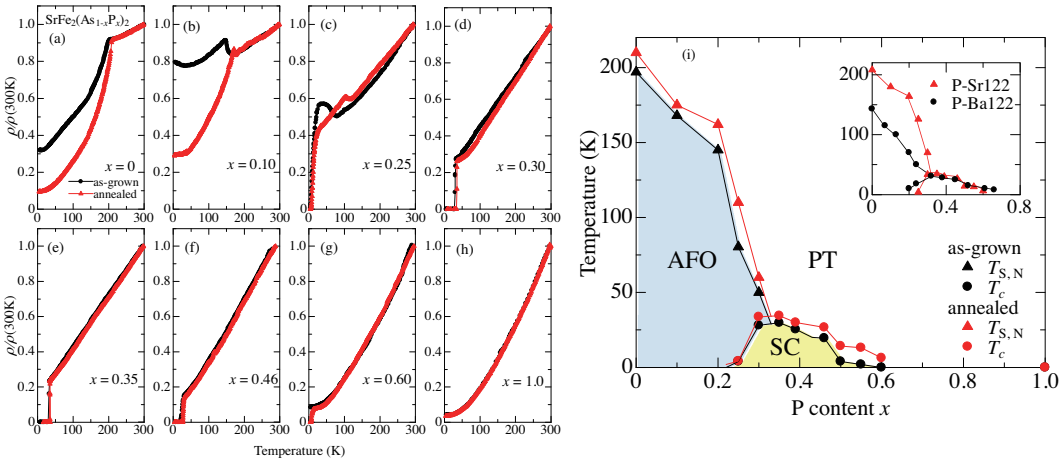

Figure 1.12: (a)-(h) Resistivity of as-grown and annealed $SrFe_2(As_{1-x}P_x)_2$ (Sr122P) ($0 \leq x \leq 1$). (i) Phase diagram of Sr122P. Phase diagrams of Ba122P and Sr122P are compared in the inset. Figures reproduced from Ref. [21].

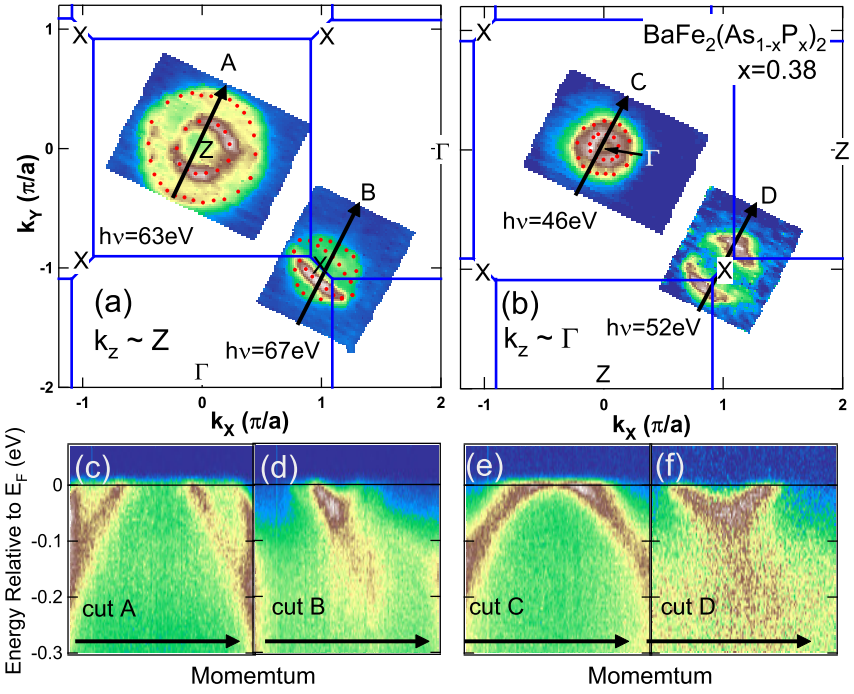

Figure 1.13: (Color online) (a),(b) In-plane Fermi surface (FS) mapping for Ba122P ($x = 0.38$) . Filled circles indicate the k_F positions. (c)-(f) ARPES intensity plot taken along the cuts shown in (a) and (b). Figures reproduced from Ref. [25].

two electron-like bands crossing E_F around the X point [panel (d)]. ARPES E-k intensity plots around high-symmetry cuts are shown in Figs. 1.14 (c)-(e). The peaks are fitted to parabolic dispersions of the form $E(\boldsymbol{k}) = E(0) + \frac{\hbar^2 k^2}{2m^*}$ and the quasiparticle mass m^*/m_e are also shown in the inset.

The intensity mappings along the k_z directions for Sr122P and Ba122P are compared in Fig 1.15 [26]. In Sr122P, the γ FS, which has strong d_{z^2} character around the Z point, shrinks rapidly as it approaches the Γ point. At the same time, the innermost α band shrinks and splits into two pockets. This is in contrast to that of Ba122P, in which all the hole FSs are connected in the entire k_z region. The stronger three-dimensionality in Sr122P originates from enhanced interlayer hopping matrix elements due to the smaller c-axis lattice constant. By examining nesting conditions between the hole and electron FSs, Suzuki *et al.* concludes that magnetic interactions between FeAs layers rather than FS nesting play an important role in stabilizing the antiferromagnetic order.

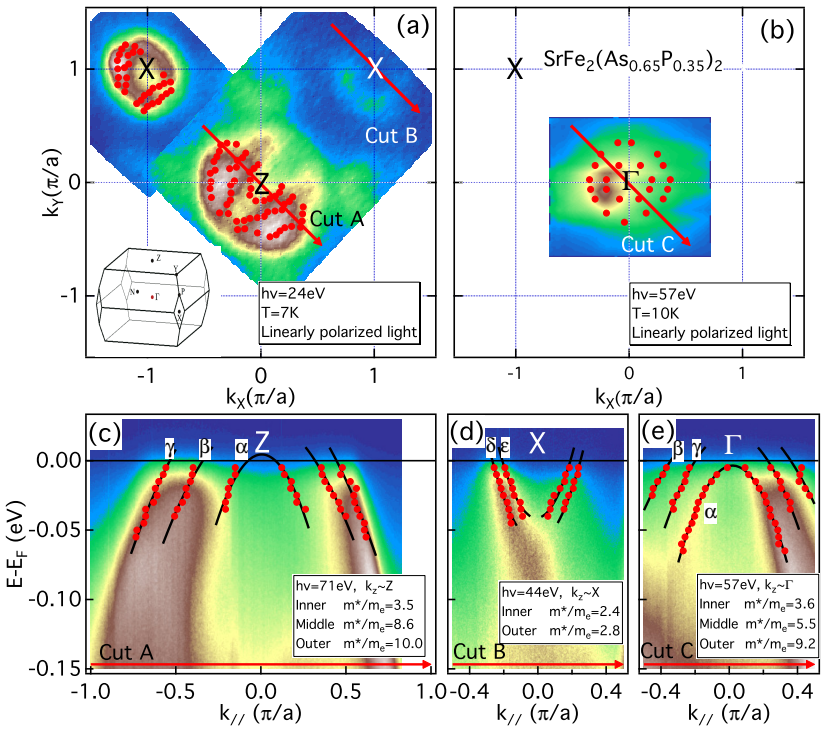

Figure 1.14: (a),(b) In-plane FS mapping for Sr122P ($x = 0.35$) taken at $h\nu = 24$ eV [(a)] and 57 eV [(b)]. Filled circles indicate the k_F positions. The first Brillouin zone of Sr122P is shown in the inset of panel (a). (c)-(e) ARPES intensity plot taken along the cuts shown in (a) and (b). Figures reproduced from Ref. [26].

The low-energy excitations in the superconducting state are reflected in the low-temperature penetration depth λ. λ is related to the superfluid density n_s through

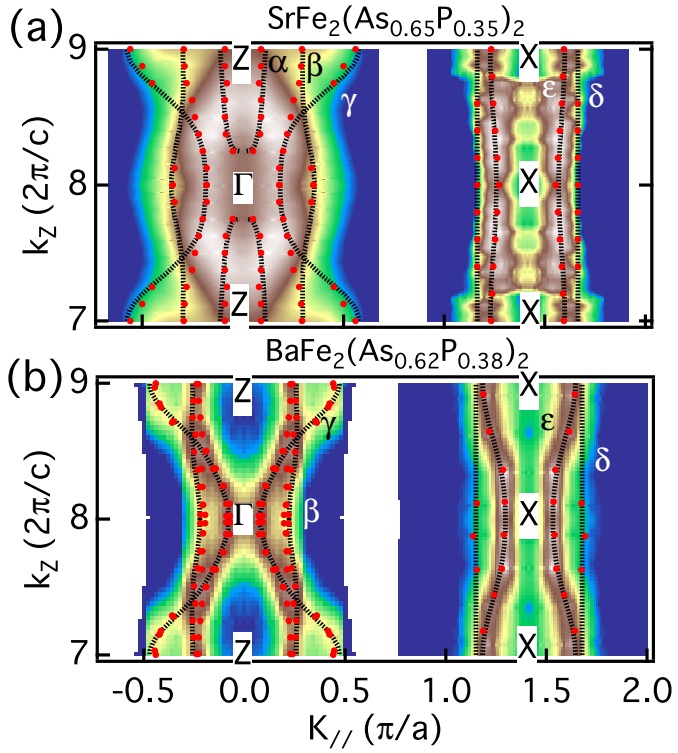

Figure 1.15: Fermi surface mapping taken in the k_z-$k_{\|}$ plane for Sr122P ($x = 0.35$) [(a)] and Ba122P ($x = 0.38$) [25] [(b)]. In Sr122P, the γ FS is warped more strongly than that of Ba122P and the α FS forms a 3D ellipsoidal hole pocket. The electron FSs ϵ and δ are less warped and nearly cylinder-like. Figures reproduced from Ref. [26].

$n_s \propto \lambda^{-2}$, and the temperature dependence of n_s is directly determined by the gap function. Figure 1.16 (a) shows the normalized change in the penetration depth of $BaFe_2(As_{0.67}P_{0.33})_2$ [27] with the data for $Ba_{0.45}K_{0.55}Fe_2As_2$ [28]. For $Ba_{0.45}K_{0.55}Fe_2As_2$, $\Delta\lambda(T)/\lambda(0)$ shows a flat behaviour up to $T = 6$ K, indicating a fully-gapped order parameter. In stark contrast, $\Delta\lambda(T)/\lambda(0)$ for $BaFe_2(As_{0.67}P_{0.33})_2$ exhibits a quasilinear temperature dependence at low temperatures. The linear-T dependence is a strong indication of line nodes in the order parameter. $\Delta\lambda$ values for $SrFe_2(As_{0.65}P_{0.35})_2$ for as-grown and annealed samples are shown in Fig. 1.16 (b). All the curves are well fitted by the functional form $\Delta\lambda = A\frac{t^2}{t^*+t}$, which connects the linear T-dependence to low-energy rounding off due to impurity scattering [29], suggesting line nodes in $SrFe_2(As_{0.65}P_{0.35})_2$ as well.

The indication of nodes in Ba122P and Sr122P has also been proposed from nuclear magnetic resonance (NMR) measurements. ^{31}P-NMR and ^{75}As-NMR spectra for as-grown and annealed Sr122P ($x = 0.35$) are compared in Figs. 1.17. The line shapes of annealed samples are narrower than those of as-grown ones, indicating better homogeneity and reduced defects in the annealed samples. Fig-

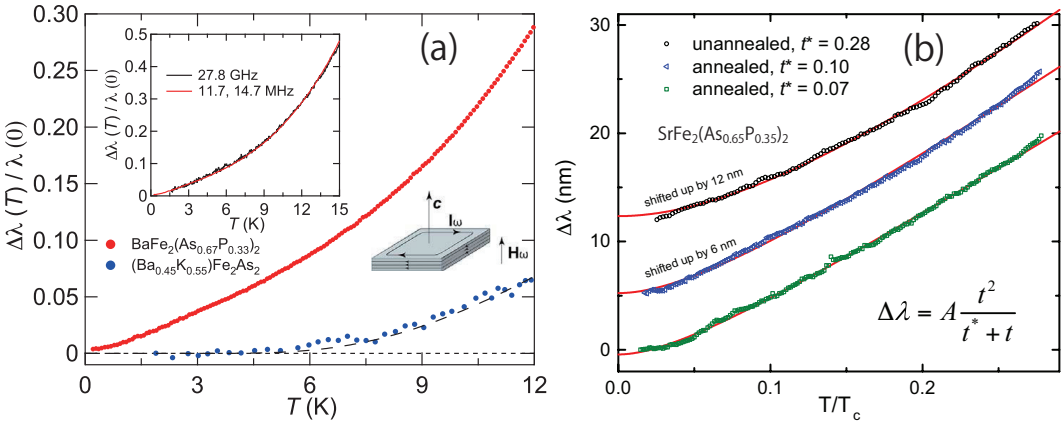

Figure 1.16: (a) The change in the penetration depth of $BaFe_2(As_{0.67}P_{0.33})_2$ from Ref. [27]. The data for $Ba_{0.45}K_{0.55}Fe_2As_2$ [28] is also plotted. (b) Change in the penetration depth in $SrFe_2(As_{0.65}P_{0.35})_2$ reproduced from Ref. [30].

ure 1.17 (c) shows $\sqrt{(1/T_1T)/(1/T_1T)_{T=T_c}} = N_{\rm res}/N_0$ plotted as a function of T/T_c in logarithmic scale, where T_1 is the nuclear spin-lattice relaxation time, N_0 is the density of state at E_F in the normal state, and $N_{\rm res}$ is the residual density of states in the superconducting state. The results for Ba122P ($x = 0.33$) [31] and $Ba_{0.6}K_{0.4}Fe_2As_2$ [32] are also plotted. For $Ba_{0.6}K_{0.4}Fe_2As_2$, the $1/T_1T$ shows a power-law T dependence and approaches zero at $T = 0$ even under strong magnetic field of 12 T, indicating fully-gapped SC order parameter. For Ba122P and Sr122P, the $1/T_1T$ approaches finite constants, indicative of superconductivity with nodes. The values for Sr122P are larger than that of Ba122P taken with lower magnetic field. As for the effect of annealing, $N_{\rm res}/N_0 = 0.72$ at 14 T for as-grown sample is reduced to $N_{\rm res}/N_0 = 0.56$ at 11.95 T for annealed ones. This reduction can be attributed the removal of lattice defects that have finite density of states at E_F. The increase of T_c by the removal of nonmagnetic impurity is consistent with the Anderson's theorem if s-wave SC gap structure is anisotropic. Thus it is important to directly investigate the anisotropy of order parameter.

The presence of nodes being established from several experimental probes, it is pivotal to pin down the exact topology of the FSs and the location of nodes in the momentum space. In the cuprate superconductors, the location of node is dictated by the universal B_{1g} ($d_{x^2-y^2}$-wave) symmetry of order parameter to be on the diagonal lines in the k_x-k_y plane. In the FeSCs, however, the appearance of nodes is accidental in the sense that the zero of the order parameter is not protected by its symmetry but by the quantitative details of the pairing interactions. Therefore it is anticipated that the nodal structure is material specific and systematic studies on the chemical elements and compositions are required.

The first experimental proposal on the nodal gap structure for Ba122P appeared

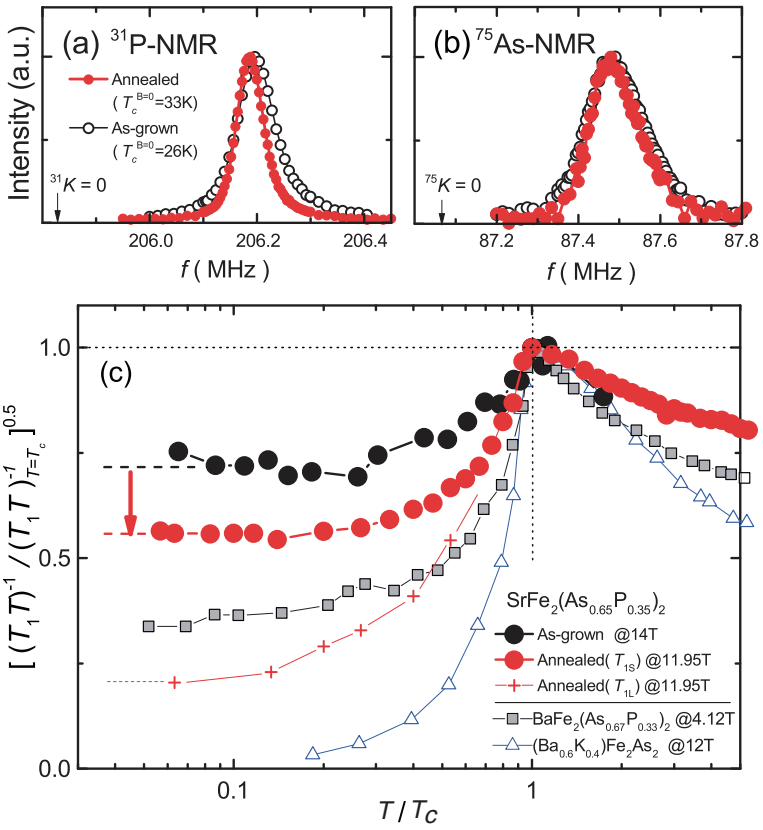

Figure 1.17: (a) ^{31}P-NMR and (b) ^{75}As-NMR spectra of as-grown and annealed $SrFe_2(As_{0.65}P_{0.35})_2$ at $T = 70$ K under 11.95 T. (c) Reproduced from Ref. [33].

from an angle-resolved thermal conductivity (κ) measurement. Yamashita *et. al.* [34] measured the thermal conductivity under rotating magnetic field within the basal plane. The Doppler shift of the quasiparticle energy by the amount $\delta\epsilon(\boldsymbol{r}, \boldsymbol{v}_F) = \boldsymbol{v}_F(\boldsymbol{k}) \cdot \boldsymbol{p}_s(\boldsymbol{r})$, where $\boldsymbol{p}_s(\boldsymbol{r})$ is the superflow due to vortices normal to H, causes change in the density of states at E_F, thereby modifying the quasiparticle entropy flow. Under the experimental geometry shown in Fig. 1.18, κ exhibits fourfold oscillatory behaviour as a function of magnetic field angle ϕ. With theoretical considerations to reproduce the experimental result under the A_{1g} symmetry, Yamashita *et. al.* concluded that the line nodes appear on the flat part of the electron FS and form three-dimensional loops [Fig. 1.18 (b)].

The direct information on the three-dimensional gap structure can, in principle, be obtained from ARPES experiments using tunable incident photon energy $h\nu$. However, mutually inconsistent results for Ba122P have been reported in the literature. Fig. 1.19 (a) shows the SC gaps on the hole sheets determined by laser ARPES with $h\nu = 7$ eV [35]. Shimojima *et al.* [35] claims that $h\nu = 7$ eV corresponds to $k_z = \pi$ plane and that the three hole sheets have almost identical gap of 3 meV. A following work by photon-energy dependent ARPES [36] shown in panel

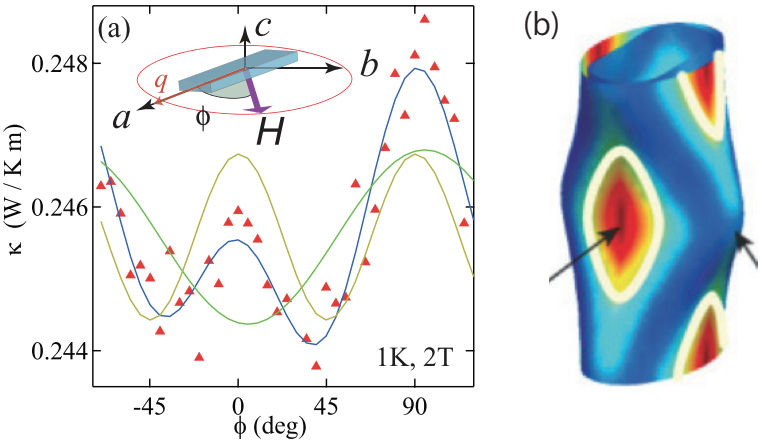

Figure 1.18: (a) ^{31}P-NMR and (b) ^{75}As-NMR spectra of as-grown and annealed $SrFe_2(As_{0.65}P_{0.35})_2$ at $T = 70$ K under 11.95 T. (c) Reproduced from Ref. [34].

(b) reported that the nodes appear horizontally on the outer hole sheet around the Z point. Another work from synchrotron ARPES [37] claimed that observed fully-gapped superconducting gap on the hole sheets. To clarify the reason of the discrepancy, we have studied the phosphorous content dependence and the gap structure of Sr122P by synchrotron ARPES. Chapter 5 is devoted to the result of annealed and optimally-doped Sr122P.

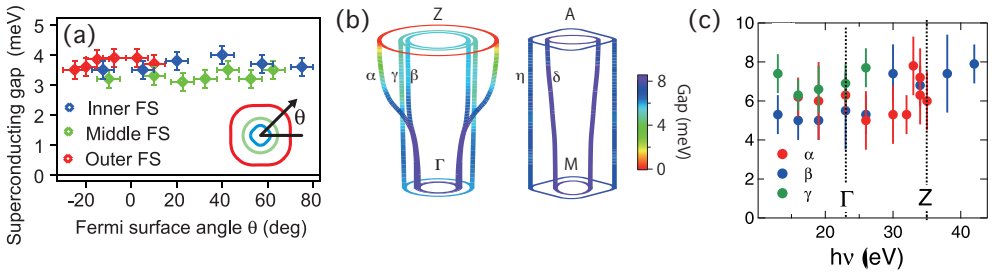

Figure 1.19: (a) SC gaps of Ba122P on the hole sheets determined from laser ARPES [35]. (b) Three-dimensional SC gaps of Ba122P determined from photon-energy-dependent ARPES [36]. Nodes appear horizontally on the outer hole sheet around the Z point. (c) Another report from synchrotron ARPES [37], that observed fully-gapped superconducting gap on the hole sheets.

A theoretical calculation of the superconducting gap structure of 10-orbital model of Ba122P based on spin-fluctuation exchange is performed in Ref. [38]. Within the spin-fluctuation mediated mechanism, the gap is basically s-wave, with a sign change between the hole and electron FSs. Suzuki *et al.* predicts that three-dimensional node structure on one of the hole sheets. Figure 1.20 (a) shows the gap function of the $z^2/xz/yz$ hole FS (outer FS around the Z point) on which the sign change occurs. The sign is mainly minus, but a sign change occurs around $k_z = \pi$ plane. Fig-

ure 1.20 shows the gap function from orbital-fluctuation exchange mechanism [39]. As a result of competition between repulsive interaction from spin fluctuation exchange and attractive interaction from orbital fluctuation exchange, the loop-like line nodes are located at electron FSs.

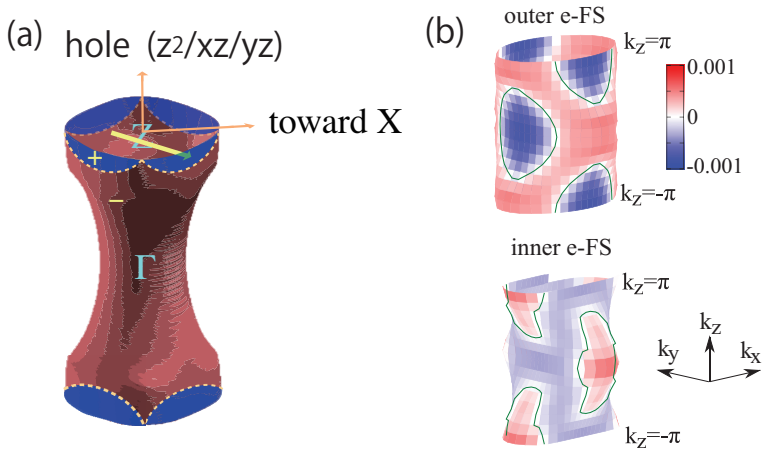

Figure 1.20: (a) Gap function of the $z^2/xz/yz$ hole FS in 10-orbital model of BaFe2($As_{0.36}P_{0.34}$)$_2$ within spin-fluctuation exchange from Ref. [38]. Sign change occurs around the Z point ($k_z = \pi$). (b) Gap function of the electron FSs in 10-orbital model within orbital-fluctuation exchange calculations from Ref. [39].

1.2 Ultrafast phenomena in iron-based superconductors

The ultrafast dynamics in condensed matter physics has been the central focus of intense research along with the advent of pump-probe type experimental techniques. Here, fundamental laser pulses are split into pump and probe portions; the pump beam is used to optically excite the electronic system and the several physical quantities are measured by the probe beam. Soon after the discovery of FeSCs, the relaxation dynamics from optically excited states in FeSCs has been investigated by several experimental techniques. Here I summarize some previous works on $BaFe_2As_2$ systems.

1.2.1 Low-energy elementary excitations

The direct information about the elementary excitations can be obtained from inelastic scattering experiments. Since the relaxation dynamics is strongly governed by the coupling between the excited electrons and low-energy elementary excitations, it is essential to clarify the their energy scales and momentum dependence.

The energy dispersions of the elementary excitations determine the available phase space in which excited electrons decay satisfying the energy and momentum conservations.

Figure 1.21 shows Raman response spectra from $BaFe_2As_2$. The coordinates are defined in the inset of panel (a). When the incident photon polarization is parallel to the z' axis and the outgoing photon polarization to the x' axis, one observes the E_g modes at 124 and 264 cm^{-1} involving Fe and As displacements, and the B_{1g} mode at 209 cm^{-1} involving Fe displacement along the c axis. Raman spectra for different temperatures are shown in Fig. 1.21 (b). The lower energy E_g mode splits between 135 K and 145 K, reflecting the lattice parameter change at the structural transition. The inset shows the Raman spectra in the $(z'z')$ configurations. The A_{1g} phonon peak involving symmetric As oscillations shows up below 147 K. Oscillatory phenomena observed in various pump-probe experiments we shall see below are mostly assigned to the A_{1g} mode.

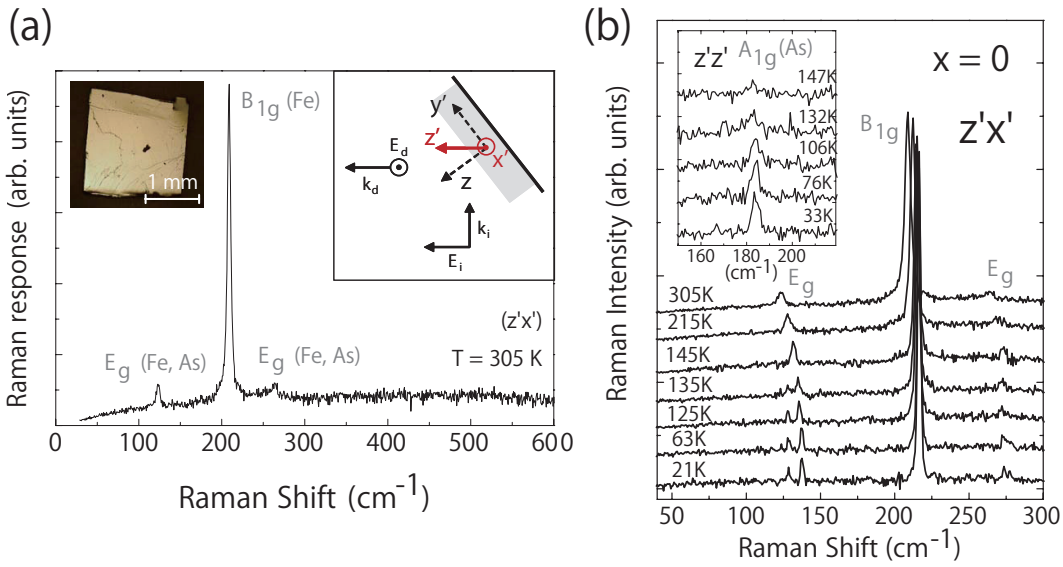

Figure 1.21: Raman scattering spectra of $BaFe_2As_2$ [40]. (a) Raman spectrum for $T = 305$ K collected with $(z'x')$ configuration. The definition of the polarization axes is shown in the inset. The E_g and B_{2g} modes are allowed in this geometry. (b) Raman spectra with $(z'x')$ configuration for different temperatures. Inset: Raman spectra with $(z'z')$ configurations. A_{1g} peaks appear below 147 K.

The phonon spectrum has also been investigated through inelastic neutron scattering. Zbiri *et. al.* [41] measured phonon density of states by neutron scattering and compared the result with the density functional phonon calculations. Top panels in Fig. 1.22 show calculated vibrational dispersion relations and DOS for tetragonal (S1) and orthorhombic (S2) structures. Acoustic branches extend up to 9 meV and the lowest optical mode appears from 12 meV. The bottom panels compare the

calculated and experimental phonon DOS. In both structures, agreement between them is qualitatively good. The experimental data for 140 K is slightly above the Néel temperature, but some modes noticeably harden upon cooling as compared with that of 300 K.

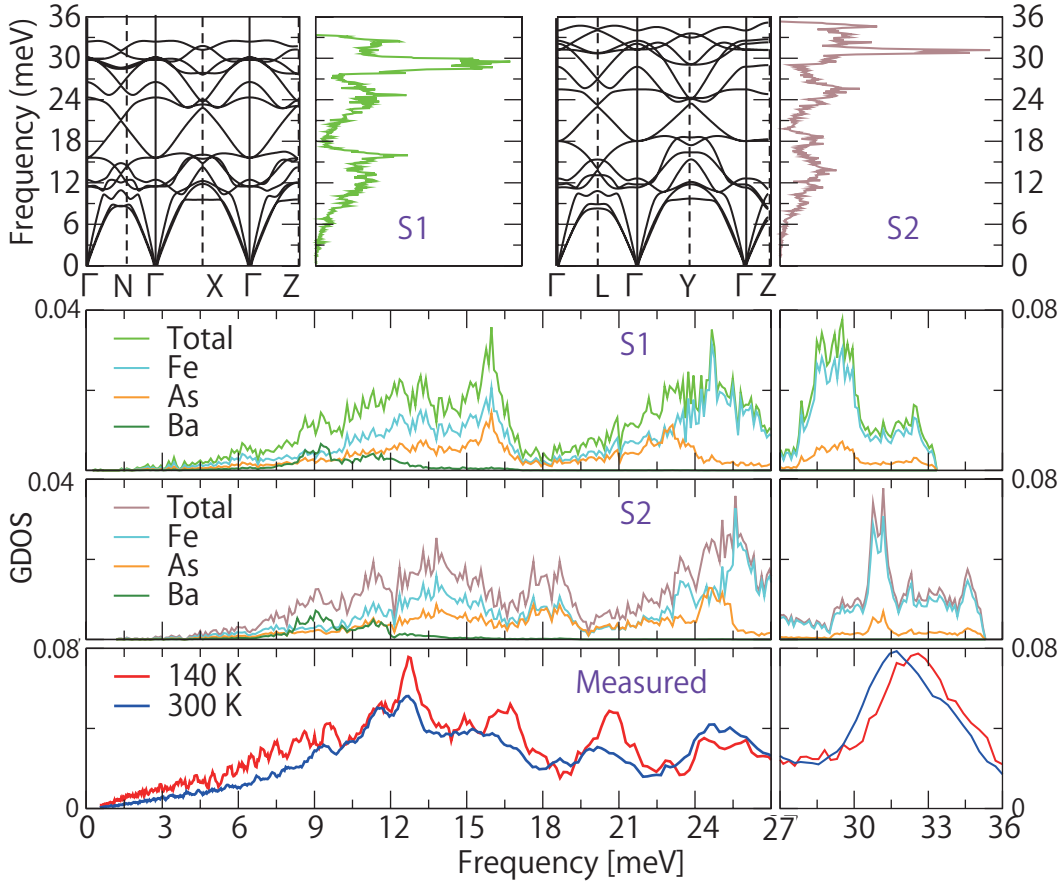

Figure 1.22: Calculated and inelastic neutron scattering phonon spectra of $BaFe_2As_2$ from Ref. [41]. Top panels: dispersion relations and vibrational DOS for tetragonal (S1) and orthorhombic (S2) phases. Bottom panels: calculated partial vibrational DOS and experimental phonon DOS for two temperatures.

1.2.2 Time-resolved optical reflectivity

Early studies of the ultrafast dynamics in FeSCs came from time-resolved optical reflectivity. Torchinsky *et. al.* [42] reported the ultrafast dynamics of superconducting $Ba_{0.6}K_{0.4}Fe_2As_2$ ($T_c = 37$ K). Figure 1 (a) and (b) show transient normalized reflectivity at 7 K and 60 K, respectively, for different pump fluences. In the superconducting state, photoexcitation reduces the reflectivity and the relaxation dynamics depends strongly on the fluence. The decay rate systematically decreases from

16 μJ/cm^{-1} to 7 μJ/cm^{-1}. This observation is interpreted as the competition between the Cooper pair formation from quasiparticles and pair quasiparticle creation from bosonic degrees of freedom. The former factor is linearly dependent on the quasiparticle population and causes the rapid decay in the strong fluence regime. The normal state data taken at 60 K is shown in Fig. 1.23 (b). The data with different fluences fall on the same curve, signifying that the relaxation dynamics is related to superconductivity.

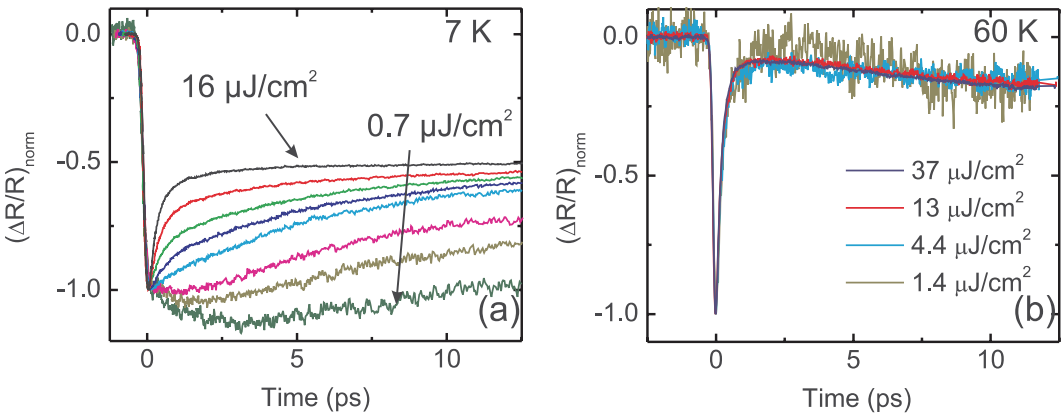

Figure 1.23: Time-resolved reflectivity curves of $Ba_{0.6}K_{0.4}Fe_2As_2$ taken from Ref. [42]. (a) Superconducing phase ($T = 7$ K) for different fluences. (b) Normal state ($T = 60$ K). The temporal evolution is independent of pump fluence.

Mansart *et. al.* [43] studied the superconducting $Ba(Fe_{0.92}Co_{0.08})_2As_2$. Figure 1.24 (a) shows normalized reflectivity spectra for different fluences. Note that the pump fluence regime (mJ/cm^{-2}) is by order of three stronger than Ref. [42]. All the spectra show sudden increase of reflectivity at $t = 0$ followed by a decay with two different time scales. The initial fast decay process occurs within $\sim$ 1 ps after the pulse, and the slow decay continues for $\sim$ 6 ps. On top of the decay, one observes oscillation components that are attributed to coherent A_{1g} phonon excitations, and the oscillation amplitude increases with the fluence. Together with the the low-fluence data by Torchinsky *et. al.*, this result indicates that in the strong fluence regime (mJ/cm^2) the relaxation is primarily governed by the electron-phonon coupling while in weak fluence regime (μJ/cm^2) by Cooper-pair recombination. Reflectivity curves with 1.3 mJ/cm^2 for 10 K and 25 K are compared in Fig. 1.24 (b). The fact that the relaxation process is unchanged across the superconducting transition at $T_c = 24$ K proves that in the strong fluence regime the fast relaxation is not related to a electronic recombination across the superconducting gap but determined by the electronic temperature.

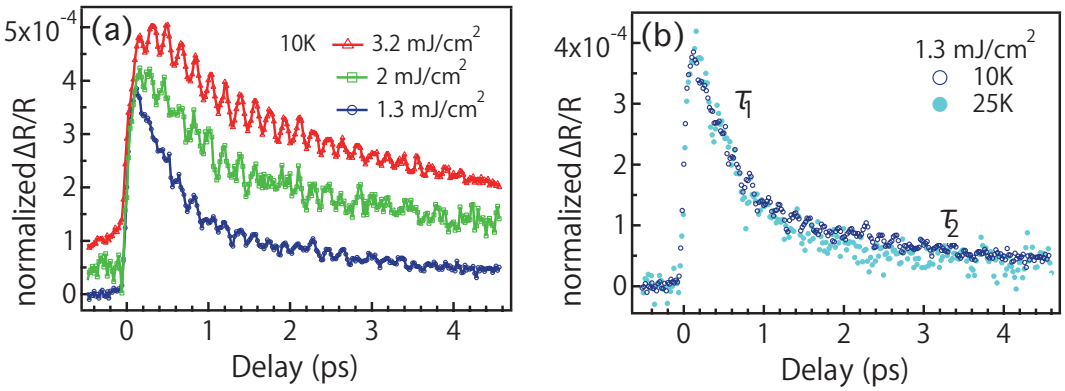

Figure 1.24: Time-resolved reflectivity curves of $Ba(Fe_{0.92}Co_{0.08})_2As_2$ [43]. (a) Superconducing phase ($T = 10$ K) for different fluences. (b) With 1.3 mJ/cm^2 fluence for 10 K and 25 K.

1.2.3 Time-resolved photoemission spectroscopy

The nonequilibirium spectral function can be directly studied by time- and angle-resolved photoemission spectroscopy (TrARPES). Rettig *et al.* [44] reported the electronic dynamics of $EuFe_2As_2$ around the Γ point with $h\nu_{\text{pump}} = 1.5$ eV and $h\nu_{\text{probe}} = 6$ eV. Figures 1.25 (a) shows the ARPES spectra at $t = 100$ fs. Reflecting the holelike band dispersions around the Γ point in the high-temperature paramagnetic states, the intensity inside k_F increases above E_F [panel (c)] and that out of k_F [panel (b)] decreases below E_F. Figures 1.25 (d) and (e) show the temporal evolution of the EDCs at the Γ point above and below T_N and the red points indicate the leading edge midpoints (LEMs). Above T_N [panel (d)], the LEMs below the pump is at E_F, and start to oscillate after the pump. Below T_N [panel (e)], the LEMs below pump is at ~ 0.15 eV, reflecting the opening of the SDW gap. At $t = 0$, the spectral intensity appears above E_F and the LEMs come close to E_F. The authors interpret this as the melting of the SDW and the recovery time is estimated to be 800 fs.

To elaborate the oscillatory phenomena, in the following work Avigo *et al.* [45] performed similar measurements on superconducting $BaFe_{1.85}Co_{0.15}As_2$ with various pump fluences. Figure 1.26 shows the TrARPES intensity at the Γ point as a function of delay time. Oscillatory intensity profile is also observed as in $EuFe_2As_2$. The integrated intensity shown in panel (b) indicate that the the population of hot electrons and the amplitude of oscillation increase with the pump fluence, but that the frequency remains almost unchanged, as fast Fourier transform spectra in panel (c) manifest. There are three peaks in the frequency: 5.6, 3.3, and 2.6 THz. The 5.6 THz peak is assigned to the Raman-active A_{1g} mode observed above.

The investigation into the dynamics in the zone corner requires higher energy probe beams. Yang *et al.* [46] investigated into the dynamics both at the Γ and X

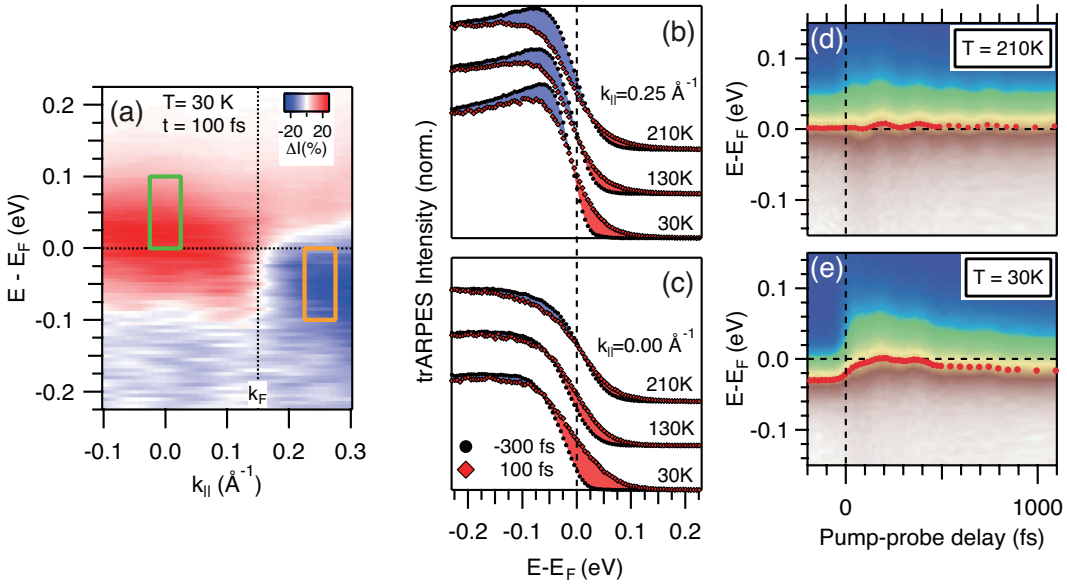

Figure 1.25: (a) Time-resolved ARPES (TrARPES) spectra at $t = 300$ fs. (b), (c) Energy distribution curves for $k_{||} = 0.25$ Å^{-1}[(b)] and $k_{||} = 0$ Å^{-1} [(c)]. (d), (e) TrARPES intensity at Γ for $T = 210$ K [(d)] and $T = 30$ K [(e)]. Reproduced from Ref. [44].

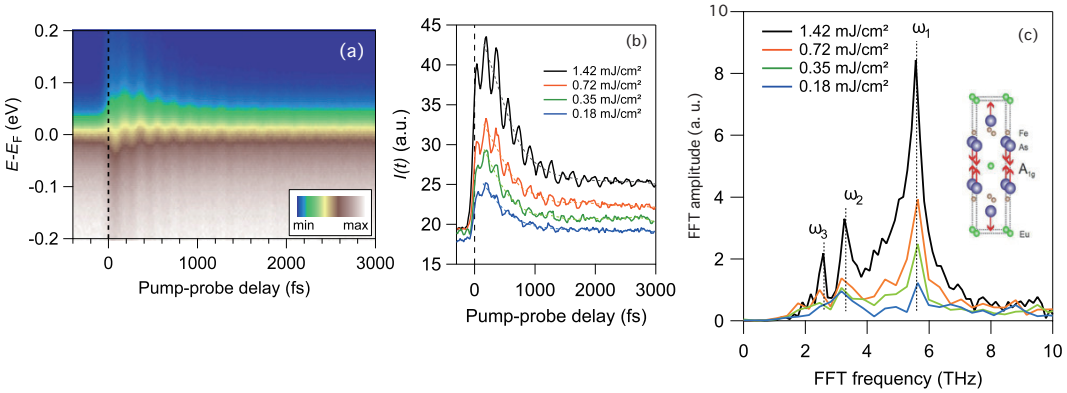

Figure 1.26: (a) TrARPES spectra of $BaFe_{1.85}Co_{0.15}As_2$ at $T = 100$ K. (b) Integrated TrARPES intensity for different pump fluences. (c) Fourier transform of spectra in panel (b). Reproduced from Ref. [45].

points by ultraviolet higher harmonic generation (HHG). The temporal evolution of EDCs at the Γ and X points are shown in Figs. 1.27 (a) and (b), respectively. Both at Γ and X points, intensities above E_F increase at $t = 0$, and start to oscillate. To quantify this observation, the authors fitted the EDCs by Fermi-Dirac distribution functions and estimated the electronic temperature and the chemical potential (Figs. 1.27 (c) and (d)). The temperature jumps up at $t = 0$ and shows a simple exponential decay with decay constant 380 fs, whereas the chemical potential starts to oscillate at $t = 0$ and the amplitude slowly decays with 660 fs. These parameters are identical both at Γ and X points, and the oscillation frequency 5.4 THz matches that of A_{1g} phonon mode.

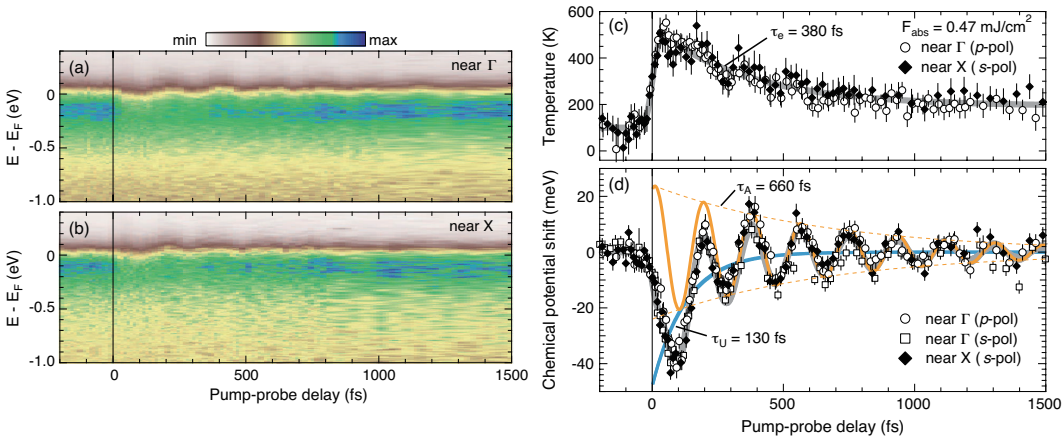

Figure 1.27: (a), (b) TrARPES spectra of $BaFe_2As_2$ taken with $h\nu = 22.1$ eV. (c), (d) The electronic temperature and chemical potential parameters as a function of delay time. Reproduced from Ref. [46].

1.2.4 Time-resolved x-ray diffraction

Time-resolved x-ray diffraction combines the pump photons from laser with pulsed x-rays generated from synchrotron electron bunch or free electron laser. In order to directly probe the structural modifications caused by optical excitations, Rettig *et. al.* [47] performed time-resolved x-ray diffraction measurement on $BaFe_2As_2$ utilizing pulsed hard x-ray generated by slicing technique. Figure 1.28 (a) shows the atomic motion of the A_{1g} phonon oscillation. When the As atoms coherently oscillate along the c axis, Fe-As tetrahedra angle α is modified and causes change in the intensity profile of Bragg spots. All the previous assignment of oscillatory phenomena to the A_{1g} mode were based solely on theoretical considerations on their energy scale or frequency. Figure 1.28 (b) illustrates the experimental setup. The transient states generated by 1.5 eV pulses from solid state laser are probed by 7 keV x-ray pulse synchronized with the probe pulse. Rocking curves of the $(1, 0, 5)$

and $(2, 0, 6)$ Bragg reflection spots before and after the optical pump are shown in panel (c). While the intensity at $(1, 0, 5)$ increases after the pump, that at $(2, 0, 6)$ decreases. Intensity modifications for various pump fluences are shown in panels (d) and (e). Rapid increase/decrease in the intensity followed by picosecond-time-scale decay are observed, on which oscillatory component originating from the A_{1g} phonon oscillation is superimposed. One also notices that the intensity change and the amplitude of the oscillation is linearly dependent on the pump fluence. The diffraction signal are fitted as a summation of an displacive and an oscillatory component:

$$\Delta I/I_0 = A_{\text{disp}} e^{-t/t_{\text{disp}}} + A_{\text{disp}} \cos(\omega t + \Phi) e^{-t/t_{\text{disp}}}. \tag{1.8}$$

This behavior indicates that the pump pulse instantaneously creates a new potential minimum and a coherent oscillation around the new minimum [48]. A following study utilizing x-ray free electron laser [49] has come to a similar conclusion, and it also reported that there is no structural transition from orthorhombic to tetragonal symmetry within 4.5 ps.

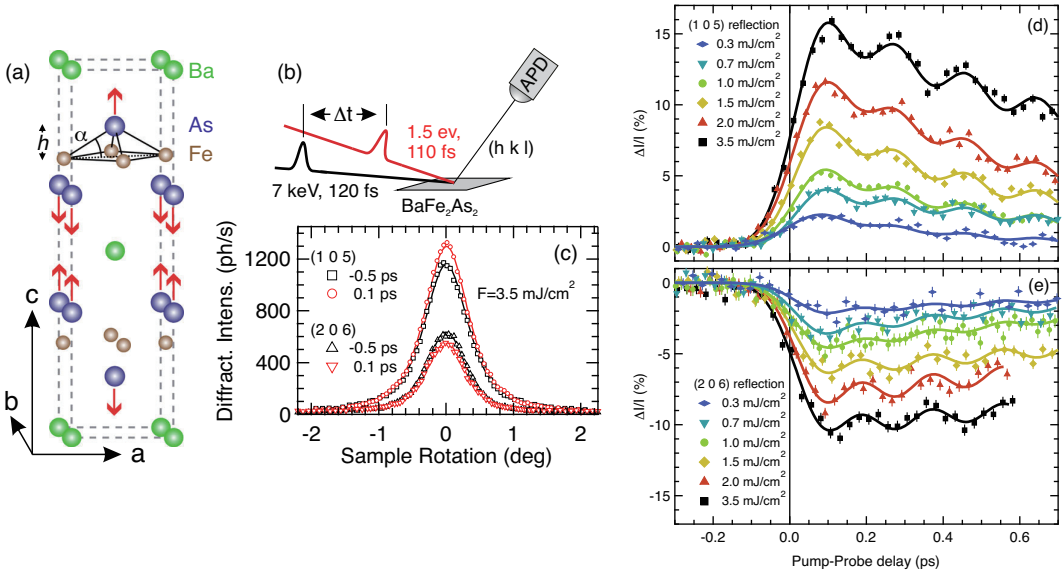

Figure 1.28: Time-resolved x-ray diffraction experiment on $BaFe_2As_2$ from Ref. [47]. (a) Illustration of atomic motion of A_{1g} phonon mode. (b) Experimental geometry. (c) Rocking curves of the $(1, 0, 5)$ and $(2, 0, 6)$ Bragg reflections 0.5 ps before and 0.1 ps after the optical excitations. (d), (e) Photo-induced intensity change of the $(1, 0, 5)$ and $(2, 0, 6)$ peaks for various pump fluences.

1.2.5 Three-temperature model

Although experimental investigations into ultrafast phenomena have developed rapidly, theoretical framework that describes them is not yet fully developed partly because

of the absence of nonequilibrium statistical mechanics. From the rates of change of electron and phonon distributions, Allen [50] derived the temperature relaxation $dT_e/dt = \gamma(T_L - T_e)$, where T_e and T_L are electron and lattice temperatures, respectively. Important consequence is a formula $\gamma = 3\hbar\lambda\langle\omega^2\rangle/\pi k_B T_e$, where $\lambda\langle\omega^2\rangle$ is an important parameter in the theory of superconductivity. In order to apply the formalism to the multi-timescale decay behavior of time-resolved ARPES data, Ref. [51] introduced a phenomenological three-temperature model, which describes the temporal temperature evolution of the electronic and lattice systems after the excitation process. Three temperature model divides the system into hot electrons, phonons which couple to the electrons, and phonons which do not interact with electrons. A set of rate equations describing the energy transfer from the optical pulse into the electronic system and active/inactive phonons, and their temperature evolutions is given by

$$\frac{\partial T_e}{\partial t} = -\frac{3\lambda\Omega_0^3}{\hbar\pi k_B}\frac{n_e - n_p}{T_e} + \frac{P}{C_e} \tag{1.9}$$

$$\frac{\partial T_p}{\partial t} = \frac{C_e}{C_p}\frac{3\lambda\Omega_0^3}{\hbar\pi k_B}\frac{n_e - n_p}{T_e} - \frac{T_p - T_l}{\tau_\beta} \tag{1.10}$$

$$\frac{\partial T_l}{\partial t} = \frac{C_p}{C_l}\frac{T_p - T_l}{\tau_\beta} \tag{1.11}$$

,where P represents the energy supplied from the pump pulse. Here, the phonon spectrum is approximated by an Einstein model with frequency Ω_0. The specific heat of the electron, hot phonons and the remaining phonons are $C_e = \gamma_e T_e, C_p = 3f\Omega_0\frac{\partial n_p}{\partial T_p}$, and $C_l = 3(1-f)\Omega_0\frac{\partial n_p}{\partial T_p}$. The fraction f represents the proportion of the hot phonons.

1.3 New ferromagnetic semiconductors isostructural to iron-based superconductors

1.3.1 Spintronics

Electronic products are made up of numerous electronic devices. Conventional devices are divided into two categories: devices that utilize its electric properties like transistors, or the ones that are based on the magnetic properties such as hard disk drives. Recently, *Spintronics*, a concept in which both the electric and magnetic degrees of freedom are fully employed for the achievement of novel functionalities, has been proposed and intense research has been performed worldwide both in academia and industry [52]. Spintronics is expected to allow spin polarized carrier transport, low power consumption and a new form of information processing. Spintronic devices based on paramagnetic and ferromagnetic metals or insulators

include well-established applications, for example, magnetic read heads in hard disk drives, nonvolatile random access memory, and magnetic-field sensors.

1.3.2 Diluted magnetic semiconductors

Considering the compatibility with existing semiconductor technologies, the realization of semiconductor-based spintronic devices will enlarge the potential of spintronics. As a possible candidate, diluted magnetic semiconductors (DMSs), in which a fraction of host semiconductor is replaced by magnetic elements, have attracted much attention [53–56]. In particular, the achievement of ferromagnetic DMS is highly desired for novel storage devices. While semiconductor devices utilize electrons of s and p character, magnetism usually occurs from transition metal d electrons. If the interaction between s, p electrons and d electrons can be manipulated in a single material, it opens future possibility of information storage to the spins of localized d electrons and its processing by the itinerant s, p electrons. From application points of view, ferromagnetic DMS with room-temperature Curie temperature (T_C) is strongly desired.

Prototypical DMSs are summarized in Table 1.2 with their optimal ferromagnetic T_C's. Since absolute T_C values and their definitions vary in the literature, I also indicate the references.

II-VI DMSs include tellurides, selenides and sulfides doped with Mn or Cr. The valence match between the divalent II elements and the magnetic elements makes it easy to dope magnetic elements. III-V DMSs include prototypical materials $Ga_{1-x}Mn_xAs$ and $Ga_{1-x}Mn_xN$. GaAs is an widely recognized semiconductor for device applications and GaN is used in light emitting diodes. V family DMSs include $Ge_{1-x}Fe_x$ and $Ge_{1-x}Mn_x$, which have been studied due to good compatibility with Si-based semiconductor devices.

Oxide semiconductors can also be made ferromagnetic and are often termed as diluted magnetic oxides (DMOs) [57]. They are characterized by the T_C's far in excess of room temperature and large ordered moments per transition-metal cation. The search for DMO are largely prompted by a theoretical suggestion by Dietl *et al.* [54], which predicted from mean-field Zener model that p-type GaN and ZnO are promising candidates for high-T_C ferromagnetism. As an alternative scenario, Coey *et. al.* [57] proposed the spin-split impurity band formed by oxygen vacancies is playing an essential role in mediating ferromagnetism. While room-temperature ferromagnetism is claimed in several materials, it is still open to discussion whether observed ferromagnetism is truly from the DMSs or from phase-segregated magnetic precipitates.

Among them, the most heavily studied DMS is the Mn-doped GaAs, $Ga_{1-x}Mn_xAs$ (GaMnAs) [53, 75]. GaAs is a direct bandgap semiconductor in a zinc blende crys-

Table 1.2: Representative diluted magnetic semiconductors and their respective T_C's.

Material Class	Material	T_C (K)	Reference
II-VI	$Cd_{1-x}Mn_xTe$	1.8	[58]
II-VI	$Zn_{1-x}Mn_xTe$	1.5	[59]
II-VI	$Zn_{1-x}Cr_xTe$	300	[60]
IV-VI	$Pb_{1-x-y}Sn_yMn_xTe$	4	[61]
III-V	$In_{1-x}Mn_xAs$	55	[62]
III-V	$Ga_{1-x}Mn_xAs$	185	[63]
III-V	$Ga_{1-x}Mn_xN$	>740	[64]
III-V	$Ga_{1-x}Cr_xN$	280	[65]
III-V	$Ga_{1-x}Mn_xP$:C	270	[66]
III-V	$Ga_{1-x}Mn_xSb$	400	[67]
IV	$Ge_{1-x}Mn_x$	116	[68]
IV	$Ge_{1-x}Fe_x$	170	[69]
Oxide	$Ti_{1-x}Co_xO_2$	>400	[70]
Oxide	$Zn_{1-x}Mn_xO$	>420	[71]
Oxide	$Sn_{1-x}Co_xO_2$	650	[72]
Oxide	$Sn_{1-x}Fe_xO_2$	610	[73]
Oxide	$In_{2-x}Cr_xO_3$	930	[74]

tal structure with the direct band gap of 1.424 eV at the Γ point. Magnetic element Mn is doped into the Ga sites simultaneously doping hole carriers. Figure 1.29 (a) shows the sheet resistance R_{sheet} of GaMnAs ($x = 0.015$-0.171). For the low-Mn regime, R_{sheet} diverges as $T \to 0$, reflecting the semiconducting transport of GaAs host. For $0.03 < x < 0.06$, R_{sheet} take maxima and go down as $T \to 0$. The fact that these maxima approximately equal to T_C indicates that the carrier scattering is influenced by the ferromagnetic ordering. The negative magnetoresistance in GaMnAs is shown in Fig. 1.29 (b). By applying the external magnetic field, the resistivity drops. This reflects the reduced carrier scattering by local spins when they are ferromagnetically ordered.

Due to its simple constitution, GaMnAs has several drawbacks as well. First, the substitutional divalent Mn atoms at the trivalent Ga sites show severely limited chemical solubility and only thin films grown by low-temperature MBE are available. Second, since the Mn doping simultaneously plays the role of introducing hole carriers and magnetic elements, these two parameters cannot be controlled independently. Further, the Mn doping often entails uncontrollable antisite As defects, which compensate holes introduced by Mn. This makes difficult to control the total carrier density of the system. In the carrier-induced ferromagnetism occurring in DMS systems, it leads to uncontrollability of T_C. For device applications it is

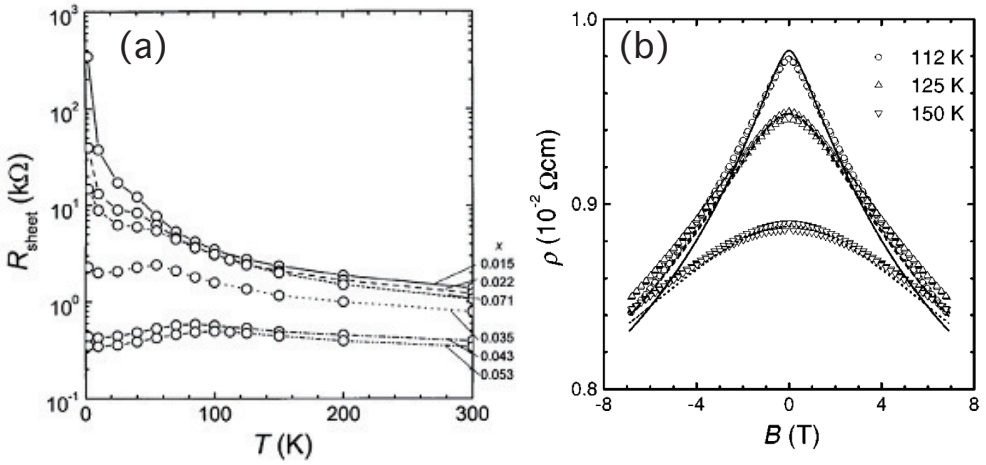

Figure 1.29: (a) Sheet resistance of $Ga_{1-x}Mn_xAs$ for ($x = 0.015 - 0.171$). (b) Negative magnetoresistance at three different temperatures above T_C for $x = 0.053$. Figures reproduced from Ref. [76].

mandatory to overcome these difficulties.

1.3.3 Theoretical models of carrier-induced ferromagnetism

Zener [77, 78] first proposed the model of carrier-induced ferromagnetism in transition metals driven by the exchange interaction between carriers and localized spins. This model has been abandoned as a theory of magnetic metals, since neither the itinerant character of magnetic electrons nor the quantum oscillations of the electron spin polarizations are not fully taken into account. However, in the case of semiconductors, the Friedel oscillations averages to zero because the average distance between the carriers is greater than that between the spins. In such a case, Dietl *et al.* [79] showed that the Zener model becomes equivalent to the Ruderman-Kittel-Kasuya-Yoshida (RKKY) interactions, where the presence of oscillations is fully taken into account.

A drawback of the mean-field Zener model is that charge carriers are treated as free carriers. It does not explain the experimentally observed transport properties such as insulating and ferromagnetic GaMnAs with low Mn concentrations. As an opposite approach, the bound magnetic polaron (BMP) model was proposed by Kaminski *et al.* [80]. In this limit, localized holes in DMSs exhibit exchange interaction with a number of magnetic polaron, as illustrated in Fig. 1.30 (a). The ratio of the exchange interaction and thermal energy governs the effective radii of BMPs. At sufficiently low temperature, spontaneous magnetization arises as a result of a ferromagnetic percolation of BMPs.

The donor impurity band model was proposed by Coey *et al.* [57] after the

reports of possible room-temperature ferromagnetism in oxide-based DMSs. The mean field Zener model predicts that p-type DMSs possess high T_C. However, the most of the oxide DMSs are n-type due to the oxygen vacancies. To overcome this inconsistency, Coey *et al.* [57] introduced the donor impurity band model, which is an extension of the BMP model by taking into account the properties of defects. Shallow donors associated with the defects form BMPs, by which the ferromagnetic ordering of local moment is mediated. When the BMPs overlap at sufficiently high concentrations, a spin-split impurity band is formed in the band gap and ferromagnetic ordering is achieved in entire material. Figure 1.30 (b) shows schematic band structure of an oxide with $3d$ impurities with a spin-split doner impurity band [57]. In this model, the spin polarization of the impurity band is the key parameter for the emergence of ferromagnetism. The left panel shows the case when the splitting of the impurity band is small. In this case the exchange interaction between the local moment and the carriers is not efficient, leading to low T_C. High T_C is achieved if the splitting becomes large as shown in the center panel. The character of the $\uparrow$ states can also be of the impurity band instead of the $3d$ levels (right panel).

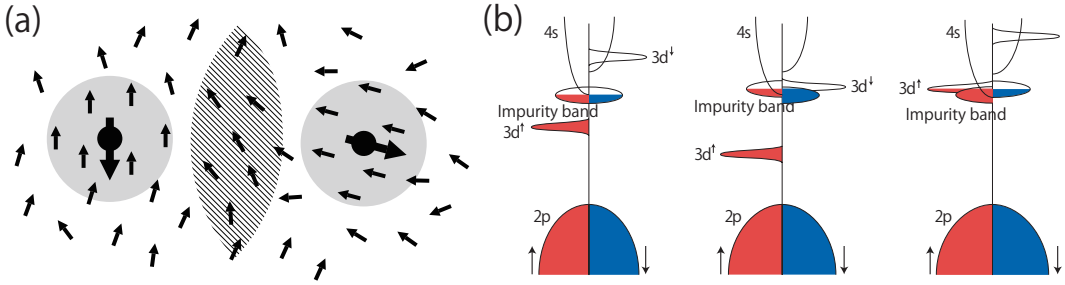

Figure 1.30: (a) Interaction of two bound magnetic polarons reproduced from Ref. [76]. Polarons are shown with gray circles. Small and large arrows show impurity and hole spins. (b) Energy diagrams of oxide DMSs with $3d$ impurities from Ref. [57]. Left: The position of the $3d$ level for low T_C, when the splitting of the impurity band is small. Center: High T_C configuration where minority $3d$ states interact with the spin-split impurity band. Right: High T_C configuration where the majority spin states interact with the impurity band.

1.3.4 Novel ZnAs-based ferromagnetic semiconductors

The history of new ZnAs-based ferromagnetic DMSs originates from the theoretical prediction of n-type ferromagnetism in $LiZn_{1-x}Mn_xAs$ by Mašek *et al.* [81]. The calculated crystal structure of $LiZn_{1-x}Mn_xAs$ is shown in Fig. 1.31. Compared with the crystal structure of GaMnAs, the Zn atoms take Ga sites and Li atoms take tetrahedral interstitial sites with respect to As atoms. Based on coherent potential approximations, Ref. [81] predicted that, while the Mn ions are isovalent to Zn ions, Mn doping induces further substitutional Li_{Zn} atoms at the Zn sites and interstitial

Li_I at tetrahedral interstitial sites of Zn. It is expected from energetics considerations that the amount of doner Li_I is always larger than that of acceptor Li_{Zn} so that the system as a whole becomes n-type. The spin-resolved DOS for GaMnAs and $LiZn_{1-x}Mn_xAs$ are shown in the bottom panels. Like in GaMnAs, $LiZn_{1-x}Mn_xAs$ shows spin polarizations with main DOS of $\uparrow$ band at -5 eV.

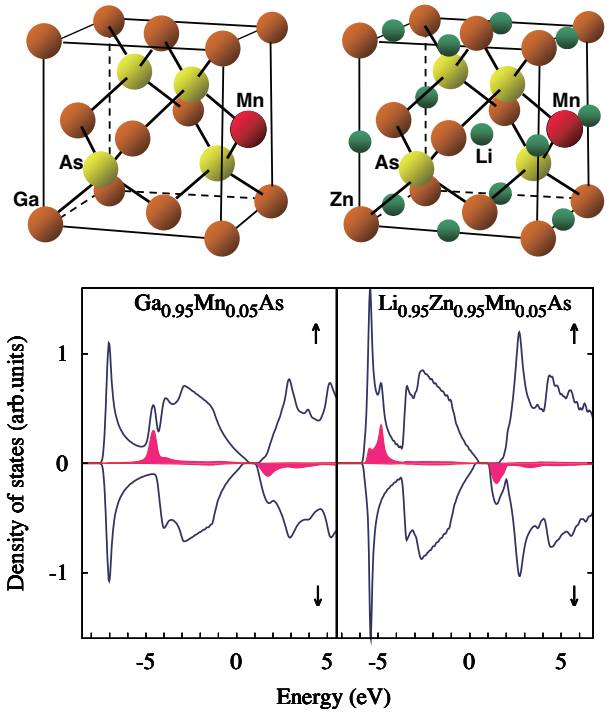

Figure 1.31: Top panels: Calculated crystal structure of $Ga_{1-x}Mn_xAs$ and $LiZn_{1-x}Mn_xAs$ crystal structures. Bottom panels: Total DOS and Mn d-oribital projected DOS. Reproduced from Ref. [81].

After the theoretical prediction, Deng *et. al.* [82] successfully synthesized ferromagnetic $LiZn_{1-x}Mn_xAs$ as the first example of ZnAs-based DMS. Figure 1.32 shows the crystal structure of $LiZn_{1-x}Mn_xAs$. It has the predicted crystal structure with lattice parameter 5.94 Å. Figures 1.32 (b) and (c) show the magnetization properties. The nominal optimal composition that gives the highest T_C is $Li_{1.1}Zn_{0.85}Mn_{0.15}As$ with the saturated magnetization of 1.1 μ_B/Mn. The excess Li atoms are anticipated to take the interstitial sites and to act as donors, but the Hall effect measurement indicates that the carriers are indeed p-type, contrary to the theoretical prediction. This discrepancy can be explained when the excess Li atoms in reality take mainly substitutional Zn sites, and act as acceptors. In the following work, Deng *et. al.* reported that the isovalent material $LiZn_{1-x}Mn_xP$ [83] also shows p-type ferromagnetism. Although $LiZn_{1-x}Mn_xAs$ and $LiZn_{1-x}Mn_xP$ proved not to be longed-for n-type DMSs, they sparked off an intensive search for new ZnAs DMSs.

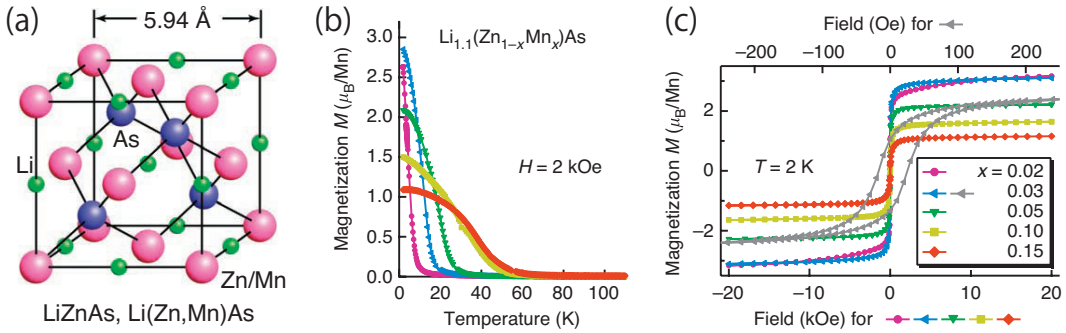

Figure 1.32: (a) Crystal structure of $LiZn_{1-x}Mn_xAs$. (b) Magnetization curves as a function of temperature at $H = 2$ kOe. (c) Magnetization as a function of external magnetic field at $T = 2$ K. Figures reproduced from Ref. [82].

As a second example of ZnAs-DMS, Zhao *et. al.* [84] successfully synthesized $Ba_{1-x}K_x(Zn_{1-y}Mn_y)_2As_2$ (Mn-$BaZn_2As_2$), which is the main focus of this thesis. The crystal structure of Mn-$BaZn_2As_2$ is shown in Fig. 1.33 (a). Mn-$BaZn_2As_2$ has the tetragonal $ThCr_2Si_2$ structure and is isostructural to the "122"-type iron-based superconductor $BaFe_2As_2$. Here, the hole carriers are introduced by K doping to the Ba sites, and the magnetic elements are introduced by the Mn doping to the Fe sites. Mn atoms are tetrahedrally coordinated by As ligands, which is equivalent to Mn atoms in GaMnAs. The decoupled charge and spin doping leads to mutually independent control of the amount of carrier and spin moments. The valence match between Mn and Zn enables the high Mn concentration up to $y = 0.15$. Figure 1.33 (b) shows the a- and c-axis lengths as a function of K concentration. While the a-axis is almost unchanged at ~ 4.13 Å, the c-axis shrinks upon K doping. This reflects the smaller atomic radius of K than Ba, and K atoms are spatially separated from the ZnAs sites. Figure 1.33 shows the resistivity of Mn-$BaZn_2As_2$ for different compositions. For Mn-free samples ($y = 0$), the resistivity changes from semiconducting ($x = 0$) to metallic behavior ($x = 0.05, 0.1$). In the Mn-doped samples ($y = 0.1$), the "bad-metallic" behavior at $x = 0$ does not change much upon hole doping, indicating strong scattering by local spins.

The magnetic properties of Mn-$BaZn_2As_2$ are summarized in Fig. 1.34. Figure 1.34 (a) shows DC magnetization measured under the magnetic field of $H = 500$ G. Clear ferromagnetic signals are obtained, and the highest T_C of 180 K is achieved for $x = 0.30$. After the publication of Ref. [84], the optimal T_C has risen up to 230 K [85]. Figures 1.34 (b) and (c) show the magnetization curves as a function of magnetic field. As shown in panel (b), the correction to the data is performed by subtracting a small T-linear component. Corrected $M(H)$ curves show ferromagnetic hysteresis curves for $x > 0.05$, and the saturated magnetization is $\sim 1.5\mu_B$. The anomalous Hall effect shown in panel (d) evidences that the ferromagnetism is

intrinsic to the DMS.

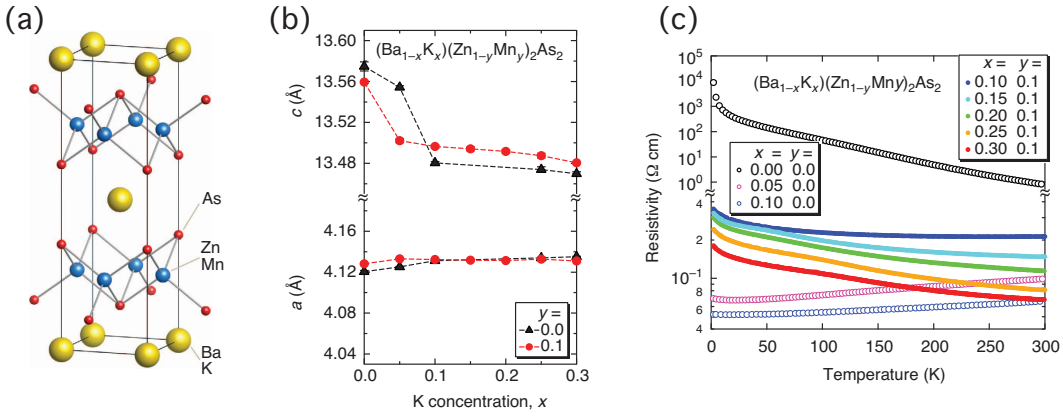

Figure 1.33: (a) Crystal structure of $Ba_{1-x}K_x(Zn_{1-y}Mn_y)_2As_2$. (b) a- and c-axis parameters as a function of K concentration. (c) Resistivity curves for different doping concentrations. Figures reproduced from Ref. [84].

After the successful growth of $LiZn_{1-x}Mn_xAs$ and $Ba_{1-x}K_x(Zn_{1-y}Mn_y)_2As_2$, $BaZn_2As_2$ in thin film is successfully grown by pulsed laser deposition method [86], opening up possibilities of fabricating functional heterostructures. Further, "1111"-type new ZnAs DMSs, $(La_{1-x}Sr_x)(Zn_{1-y}TM_y)AsO$ (TM=Mn, Fe, Co), are synthesized in bulk form [87]. They are isostructural to iron-based superconductor LaFeAsO. By its emergence, it turned out that all of the "111", "122" and "1111"-type iron arsenide superconductors have corresponding zinc arsenide DMSs. For details of these issues, the reader is referred to the original articles.

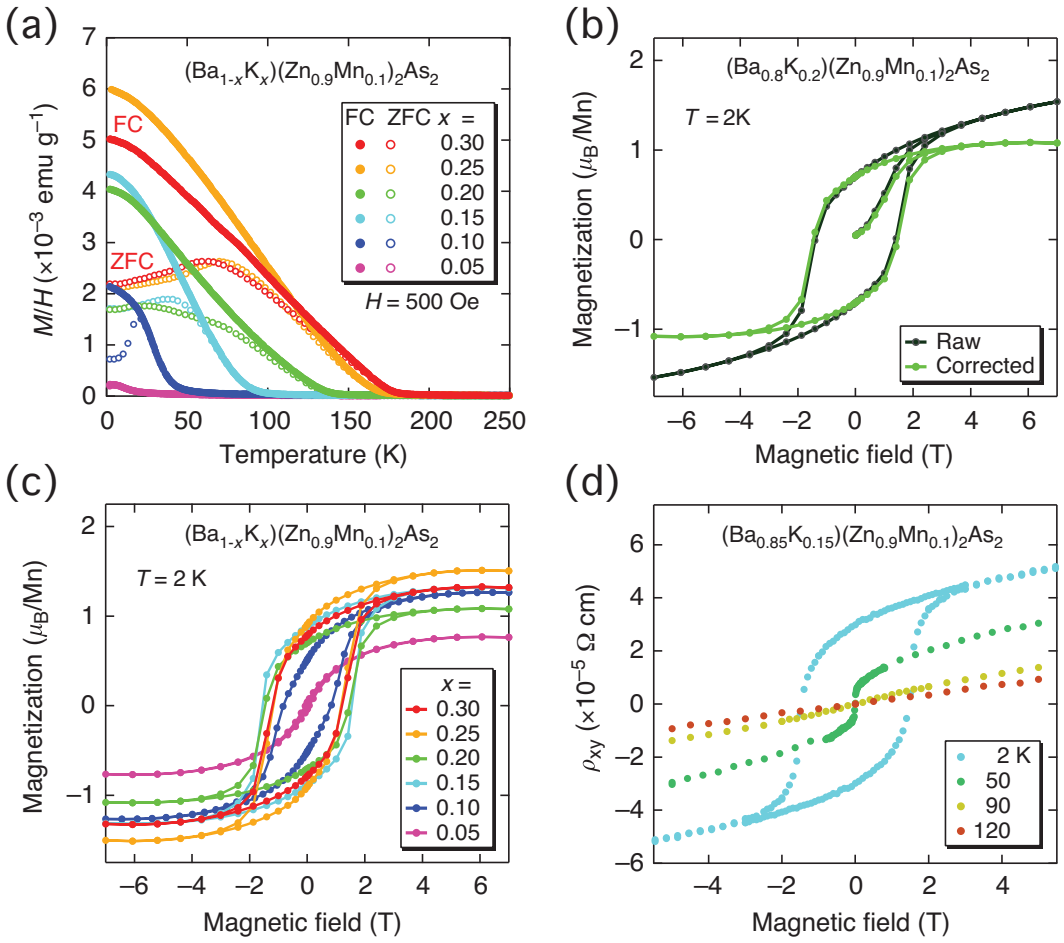

Figure 1.34: (a) Magnetization of $Ba_{1-x}K_x(Zn_{0.9}Mn_{0.1})_2As_2$ measured in $H = 500$ G for different K concentration x. ZFC and FC represent zero-field cooled and field-cooled, respectively. (b) Raw and corrected $M(H)$ curves. Corrected curves are obtained by subtracting a small T-linear contribution from the raw curves. (c) Corrected $M(H)$ curves for different compositions. (d) Hall resistance for $x = 0.15$. Anomalous Hall effect is clearly observed at $T = 2$ K. Figures reproduced from Ref. [84].

Chapter 2

Experimental methods

In this chapter we shall describe the principles of experimental methods. Angle-resolved photoemission spectroscopy (ARPES) is one of the most direct methods of probing the electronic structure in solids. X-ray absorption spectroscopy (XAS) clarifies the valence of each elements. Resonance photoemission spectroscopy is the most efficient tool to investigate the partial density of states (PDOS) of particular atomic orbitals. Time-resolved angle-resolved photoemission spectroscopy (TrARPES) is a method to investigate transient electronic states of solids by pump-probe photoemission measurement. Resonant inelastic x-ray scattering is a photon-in, photon-out inelastic scattering technique, with which various elementary excitations of solids can be clarified.

2.1 Angle-resolved photoemission spectroscopy

Electrons in solids are interacting with positive ions and electrons themselves. The non-relativistic Hamiltonian for the many-electron system is given, in the second-quantization formalism, by

$$H_e = T_e + V_{ei} + H_{ee} \tag{2.1}$$

$$\equiv \sum_\sigma \int d\boldsymbol{r} \psi_\sigma^\dagger(\boldsymbol{r})(-\frac{\Delta}{2m})\psi_\sigma(\boldsymbol{r}) + \sum_\sigma \int d\boldsymbol{r} \psi_\sigma^\dagger(\boldsymbol{r})(-\sum_j \frac{Z_j e^2}{|\boldsymbol{r}-\boldsymbol{R}_j|})\psi_\sigma(\boldsymbol{r}) \tag{2.2}$$

$$+ \frac{1}{2}\sum_{\sigma\sigma'} \int d\boldsymbol{r} \int d\boldsymbol{r'} \psi_\sigma^\dagger(\boldsymbol{r})\psi_{\sigma'}^\dagger(\boldsymbol{r'})\frac{e^2}{|\boldsymbol{r}-\boldsymbol{r'}|}\psi_{\sigma'}(\boldsymbol{r'})\psi_\sigma(\boldsymbol{r})$$

where $\psi_\sigma^\dagger(\boldsymbol{r})$ and $\psi_\sigma(\boldsymbol{r})$ are the creation and annihilation operators of the electron field, respectively. It is widely believed that the low-energy excited states of the system can be described as a collection of almost independent elementary excitations. Probing the properties of these elementary excitations and the interactions

among them enables us to understand the properties of the system. These properties are often investigated through the dynamical response of the system to external perturbations.

Many-body electron system in solids are generally well understood by one-electron approximation. This is due to the fact that quasiparticles, which is an elementary excitation with qualitatively the same physical properties as noninteracting electrons, exist for sufficiently long duration. Photoemission spectroscopy (PES) has been the most useful experimental technique in directly measuring quasiparticles.

2.1.1 Basics of photoemission spectroscopy

Figure 2.1 illustrates a schematic diagram of the principle of photoemission spectroscopy. Photoemission is a process where electrons absorb photons of sufficiently high energy $h\nu$ and escape from the sample. The knowledge on the kinetic energy E^v_{kin} of the emitted electron in the vacuum enables us to determine the initial electron energy. Conservation of energy gives

$$E^v_{\text{kin}} = h\nu - \Phi - E_{\text{B}}, \tag{2.3}$$

where $h\nu$ is the energy of the incident photons, E_{B} is the binding energy relative to the Fermi level E_F (chemical potential μ) and Φ is the work function of the material under study. The work function Φ is the energy required for the electron to escape from the solid through the surface and to reach the vaccum level E_{vac}, that is, $\Phi = E_{\text{vac}} - E_F$. In real experiments the kinetic energy (E_{kin}) measured from E_F rather than E^v_{kin} is directly observed. Then we obtain

$$E_{\text{kin}} = h\nu - E_{\text{B}}. \tag{2.4}$$

Here, we take the chemical potential μ as a reference of all energies. Since both the sample and the electron energy analyzer are grounded, the measured kinetic energy E_{kin} of the emitted electron is referred to μ (E_F).

In the mean-field (Hartree-Fock) approximation, the energy E_{B} is regarded as the energy ϵ of the electron in the solid before it was emitted. Therefore, the energy distribution of the electrons in the material can be directly mapped by the distribution of the kinetic energies of photoelectrons emitted by monochromatic incident photons.

In real systems, however, the photoemission spectra are affected by the relaxation of the entire electron system. The one-electron energy ϵ can be measured if the frozen-orbital approximation is valid. In response to the hole produced by the photoemission process, the surrounding electrons screen the hole to lower the total energy of the system. Therefore, considering the entire electron system, the binding

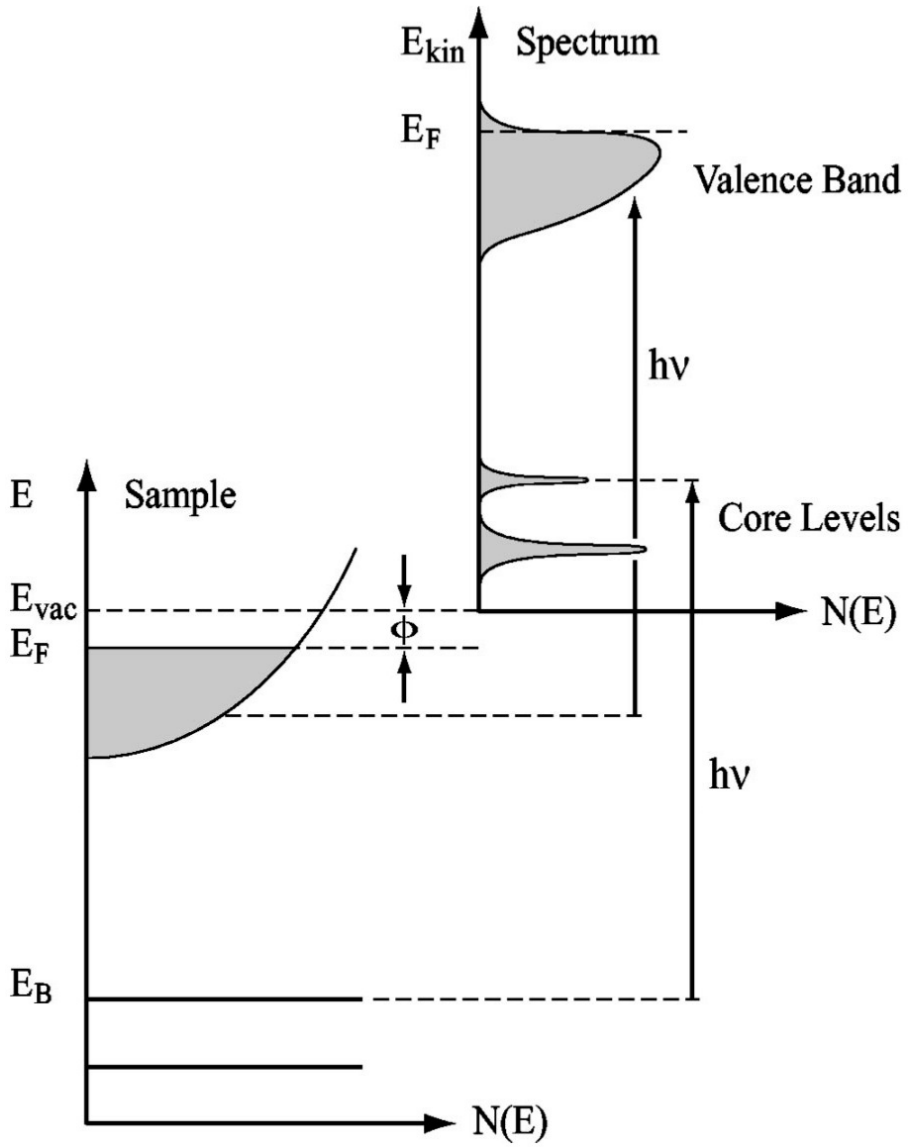

Figure 2.1: Schematic energy diagram showing the principle of photoemission spectroscopy (PES) [88]. Using the relationship $E_{\text{kin}} = h\nu - E_{\text{B}}$, the electronic structure of the solid is mapped to energy distribution curves (EDCs)

energy $E_{\rm B}$ is given by the energy difference between the N-electron initial state $E_{\rm i}^N$ and the $(N-1)$-electron final state $E_{\rm f}^{N-1}$. In other words, $E_{\rm B}$ is the energy of the hole produced by the photoemission process, including the relaxation energy of the total electron system. Thus information about electron correlations can be obtained by analyzing the photoemission spectra.

2.1.2 Relation between experimental values and crystal momentum

In ARPES not only the energies but also the momenta of the electrons in the materials are probed. Here, we briefly review the principle of ARPES [88]. In the photoexcitation process by photons with low energy, the wave number of the incident photon can be neglected, and the wave number of the electron is conserved before and after the photoexcitation except for the reciprocal lattice vector. We obtain

$$\boldsymbol{k}_{\rm f} = \boldsymbol{k}_{\rm i} + \boldsymbol{G}, \tag{2.5}$$

where $\boldsymbol{k}_{\rm i}$ and $\boldsymbol{k}_{\rm f}$ are the crystal momentum of the electron in the initial and final states, respectively, and $\boldsymbol{G} = (2n_x\pi/a, 2n_y\pi/b, 2n_z\pi/c)$ is an arbitrary reciprocal lattice vector. When the photoelectron escapes from the solid to the vacuum, part of the momentum perpendicular to the surface is lost due to the finite work function Φ, whereas the momentum parallel to the surface is conserved owing to the translational symmetry along the surface. When the momentum of the electron outside the sample is denoted by $\boldsymbol{p}$, we have

$$\boldsymbol{p}_{\parallel}/\hbar = \boldsymbol{k}_{\rm f\parallel} + \boldsymbol{G}_{\parallel}. \tag{2.6}$$

In Fig. 2.2, the geometry of an ARPES experiment is sketched. A beam of monochromatized radiation supplied either by a gas-discharge lamp or by a synchrotron radiation. As a result, electrons are emitted by photoelectric effect and escape in vacuum in all directions. By collecting the photoelectrons with an electron energy analyzer characterized by a finite acceptance angle, one measures their kinetic energy $E_{\rm kin}^v$ for given emission direction. In this way, the momentum $\boldsymbol{p}$ of the photoelectrons in vacuum is also determined: the magnitude is given by $p = \sqrt{2mE_{\rm kin}^v}$ and its components parallel ($\boldsymbol{p}_{\parallel} = \boldsymbol{p}_x + \boldsymbol{p}_y$) and perpendicular ($\boldsymbol{p}_{\perp} = \boldsymbol{p}_z$) to the sample surface are obtained in terms of the polar angle θ and azimuthal angle ϕ defined by the experiment:

$$p_x = \sqrt{2mE_{\rm kin}^v}\sin\theta\cos\phi, \tag{2.7}$$

$$p_y = \sqrt{2mE_{\rm kin}^v}\sin\theta\sin\phi, \tag{2.8}$$

$$p_z = \sqrt{2mE_{\rm kin}^v}\cos\theta, \tag{2.9}$$

where m is the free electron mass. Summarizing Eqs. (2.3), (2.5), (2.6), (2.7), and (2.8), we can directly observe both the energy $E \equiv -E_{\mathrm{B}}$ and the parallel momentum $\boldsymbol{k}_{\parallel} = (k_x, k_y)$ of the hole produced in the sample by the photoemission process as

$$k_x = \frac{\sqrt{2m(h\nu - \Phi - E_{\mathrm{B}})}}{\hbar} \sin\theta \cos\phi + \frac{2n_x\pi}{a}, \tag{2.10}$$

$$k_y = \frac{\sqrt{2m(h\nu - \Phi - E_{\mathrm{B}})}}{\hbar} \sin\theta \sin\phi + \frac{2n_y\pi}{b}. \tag{2.11}$$

For the determination of $\boldsymbol{k}_{\perp} = k_z$, which is not conserved during the photoemission process, a different approach is required as shown in Fig. 2.3. Suppose we adopt a nearly-free-electron description for the final bulk Bloch state:

$$E_{\mathrm{f}}(\boldsymbol{p}) = \frac{\boldsymbol{p}^2}{2m} + E_0 = \frac{\boldsymbol{p}_{\parallel}^2 + \boldsymbol{p}_{\perp}^2}{2m} + E_0, \tag{2.12}$$

where the electron momenta are defined in the extended-zone scheme, and E_0 is the energy of the bottom of the free electron band as indicated in Fig. 2.3. Because $E_{\mathrm{f}} = E_{\mathrm{kin}}^{v} + \Phi + \mu$, using Eqs. (2.7) (2.8), and (2.12), we obtain

$$k_{\perp} = \frac{\sqrt{2m\left(E_{\mathrm{kin}}^{v}\cos^2\theta + V_0\right)}}{\hbar}. \tag{2.13}$$

Here, $V_0 = \Phi + \mu - E_0 = E_{\mathrm{vac}} - E_0$ is the inner potential, which corresponds to the energy of the bottom of the valence band referenced to the vacuum level E_{vac}. From Eq. (2.13) and the measured values of E_{kin}^{v} and θ, if V_0 is known, one can obtain the corresponding value of $k_{\perp}$. Based on this principle, one can investigate the Fermi surface in $k_{\parallel}$-k_z plane.

2.1.3 Green's function

Using the relationship between the emission angle, $h\nu$ and crystal momentum discussed above, ARPES can be used as a direct probe of the spectral function $A(\boldsymbol{k}, \omega)$ of the system. The relationship between one-particle Green's function and the spectral function is given below [90]. For simplicity we restrict ourselves to the case of $T = 0$.

In the method of quantum field theory, one-particle Green's function, which characterizes the microscopic properties of a system, is defined as

$$G_{\alpha,\beta}(x, x') = -i \left\langle 0 \right| T(\psi_{\alpha}(x)\psi_{\beta}^{\dagger}(x')) \left| 0 \right\rangle, \tag{2.14}$$

where x and x' denotes four-coordinate $(\boldsymbol{r}, t)$, α and β denote spin indices, $|0\rangle$ denotes the ground state, and $T(\dots)$ denotes the time-ordered product. In the absence of ferromagnetism and an external magnetic field, Green's function must be spin-independent,

$$G_{\alpha,\beta} = G\delta_{\alpha,\beta}. \tag{2.15}$$

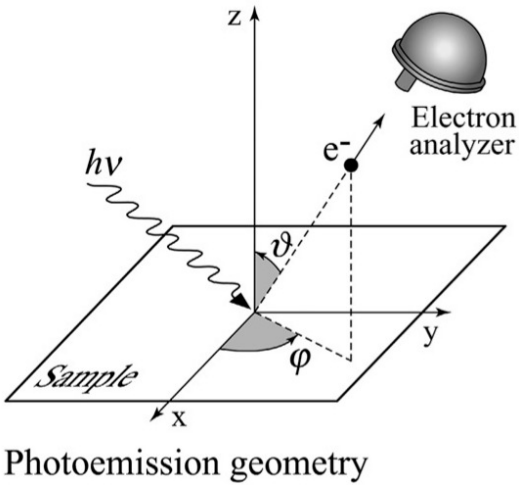

Figure 2.2: Geometry of ARPES experiment: the emission direction of the photoelectron is specified by the polar (θ) and azimuthal (ϕ) angles [89].

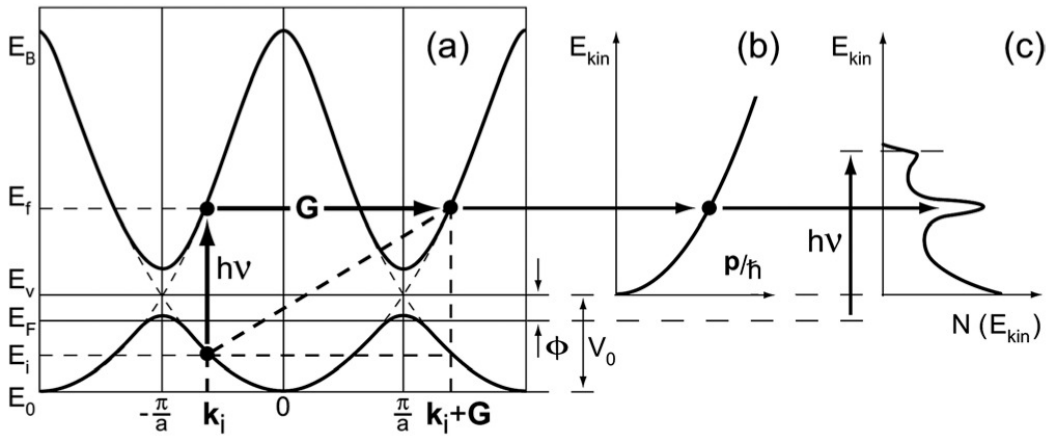

Figure 2.3: Kinematics of the photoemission process within the three-step nearly-free-electron final-state model [88]. (a) Direct optical transition in the solid (the lattice supplies the required momentum). (b) Free-electron final state in vacuum. (c) Corresponding photoelectron spectrum with a background due to scattered electrons.

In the absence of external fields, the Green's functions of homogeneous and spatially infinite systems depend only on the coordinate differences $\boldsymbol{r} - \boldsymbol{r}'$ and the time difference $t - t'$. Suppose we represent Green's function as a Fourier integral, we have

$$G(x - x') = \int G(\boldsymbol{p}, \omega) e^{i[\boldsymbol{p}\cdot(\boldsymbol{r}-\boldsymbol{r}')-\omega(t-t')]} \frac{d^4p}{(2\pi)^4}. \tag{2.16}$$

Then the function $G(\boldsymbol{p}, \omega)$ can be derived easily for a system of noninteracting particles. We insert the expression of the free-field operator

$$\psi(x) = \frac{1}{\sqrt{V}} \sum_{\boldsymbol{p}} a_{_p} e^{i[\boldsymbol{p}\cdot\boldsymbol{r}-\epsilon_0(\boldsymbol{p})t]} \tag{2.17}$$

into Eq.(2.14) and bearing in mind that all levels with $|\boldsymbol{p}| < p_0$ are occupied while those with $|\boldsymbol{p}| > p_0$ are empty, we obtain

$$G^{(0)}(x) = -\frac{i}{V} \sum_{\boldsymbol{p}} e^{i[\boldsymbol{p}\cdot\boldsymbol{r}-\epsilon_0(\boldsymbol{p})t]} \left[\theta(t)(1 - n_{\boldsymbol{p}}) - \theta(-t)n_{\boldsymbol{p}}\right], \tag{2.18}$$

where

$$n_p = \begin{cases} 1 & \text{for } |\boldsymbol{p}| < p_0, \\ 0 & \text{for } |\boldsymbol{p}| > p_0, \end{cases} \tag{2.19}$$

and $\theta(x)$ is the Heaviside step function. Going to the momentum representation, we have

$$G^{(0)}(\boldsymbol{p}, \omega) = -i \left\{ \theta(|\boldsymbol{p}| - p_0) \int_0^\infty e^{i[\omega-\epsilon_0(\boldsymbol{p})]t} dt - \theta(p_0 - |\boldsymbol{p}|) \int_0^\infty e^{-i[\omega-\epsilon_0(\boldsymbol{p})]t} dt \right\}. \tag{2.20}$$

This expression contains two integrals of the type

$$\int_0^\infty e^{ist} dt. \tag{2.21}$$

We define an integral of this type as the limit

$$\lim_{\delta\to+0} \int_0^\infty e^{ist-\delta t} dt = i \lim_{\delta\to+0} \frac{1}{s + i\delta}. \tag{2.22}$$

Using (2.20) and (2.22), we obtain

$$\begin{aligned} G^{(0)}(\boldsymbol{p}, \omega) &= \frac{\theta(|\boldsymbol{p}| - p_0)}{\omega - \epsilon_0(\boldsymbol{p}) + i\delta} + \frac{\theta(p_0 - |\boldsymbol{p}|)}{\omega - \epsilon_0(\boldsymbol{p}) - i\delta} \\ &= \frac{1}{\omega - \epsilon_0(\boldsymbol{p}) + i\delta \mathrm{sgn}(|\boldsymbol{p}| - p_0).} \end{aligned} \tag{2.23}$$

Now we consider the basic properties of Green's function of a system of interacting fermions. Going to Schrödinger operators, we obtain

$$\begin{aligned} G(\boldsymbol{r}-\boldsymbol{r},t-t') &= -i\left\langle 0\right| e^{iHt}\psi(\boldsymbol{r})e^{-iH(t-t')}\psi^{\dagger}(\boldsymbol{r}')e^{-iH't'}\left|0\right\rangle \qquad (2.24)\\ &= -i\sum_{s}\left\langle 0\right| e^{iHt}\psi(\boldsymbol{r})e^{-iHt}\left|\Psi_s\right\rangle\left\langle \Psi_s\right| e^{iHt'}\psi^{\dagger}(\boldsymbol{r}')e^{-iH't'}\left|0\right\rangle \\ &= -i\sum_{s}\psi_{0s}(\boldsymbol{r})\psi^{\dagger}_{s0}(\boldsymbol{r}')e^{i(E_s-E_0)(t-t')} \quad \text{for } t>t'. \\ G(\boldsymbol{r}-\boldsymbol{r},t-t') &= i\sum_{s'}\psi_{0s'}(\boldsymbol{r}')\psi^{\dagger}_{s'0}(\boldsymbol{r})e^{i(E_{s'}-E_0)(t-t')} \quad \text{for } t<t'. \end{aligned}$$

For a homogeneous system, the coordinate dependence of matrix elements $\psi_{nm}(\boldsymbol{r})$ and $\psi^{\dagger}_{nm}(\boldsymbol{r})$ takes the form

$$\psi_{nm}(\boldsymbol{r})=\psi_{nm}(0)e^{-i\boldsymbol{p}_{nm}\cdot\boldsymbol{r}},\psi^{\dagger}_{nm}(\boldsymbol{r})=\psi^{\dagger}_{nm}(0)e^{-i\boldsymbol{p}_{nm}\cdot\boldsymbol{r}}, \qquad (2.25)$$

where $\boldsymbol{p}_n$ is the momentum of the state n and $\boldsymbol{p}_{nm}=\boldsymbol{p}_n-\boldsymbol{p}_m$. Setting $\boldsymbol{p}_0=0$, we have

$$G(\boldsymbol{r}-\boldsymbol{r}',t-t')=-i\sum_{s}|\psi_{0s}(0)|^2e^{i\boldsymbol{p}_s\cdot(\boldsymbol{r}-\boldsymbol{r}')}e^{-i(E_s-E_0)(t-t')} \text{ for } t>t' \qquad (2.26)$$

$$G(\boldsymbol{r}-\boldsymbol{r}',t-t')=i\sum_{s'}|\psi_{0s'}(0)|^2e^{-i\boldsymbol{p}_{s'}\cdot(\boldsymbol{r}-\boldsymbol{r}')}e^{i(E_{s'}-E_0)(t-t')} \text{ for } t<t' \qquad (2.27)$$

Since the operator $\psi^{\dagger}(\boldsymbol{r})$ increases the number of electrons by unity, the summation over s for $t>t'$ is made over states with particle number equal to $N+1$. On the other hand, the summation over s' for $t<t'$ is made over states with particle number equal to $N-1$. We write

$$E_s-E_0=\epsilon_s+\mu, \qquad (2.28)$$

where $\epsilon_s=E_s-E_0(N+1)$ is the excitation energy of the system and $\mu=E_0(N+1)-E_0(N)$ is the chemical potential at $T=0$. In the same way, we write

$$E_{s'}-E_0(N)=\epsilon_{s'}-\mu', \qquad (2.29)$$

where $e_{s'}$ and μ' are the excitation energy and the chemical potential for $T=0$ of the system with $N-1$ particles. Within an error of order $1/N$, we can assume

$$\epsilon_s=\epsilon_{s'},\ \mu=\mu'. \qquad (2.30)$$

Introducing the functions

$$A(\boldsymbol{p},E)=(2\pi)^3\sum_{s}|\psi_{0s}(0)|^2\delta(\boldsymbol{p}-\boldsymbol{p}_s) \text{ for } E<\epsilon_s<E+dE \qquad (2.31)$$

$$B(\boldsymbol{p}, E) = (2\pi)^3 \sum_{s'} |\psi_{0s'}(0)|^2 \delta(\boldsymbol{p} + \boldsymbol{p}_s) \text{ for } E < \epsilon_{s'} < E + dE, \tag{2.32}$$

we express Green's function as a Fourier integral

$$G(\boldsymbol{p}, \omega) = \int_0^\infty \left[\frac{A(\boldsymbol{p}, E)}{\omega - E - \mu + i\delta} + \frac{B(\boldsymbol{p}, E)}{\omega + E - \mu - i\delta} \right] dE \tag{2.33}$$

The coefficient A and B are real and positive. Separating the real and imaginary parts of the function G, we obtain

$$\operatorname{Re} G(\boldsymbol{p}, \omega) = P \int_0^\infty \left[\frac{A(\boldsymbol{p}, E)}{\omega - E - \mu} + \frac{B(\boldsymbol{p}, E)}{\omega + E - \mu} \right] dE, \tag{2.34}$$

$$\operatorname{Im} G(\boldsymbol{p}, \omega) = \begin{cases} -\pi A(\boldsymbol{p}, \omega - \mu) & \text{for } \omega - \mu > 0, \\ \pi B(\boldsymbol{p}, \mu - \omega) & \text{for } \omega - \mu < 0. \end{cases} \tag{2.35}$$

We also define the *retarded* and *advanced* Green's function as follows:

$$G_R(x - x') = -i\theta(t - t') \langle 0 | \{\psi(x), \psi^\dagger(x')\} | 0 \rangle , \tag{2.36}$$

$$G_A(x' - x) = i\theta(t' - t) \langle 0 | \{\psi(x), \psi^\dagger(x')\} | 0 \rangle . \tag{2.37}$$

Performing the same operations as used to derive Eq.(2.33), we obtain

$$G_R(\boldsymbol{p}, \omega) = \int_0^\infty \left[\frac{A(\boldsymbol{p}, E)}{\omega - E - \mu + i\delta} + \frac{B(\boldsymbol{p}, E)}{\omega + E - \mu + i\delta} \right] dE, \tag{2.38}$$

$$G_A(\boldsymbol{p}, \omega) = G_R^*(\boldsymbol{p}, \omega), \tag{2.39}$$

$$G_R(\boldsymbol{p}, \omega) = \begin{cases} G(\boldsymbol{p}, \omega) & \text{for } \omega > \mu, \\ G^*(\boldsymbol{p}, \omega) & \text{for } \omega < \mu. \end{cases} \tag{2.40}$$

It follows from eq. (2.40) that G_R is the analytic continuation of G from the half-line $\omega > \mu$.

2.1.4 Spectral function and retarded Green's function

In the process of photoemission, one impinges light on the electron system and change the number of electron from N to $N - 1$ [88]. The quantity measured here is the change in the total momentum and energy. Suppose we take out one electron from the ground state $|\Psi_g^N\rangle$ and the total momentum change is $\boldsymbol{k}$. Right after the photoemission, the system is expressed as $c_{\boldsymbol{k}} |\Psi_g^N\rangle$, where $c_{\boldsymbol{k}}$ is the annihilation operator of a bloch state with momentum $\boldsymbol{k}$. Since the final state has $N-1$ particles, the relaxed state of photoexcited system can be expanded using eigenstates with $N - 1$ particles; the spectral function obtained by photoemission spectroscopy is thus

$$A_{PES}(\boldsymbol{k}, \omega) = \sum_i |\langle \Psi_i^{N-1} | c_{\boldsymbol{k}} | \Psi_g^N \rangle|^2 \delta(\omega + E_i^{N-1} - E_g^N). \tag{2.41}$$

Similarly, in the process of inverse photoemission, electrons are impinged to the electron system. The measured quantity is the emitted light and the gain of momentum when the system absorbs the incoming electrons. The spectral function obtained by inverse photoemission spectroscopy is given by

$$A_{IPES}(\boldsymbol{k},\omega) = \sum_i |\langle \Psi_i^{N+1}| \, c_{\boldsymbol{k}}^\dagger \, |\Psi_g^N\rangle|^2 \delta(\omega - E_i^{N+1} + E_g^N). \tag{2.42}$$

ω is defined as $\omega \equiv \varepsilon_{kin} + V_0 - h\nu$. $\omega < \mu$ corresponds to the photoemission, and $\omega > \mu$ corresponds to inverse photoemission. We define the spectral function as the sum of these two terms:

$$A(\boldsymbol{k},\omega) = \sum_i |\langle \Psi_i^{N-1}| \, c_{\boldsymbol{k}} \, |\Psi_g^N\rangle|^2 \delta(\omega + E_i^{N-1} - E_g^N) \tag{2.43}$$

$$+ \sum_i |\langle \Psi_i^{N+1}| \, c_{\boldsymbol{k}}^\dagger \, |\Psi_g^N\rangle|^2 \delta(\omega - E_i^{N+1} + E_g^N). \tag{2.44}$$

The spectral function $A(\boldsymbol{k},\omega)$ is related to retarded Green's function $G_R(\boldsymbol{k},\omega)$ by the relation

$$A(\boldsymbol{k},\omega) = -\frac{1}{\pi} \operatorname{Im} G_R(\boldsymbol{k},\omega). \tag{2.45}$$

In order to prove Eq. (2.45), we take the Fourier transform of Eq. (2.37). For a homogeneous system, retarded Green's function is dependent only on the difference of the coordinate and therefore

$$G_R(\boldsymbol{k},\boldsymbol{k}';t-t') \equiv \int d\boldsymbol{x} e^{-i\boldsymbol{k}\cdot\boldsymbol{x}} \int d\boldsymbol{x}' e^{i\boldsymbol{k}'\cdot\boldsymbol{x}'} G_R(\boldsymbol{x}-\boldsymbol{x}',t-t') \tag{2.46}$$

$$= \int d(\boldsymbol{x}-\boldsymbol{x}') \int d\boldsymbol{x}' e^{-i\boldsymbol{k}\cdot(\boldsymbol{x}-\boldsymbol{x}')} e^{i(\boldsymbol{k}'-\boldsymbol{k})\cdot\boldsymbol{x}'} G_R(\boldsymbol{x}-\boldsymbol{x}',t-t') \tag{2.47}$$

$$\equiv \delta_{\boldsymbol{k}\boldsymbol{k}'} G_R(\boldsymbol{k},t-t').$$

Expressing the field operator by plane-wave states, $\psi(\boldsymbol{x}) = \sum_{\boldsymbol{k}} c_{\boldsymbol{k}} e^{i\boldsymbol{k}\cdot\boldsymbol{x}}$, $G_R(\boldsymbol{k},t)$ is given by

$$G_R(\boldsymbol{k},t) = -i\theta(t) \left\langle \Psi_g^N \right| \{c_{\boldsymbol{k}}(t), c_{\boldsymbol{k}}^\dagger\} \left| \Psi_g^N \right\rangle. \tag{2.48}$$

Taking its Fourier transform and inserting the completeness relation $\hat{\mathbf{1}} = \sum_{n,i} |\Psi_i^n\rangle \langle \Psi_i^n|$,

we obtain

$$
\begin{aligned}
G_R(\boldsymbol{k},\omega) &= \int dt e^{i\omega t+\delta t} G_R(\boldsymbol{k},t) \qquad (2.49)\\
&= \int_0^\infty dt e^{i\omega t+\delta t}(-i)\sum_{n,i}[\langle\Psi_g^N|\, e^{iHt} c_{\boldsymbol{k}} e^{-iHt}\,|\Psi_i^n\rangle\,\langle\Psi_i^n|\, c_{\boldsymbol{k}}^\dagger\,|\Psi_g^N\rangle \\
&\qquad + \langle\Psi_g^N|\, c_{\boldsymbol{k}}^\dagger\,|\Psi_i^n\rangle\,\langle\Psi_i^n|\, e^{iHt} c_{\boldsymbol{k}} e^{-iHt}\,|\Psi_g^N\rangle] \\
&= (-i)\sum_i \int_0^\infty dt e^{i(\omega+E_g^N-E_s^{N+1})t+\delta t}\,\langle\Psi_g^N|\, c_{\boldsymbol{k}}\,|\Psi_i^{N+1}\rangle\,\langle\Psi_i^{N+1}|\, c_{\boldsymbol{k}}^\dagger\,|\Psi_g^N\rangle \\
&+ (-i)\sum_{i'} \int_0^\infty dt e^{i(\omega+E_s^{N-1}-E_g^N)t+\delta t}\,\langle\Psi_g^N|\, c_{\boldsymbol{k}}^\dagger\,|\Psi_i^{N-1}\rangle\,\langle\Psi_i^{N-1}|\, c_{\boldsymbol{k}}\,|\Psi_g^N\rangle \\
&= \sum_i \frac{1}{\omega+E_g^N-E_s^{N+1}}\,\langle\Psi_g^N|\, c_{\boldsymbol{k}}\,|\Psi_i^{N+1}\rangle\,\langle\Psi_i^{N+1}|\, c_{\boldsymbol{k}}^\dagger\,|\Psi_g^N\rangle \\
&+ \sum_{i'} \frac{1}{\omega+E_s^{N-1}-E_g^N}\,\langle\Psi_g^N|\, c_{\boldsymbol{k}}^\dagger\,|\Psi_i^{N-1}\rangle\,\langle\Psi_i^{N-1}|\, c_{\boldsymbol{k}}\,|\Psi_g^N\rangle\,.
\end{aligned}
$$

Comparison with Eq. (2.44) proves Eq. (2.45).

2.1.5 Electron self-energy, effective mass and damping of quasi-particles

In this section, we only treat retarded Green's function and drop the subscript R. Green's function for free particle is given, from (2.24) and (2.40), by

$$G^{(0)}(\boldsymbol{k},\omega) = \frac{1}{\omega-\epsilon_{\boldsymbol{k}}+i\delta}, \qquad (2.50)$$

where $\epsilon_{\boldsymbol{k}}$ is one-particle energy. In the presence of electron-electron interactions, the crystal momentum $\boldsymbol{k}$ is still a good quantum number. We define *self-energy* $\Sigma(\boldsymbol{k},\omega)$ by the following relation:

$$\Sigma(\boldsymbol{k},\omega) = G^{(0)}(\boldsymbol{k},\omega)^{-1} - G(\boldsymbol{k},\omega)^{-1} \qquad (2.51)$$

i.e.

$$G(\boldsymbol{k},\omega)^{-1} = \frac{1}{\omega-\epsilon_{\boldsymbol{k}}-\Sigma(\boldsymbol{k},\omega)} \qquad (2.52)$$

The spectral function $A(\boldsymbol{k},\omega)$ takes the form

$$A(\boldsymbol{k},\omega) = -\frac{1}{\pi}\,\mathrm{Im}\,G(\boldsymbol{k},\omega) = -\frac{1}{\pi}\frac{\mathrm{Im}\,\Sigma(\boldsymbol{k},\omega)}{(\omega-\epsilon_{\boldsymbol{k}}-\mathrm{Re}\,\Sigma(\boldsymbol{k},\omega))^2+(\mathrm{Im}\,\Sigma(\boldsymbol{k},\omega)^2)} \qquad (2.53)$$

The energy distribution curve (EDC) is defined as $A(\boldsymbol{k},\omega)$ with $\boldsymbol{k}$ fixed and the momentum distribution curve is defined as $A(\boldsymbol{k},\omega)$ with ω fixed. Neglecting the energy dependence of the self-energy, it is clear from (2.53) that EDC near the quasiparticle peak is approximated by a Lorentzian function.

Green's function of free electrons $G^{(0)}(\boldsymbol{k},\omega)$ has a pole at $\epsilon_{\boldsymbol{k}} = \frac{k^2}{2m}$. Let us assume that the interacting Green's function also has a pole:

$$G(\boldsymbol{k},\omega) \approx \frac{1}{\omega - \tilde{\epsilon_{\boldsymbol{k}}}}, \tag{2.54}$$

where $\tilde{\epsilon_{\boldsymbol{k}}}$ represents the spectrum of *renormalized* quasiparticles. The spectrum $\tilde{\epsilon_{\boldsymbol{k}}}$ is given by the equation:

$$\tilde{\epsilon_{\boldsymbol{k}}} - \epsilon_{\boldsymbol{k}} - \mathrm{Re}\,\Sigma(\boldsymbol{k},\tilde{\epsilon_{\boldsymbol{k}}}) = 0, \tag{2.55}$$

where we have neglected $\mathrm{Im}\,\Sigma(\boldsymbol{k},\omega)$, which determines the quasiparticle damping rate as we will see below. Expanding the self-energy in the vicinity of the pole, we obtain

$$G(\boldsymbol{k},\omega) = \frac{1}{\omega - \epsilon_{\boldsymbol{k}} - \Sigma(\boldsymbol{k},\omega)} = \frac{1}{\omega - \epsilon_{\boldsymbol{k}} - \Sigma(\boldsymbol{k},\tilde{\epsilon_{\boldsymbol{k}}}) - \frac{\partial\Sigma}{\partial\omega}|_{\omega=\tilde{\epsilon_{\boldsymbol{k}}}}(\omega - \tilde{\epsilon_{\boldsymbol{k}}})}. \tag{2.56}$$

Taking into account (2.55), we can rewrite (2.56) in the following form:

$$G(\boldsymbol{k},\omega) = \frac{1}{\omega - \tilde{\epsilon_{\boldsymbol{k}}} - \frac{\partial\Sigma}{\partial\omega}|_{\omega=\tilde{\epsilon_{\boldsymbol{k}}}}(\omega - \tilde{\epsilon_{\boldsymbol{k}}})} = \frac{\frac{1}{1-\frac{\partial\Sigma}{\partial\omega}|_{\omega=\tilde{\epsilon_{\boldsymbol{k}}}}}}{\omega - \tilde{\epsilon_{\boldsymbol{k}}}} \equiv \frac{Z_{\boldsymbol{k}}}{\omega - \tilde{\epsilon_{\boldsymbol{k}}}}, \tag{2.57}$$

where we have introduced the *residue* at the quasiparticle pole:

$$Z_{\boldsymbol{k}} = \frac{1}{1 - \frac{\partial\Sigma}{\partial\omega}|_{\omega=\tilde{\epsilon_{\boldsymbol{k}}}}}. \tag{2.58}$$

From this expression $Z_{\boldsymbol{k}}$ is the wave function renormalization factor. From general grounds, $Z_{\boldsymbol{k}} \leq 1$ and the equality is reached only for the noninteracting Fermi gas. The spectral function corresponding to Green's function (2.57) is given by

$$A(\boldsymbol{k},\omega) = Z_{\boldsymbol{k}}\delta(\omega - \tilde{\epsilon_{\boldsymbol{k}}}). \tag{2.59}$$

$Z_{\boldsymbol{k}} < 1$ means that in a system with interaction the quasiparticle contribution to $A(\boldsymbol{k},\omega)$ is reduced due to the appearance of an additional multi-particle (incoherent) contribution to the spectral function. Finite lifetime of the quasiparticle leads to the finite width of the peak.

Suppose now that the spectrum of renormalized quasiparticles can be approximated by an enhanced effective mass:

$$\tilde{\epsilon_{\boldsymbol{k}}} = \frac{k^2}{2m^*}. \tag{2.60}$$

Using the relationship $\frac{1}{2m^*} = \frac{\partial \tilde{\epsilon_{\boldsymbol{k}}}}{\partial (k^2)}$, we can derive the following formula:

$$\frac{m^*}{m} = \frac{1 - \frac{\partial \Sigma}{\partial \omega}|_{\omega=\tilde{\epsilon_{\boldsymbol{k}}}}}{1 + \frac{\partial \Sigma}{\partial \epsilon_{\boldsymbol{k}}}} = \frac{1}{Z_{\boldsymbol{k}}} \frac{1}{1 + \frac{\partial \Sigma}{\partial \epsilon_{\boldsymbol{k}}}}. \tag{2.61}$$

This gives an important relationship between the mass renormalization m^*/m and the residue at the pole of Greens function $Z_{\boldsymbol{k}}$. In the simplest case, when the self-energy has no $\boldsymbol{k}$ dependence, this relation becomes simple:

$$\frac{m^*}{m} = \frac{1}{Z_{\boldsymbol{k}}}, \tag{2.62}$$

so that the effective mass in a system with interaction is enhanced in comparison with the case of free electrons.

In order for $A(\boldsymbol{k}, \omega)$ to be positive, it follows from (2.53) that

$$\operatorname{Im} \Sigma(\boldsymbol{k}, \omega) < 0. \tag{2.63}$$

We consider the case where the interactions are sufficiently weak. Since $\Sigma(\boldsymbol{k}, \omega)$ is small, the solution to $\omega - \epsilon_{\boldsymbol{k}} - \Sigma(\boldsymbol{k}, \omega) = 0$ is close to $\epsilon_{\boldsymbol{k}}$. Writing $\omega = \epsilon^*_{\boldsymbol{k}} - i\gamma_{\boldsymbol{k}}$, we obtain

$$\epsilon^*_{\boldsymbol{k}} = \epsilon_{\boldsymbol{k}} + \operatorname{Re} \Sigma(\boldsymbol{k}, \epsilon^*_{\boldsymbol{k}} - i\gamma_{\boldsymbol{k}}) \approx \epsilon_{\boldsymbol{k}} + \operatorname{Re} \Sigma(\boldsymbol{k}, \epsilon^*_{\boldsymbol{k}}), \tag{2.64}$$

$$\gamma_{\boldsymbol{k}} = -\operatorname{Im} \Sigma(\boldsymbol{k}, \epsilon^*_{\boldsymbol{k}} - i\gamma_{\boldsymbol{k}}) \approx -\operatorname{Im} \Sigma(\boldsymbol{k}, \epsilon^*_{\boldsymbol{k}}). \tag{2.65}$$

Green's function becomes

$$G(\boldsymbol{k}, \omega) \simeq \frac{1}{\omega - \epsilon_{\boldsymbol{k}} + i\gamma_{\boldsymbol{k}}} \tag{2.66}$$

On the other hand, Green's function in time representation

$$G(\boldsymbol{k}, t) = -i\theta(t) \left\langle \Psi^N_g \right| \left[c_{\boldsymbol{k}}(t) c^\dagger_{\boldsymbol{k}} + c^\dagger_{\boldsymbol{k}} c_{\boldsymbol{k}}(t) \right] \left| \Psi^N_g \right\rangle \tag{2.67}$$

has the following physical meanings. The first term is a product of $c_{\boldsymbol{k}} \left| \Psi^N_g \right\rangle$, the state at $t = 0$ where one electron with momentum $\boldsymbol{k}$ is added to the ground state, and $c_{\boldsymbol{k}}(t) \left| \Psi^N_g \right\rangle$, the state at t where one electron with momentum $\boldsymbol{k}$ is added to the ground state. This term represents the estimate of how much the original component

remains at t. In a similar manner, the latter term corresponds to that of a hole. Taking the Fourier transform of (2.66), we obtain

$$G(\boldsymbol{k},t) = \int \frac{d\omega}{2\pi} e^{-i\omega t} G(\boldsymbol{k},\omega) \tag{2.68}$$

$$\simeq \int \frac{d\omega}{2\pi} \frac{e^{-i\omega t}}{\omega - \epsilon^*_{\boldsymbol{k}} + i\gamma_{\boldsymbol{k}}} \tag{2.69}$$

$$= -ie^{-i\epsilon^*_{\boldsymbol{k}} t} e^{-\gamma_{\boldsymbol{k}} t}. \tag{2.70}$$

This expression tells us that Green's function represents the propagation of quasiparticle with energy $\epsilon^*_{\boldsymbol{k}}$ and that the amplitude decays with its lifetime $\sim 1/\gamma_{\boldsymbol{k}}$. It is common to define the lifetime of a quasiparticle $\tau_{\boldsymbol{k}} = \frac{1}{2\gamma_{\boldsymbol{k}}}$. Thus the width of a quasiparticle peak, $\mathrm{Im}\,\Sigma$, represents the inverse of the lifetime of the quasiparticle.

2.1.6 Photoemission matrix element

The photoemission process can be described by applying the time-dependent perturbation theory to the interactions of electrons with the classical radiation field [91]. Here, we here treat the electromagnetic field as a classical field rather than a quantized field. The basic Hamiltonian in the Coulomb gauge with $|\boldsymbol{A}|^2$ omitted is given by

$$H = \frac{\boldsymbol{p}^2}{2m} + e\phi(\boldsymbol{x}) - \frac{e}{mc}\boldsymbol{A}\cdot\boldsymbol{p}. \tag{2.71}$$

In order to be specific, we shall work with a linearly polarized monochromatic plane wave

$$\boldsymbol{A} = 2A_0\hat{\boldsymbol{\varepsilon}}\cos\left(\frac{\omega}{c}\hat{\boldsymbol{n}}\cdot\boldsymbol{x} - \omega t\right), \tag{2.72}$$

$$\phi(\boldsymbol{x}) = 0, \tag{2.73}$$

where $\boldsymbol{\epsilon}$ and $\boldsymbol{n}$ denote the linear polarization of the electric field and the propagation direction, respectively. We treat $-\frac{e}{mc}\boldsymbol{A}\cdot\boldsymbol{p}$ as the time-dependent perturbation and rewrite it as

$$-\frac{e}{mc}\boldsymbol{A}\cdot\boldsymbol{p} = -\frac{e}{mc}A_0\hat{\boldsymbol{\varepsilon}}\cdot\boldsymbol{p}[e^{(i\frac{w}{c}\hat{\boldsymbol{n}}\cdot\boldsymbol{x}-i\omega t)} + e^{(-i\frac{w}{c}\hat{\boldsymbol{n}}\cdot\boldsymbol{x}+i\omega t)}]. \tag{2.74}$$

Since a harmonic perturbation of the type

$$V(t) = Ve^{i\omega t} + V^\dagger e^{-i\omega t} \tag{2.75}$$

brings about stimulated emission (the former term) and absorption (the latter term), we now focus on the $e^{-i\omega t}$ term in eq. (2.74). Fermi's golden rule gives the transition probability per unit time as

$$w_{i\to n} = \frac{2\pi}{\hbar}\frac{e^2}{m^2c^2}|A_0|^2|\left\langle n\right|e^{i\frac{\omega}{c}\hat{\boldsymbol{n}}\cdot\boldsymbol{x}}\hat{\boldsymbol{\varepsilon}}\cdot\boldsymbol{p}\left|i\right\rangle|^2\delta(E_n - E_i - \hbar\omega). \tag{2.76}$$

When $|n\rangle$ forms a continuum, we integrate the expression with density of states $\rho(E_n)$.

We now discuss the photoemission process, that is, the ejection of an electron when electrons are placed in the radiation field. The process is the transition from an initial state $|i\rangle$ in a solid with $E < \mu$ to a final state ket $|\boldsymbol{k}\rangle$ in the continuum state with $E > \mu$. This approximation is valid if the final-state electron is not too slow and the effect of photoemission final states can be neglected. Since the final states form a continuum, we have to integrate the expression of Eq. (2.74) with the density of final states. The final expression for the differential cross section for the photoelectric effect is given by

$$\frac{d\sigma}{d\Omega} = \frac{4\pi^2\alpha\hbar}{m^2\omega} |\langle \boldsymbol{k}| e^{i(\frac{\omega}{c})\hat{\boldsymbol{n}}\cdot\boldsymbol{x}} \hat{\boldsymbol{\varepsilon}} \cdot \boldsymbol{p} |i\rangle|^2 \frac{mkL^3}{\hbar^2(2\pi)^3}. \tag{2.77}$$

ARPES usually makes use of 20-100 eV (62-100 nm) photons. Since the wavelength of the radiation field is much longer than the atomic dimension ($\sim$Å), the series

$$e^{i\frac{\omega}{c}\hat{\boldsymbol{n}}\cdot\boldsymbol{x}} = 1 + i\frac{\omega}{c}\hat{\boldsymbol{n}} + \dots \tag{2.78}$$

can be approximated by its leading term, 1. Now we have the matrix element

$$\langle n| e^{i\frac{\omega}{c}\hat{\boldsymbol{n}}\cdot\boldsymbol{x}} \hat{\boldsymbol{\varepsilon}} \cdot \boldsymbol{p} |i\rangle \simeq \langle n| \hat{\boldsymbol{\varepsilon}} \cdot \boldsymbol{p} |i\rangle . \tag{2.79}$$

Using the commutation relation

$$[\boldsymbol{r}, H_0] = \frac{i\hbar\boldsymbol{p}}{m}, \tag{2.80}$$

we obtain

$$\begin{aligned} \langle n| \hat{\boldsymbol{\varepsilon}} \cdot \boldsymbol{p} |i\rangle &= \frac{m}{i\hbar} \langle n| \hat{\boldsymbol{\varepsilon}} \cdot [\boldsymbol{r}, H_0] |i\rangle \\ &= im\omega_{ni} \langle n| \hat{\boldsymbol{\varepsilon}} \cdot \boldsymbol{r} |i\rangle . \end{aligned} \tag{2.81}$$

Because the transition matrix element is approximated by that of the dipole operator, this approximation is called the electric dipole approximation. Applying this approximation to eq. (2.77), the differential cross section for the photoelectric effect is proportional to the square of the matrix element of the dipole operator:

$$\frac{d\sigma}{d\Omega} \propto |\langle \boldsymbol{k}| \hat{\boldsymbol{\varepsilon}} \cdot \boldsymbol{r} |i\rangle|^2. \tag{2.82}$$

2.2 X-ray absorption spectroscopy

The measurement of photo-absorption by the excitation of core-level electrons into unoccupied states as a function of photon energy is called x-ray absorption spectroscopy. The photo absorption intensity is given by

$$I(\omega) = \sum_f |\langle f| T |i\rangle|^2 \delta(E_i - E_f - \hbar\omega), \tag{2.83}$$

where T is the dipole transition operator. In the $3d$ transition metal compounds, transition-metal $2p$ XAS spectra reflect the valence, the spin states and the crystal-field splitting of the $3d$ states.

There are mainly three methods for XAS measurements: the transmission mode, the total-electon-yield (TEY) mode, and the total-fluorescence-yield (TFY) mode. In the transmission mode, the original intensity of x-rays and the intensity of transmitted x-rays are counted. Although the transmission-mode is a standard method for hard x-rays, it is difficult to perform in the soft x-ray range due to the strong interaction of light with matter. In the TEY mode, all the electrons emitted from the sample is collected and a good signal-to-noise ratio is expected. We measure the electric current which flows between the ground and the sample, in proportion to the intensity of the electron emission that follows the x-ray absorption. XAS spectra are obtained by dividing the sample current by the mirror current, which is proportional to the incident photon flux. In the TFY mode, the fluorescent light emitted after the photo-absorption is measured. The TFY mode is considered to be bulk sensitive but is distorted by self-absorption, while the TEY mode is surface sensitive and is little influenced by self-absorption. In the following work, we employ the TEY mode for better statistics unless otherwise stated.

2.3 Resonance photoemission spectroscopy

Photons with continuous energy spectrum are available in Synchrotron radiation facilities. A schematic diagram of resonant PES is depicted in Fig. 2.4. Suppose the energy of the incident photon is equal to the energy difference between the p core levels and the valence d states. Along with the direct photoemission the process of a valence d electron

$$p^6 d^N + h\nu \rightarrow p^6 d^{N-1} + e^-, \tag{2.84}$$

the photo-absorption and subsequent Auger-type decay, called Coster-Krönig decay occur:

$$p^6 d^N + h\nu \rightarrow p^5 d^{N+1} \rightarrow p^6 d^{N-1} + e^-. \tag{2.85}$$

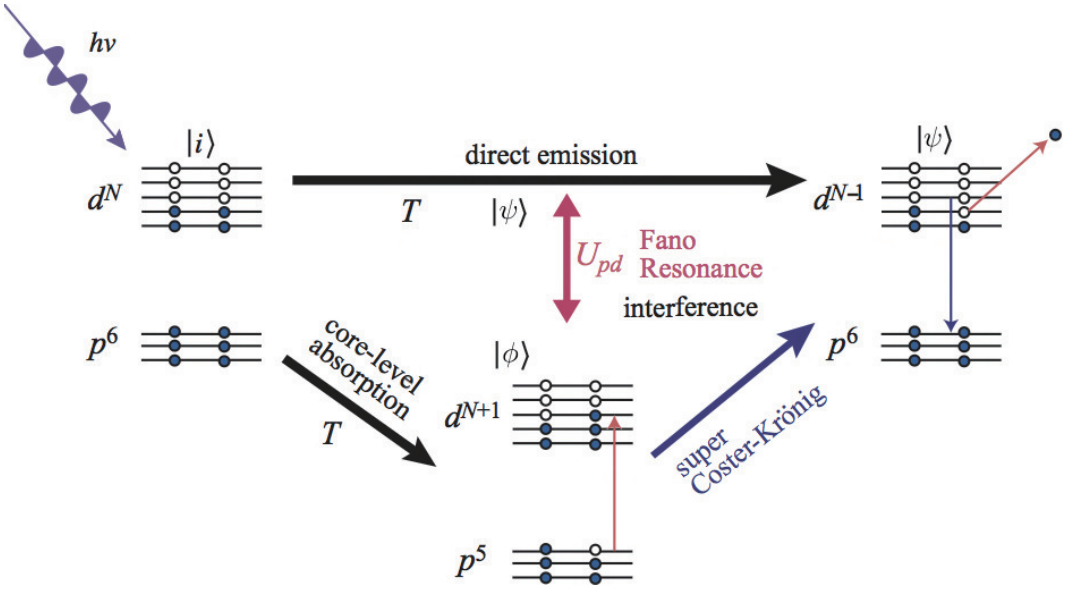

Figure 2.4: Schematic diagram of resonance photoemission spectroscopy. ψ and ϕ denote the continuum and discrete states, respectively.

The final states of these two processes have the same electron configuration, and therefore a quantum-mechanical interference will occur. The photoemission intensity is resonantly enhanced and shows a so-called Fano profile [92]. Since this enhancement takes place only for the d orbitals, one can obtain the d partial density of states in the compound.

In the $p \rightarrow d$ photoemission processes, the Fano resonance is derived from configuration interaction between the $3d$ electron emitted electronic configuration $p^6 d^{N-1}$ as a continuum state $\psi(E)$ with energy E and the core-excited electronic configuration $p^5 d^{N+1}$ as a discrete state φ with energy E_φ. These states are assumed to be orthogonal and normalized as

$$\langle\varphi|\varphi\rangle = 1,\ \langle\psi(E)|\psi(E')\rangle = \delta(E - E'),\ \langle\psi(E)|\varphi\rangle = 0. \tag{2.86}$$

The matrix elements belonging to the subset of states $\psi(E)$ and φ are indicated by

$$\langle\varphi|\mathcal{H}|\varphi\rangle = E_\varphi, \tag{2.87}$$
$$\langle\psi(E)|\mathcal{H}|\varphi\rangle = V(E), \tag{2.88}$$
$$\langle\psi(E')|\mathcal{H}|\psi(E)\rangle = E\delta(E' - E), \tag{2.89}$$

where $\mathcal{H}$ is the Hamiltonian of the system. The off-diagonal matrix element $V(E)$ originates from the Coulomb interaction in $\mathcal{H}$, that is, $V(E) = \langle p^6 d^{N-1}|e^2/r|p^5 d^{N+1}\rangle$, and is treated as configuration interaction between φ and $\psi(E)$. The corresponding

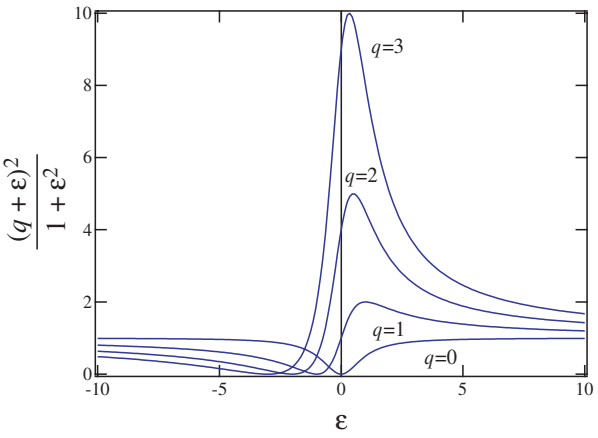

Figure 2.5: Fano line shapes for different values of q.

eigenstate has the form

$$\Psi(E) = a\varphi + \int dE' b_{E'} \psi(E'). \tag{2.90}$$

The second term represents modulated $\psi(E)$ and the sum of the two terms yield the *phase shift* Δ due to the configuration interaction between φ and $\psi(E)$, which is given by

$$\Delta = -\arctan \frac{\pi |V(E)|^2}{E - E_\varphi - F(E)}, \tag{2.91}$$

where

$$F(E) = \mathcal{P} \int dE' \frac{|V(E)|^2}{E - E'}. \tag{2.92}$$

The probability of excitation of the state $\Psi(E)$ is represented as the squared matrix element of the transition operator T between the initial state i ($p^6 d^N$ configuration) and the state $\Psi(E)$. The ratio of the transition probability $|\langle \Psi(E)|T|i\rangle|^2$ to the unperturbed $|\langle \psi(E)|T|i\rangle|^2$ can be represented by

$$\frac{|\langle \Psi(E)|T|i\rangle|^2}{|\langle \psi(E)|T|i\rangle|^2} = \frac{(q+\varepsilon)^2}{1+\varepsilon^2}, \tag{2.93}$$

where

$$\varepsilon = -\cot \Delta = \frac{E - E_\varphi - F(E)}{\pi |V(E)|^2}, \tag{2.94}$$

$$q = \frac{\langle \varphi|T|i\rangle + \mathcal{P} \int dE' \langle \varphi|\mathcal{H}|\psi(E')\rangle \langle \psi(E')|T|i\rangle / (E - E')}{\pi \langle \varphi|\mathcal{H}|\psi(E)\rangle \langle \psi(E)|T|i\rangle}, \tag{2.95}$$

are the reduced energy variable and the parameter denotes modification of the discreate state φ. Figure 2.5 shows the line shapes of Eq. (2.93) for different values of q, which shows clear enhancement near $\varepsilon = 0$. Since the photoemission intensity is proportianl to $|\langle\Psi(E)|T|i\rangle|^2$ when the energy of the incident photon is equal to that of the $p \to d$ excitation, one can extract the d partial density of states in the valence band by the $p \to d$ RPES.

2.4 ARPES system at Photon Factory 28A

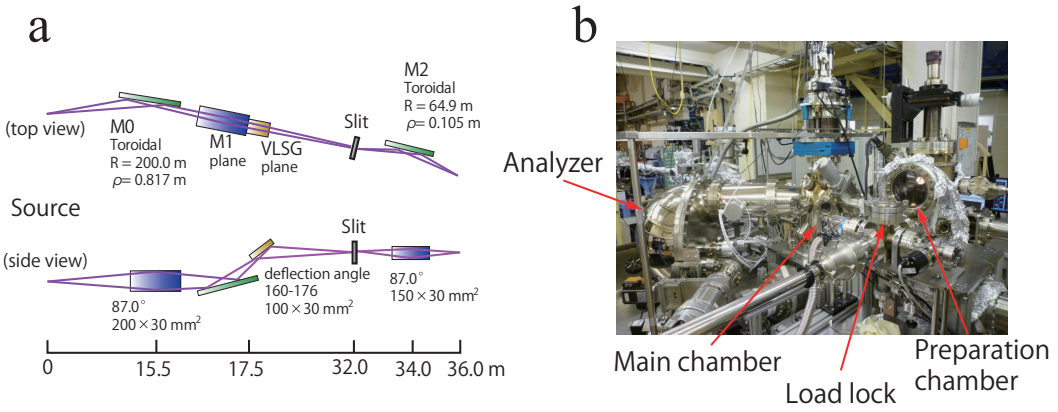

Figure 2.6: ARPES measurement system at PF beam line 28A. (a) Schematic layout of beamline 28A. (b) Overview of measurement chambers.

Now we describe the beamline 28A of Photon Factory (PF) in High Energy Accelerator Research Organization (KEK) and the measurement system. The beamline 28A is an undulator beamline with a Spherical Grating Monochromator (SGM) [Fig. 2.7 (a)] . Photons of 30-90 eV with positive/negative circular polarizations and a linear polarization ($\boldsymbol{E}$ horizontal) are available. The endstation of the beamline is composed of three chambers: a load lock chamber, a preparation chamber, and an ARPES measurement chamber (main chamber) (Fig. 2.7). Samples are cleaved *in situ* in the main chamber to obtain fresh surfaces. In the ARPES chamber a hemispherical analyzer Scienta SES2002 with a two-dimensional multi-channel plate (MCP) detection system is attached. Two rotational degrees of freedom are achieved by two-axis sample manipulator (i-Gonio). Since the analyzer slit is fixed parallel to the ground, Fermi Surface mapping is performed by sweeping the tilt (ϕ) angle. Samples can be easily transferred between chambers with horizontal transfer rods. The vacuum level of the main chamber reaches down to $\sim 10^{-11}$ Torr, which keeps the sample surface sufficiently clean for $\sim$24 hours.

2.5 ARPES system at Stanford Synchrotron Radiation Lightsource beamline 5-4

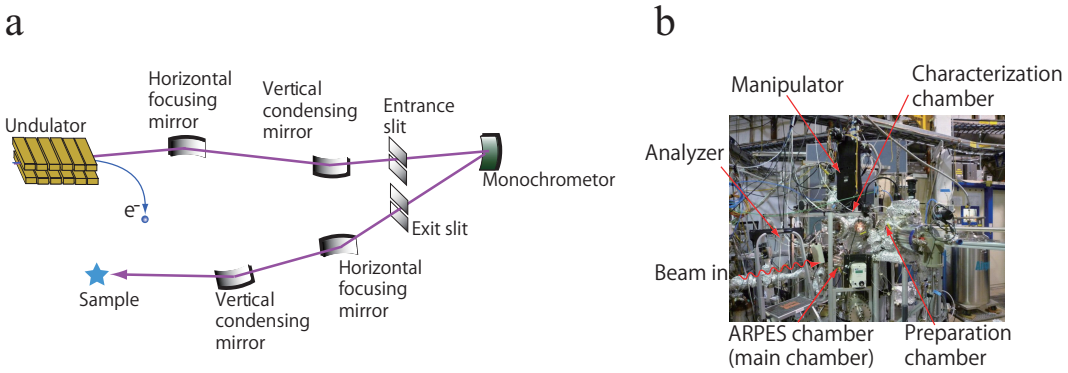

Figure 2.7: ARPES measurement system at Stanford Synchrotron Radiation Lightsource beamline 5-4. (a) Schematic layout of beamline 5-4. (b) Overview of measurement chambers.

Next we describe beamline 5-4 of Stanford Synchrotron Radiation Lightsource (SSRL). Beamline 5-4 is an undulator beamline with a normal incidence monochrometor (NIM) for vacuum ultraviolet (VUV) photons ($\sim$ 7-32 eV). The endstation of the beamline is composed of a load lock chamber, a preparation chamber, a characterization chamber, and a main chamber. Samples are cleaved at the characterization chamber, where a LEED system is installed. A hemispherical analyzer Scienta R4000 is installed in the main chamber. Since the analyzer slit is fixed vertically, Fermi surface mapping is performed by rotating the DPRF (θ) angle.

2.6 Time-resolved photoemission spectroscopy

In order to study the dynamics of the electronic state in solids by photoemission, pump-probe time-resolved ARPES (TrARPES) technique based on pulsed laser photon source has been developed in recent years. Fig. 2.8 shows a schematic illustration of the principles of TrARPES. The pulsed photons from laser source are divided into pump and probe beams. As in other pump-probe techniques, the pump beam brings the system out of equilibrium and the probe beam excite transient valence electrons to the vacuum level. In order to generate probe beams that have sufficient energy to excite valence electrons above the work functions of solids ($\sim$ 4 eV), higher harmonics (HHs) generated from fundamental beams via nonlinear crystals are employed. The fundamental beam of typically 1.5 eV is frequency-doubled twice generating probe beam with 6 eV. In order to change the decay time after the excitation, a delay stage is introduced in the optical path of pump or probe

beams. As a technical difficulty generally encountered in laser-based ARPES, the space-charge effect, the Coulomb repulsion between photoelectrons in the vacuum, becomes striking because the pulsed laser instantaneously excites many photoelectrons and it can severely deteriorate the momentum and energy resolution. In addition, multiphoton absorption in strong fields prevents the application of Fermi's golden rule and distorts the spectra. Further, the high-power laser beam could generate thermal heating of samples. To avoid these effects, the power of pump and probe beams must be reduced. Therefore, to obtain good statistics, high-repetition laser source is employed.

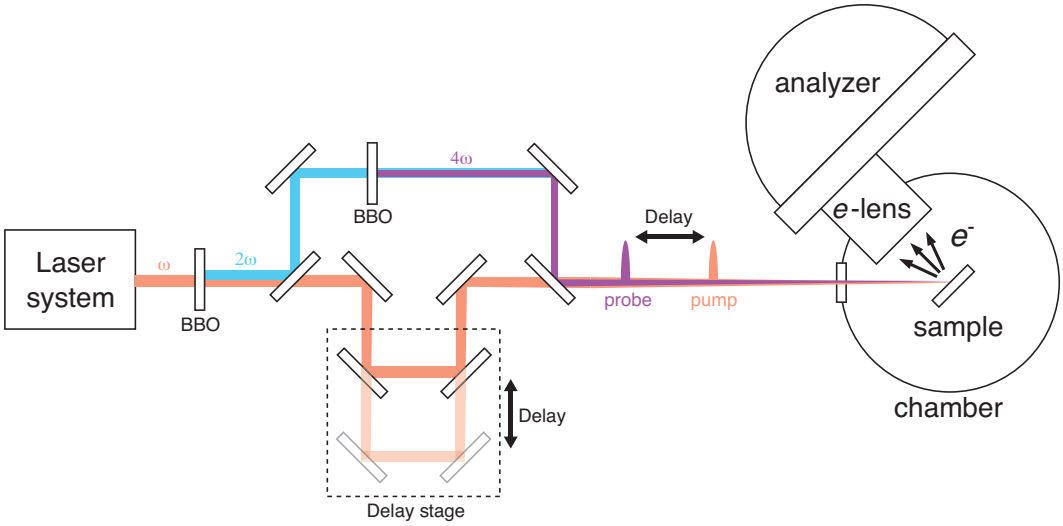

Figure 2.8: Typical setup of time-resolved ARPES (TrARPES).

2.7 TrARPES system using vacuum-ultraviolet higher harmonic generation

I explain a newly-constructed TrARPES system at Institute of Solid State Physics (ISSP) using vacuum-ultraviolet laser. Figure 2.9 shows the optical layout of the TrARPES system. The fundamental laser ($\lambda = 790$ nm) is created from a Ti:Sapphire laser system with the repetition rate of 1 kHz and the pulse width of 90 fs. The incident beam is split to pump and probe beams. In the pump line, a delay stage is introduced to change the optical distance of the pump line, which modifies the delay time between the pump and probe pulses. For probe beams, conventional TrARPES system typically utilizes the 4th order higher-harmonic generation (HHG) from nonlinear crystals like β-BaB_2O_4 (BBO); however, the photon energy available is usually below ~ 7 eV, which significantly limits the accessible momentum space. To overcome this hurdle, we employed the higher harmonics generated by irradiating

laser pulses to rare gas (Ne, Ar, Xe) jet. This process creates HHG with the photon energy equal to odd number times that of the incident beam. In the present setup, we focus the fundamental beam or second harmonics created through BBO crystal to rare gas jet created in the HHG chamber. In the spectrometer chamber, the HHG is separated by a grating and the spectra can be checked by a multi channel plate. The spectrum image in the middle of the figure crearly indicates that HHG up to $\sim$ 70 eV is successfully created. In order to select energy for photoemission experiments, the beams are reflected twice by Mo/Si multilayer mirrors, which are specially designed to reflect photons within a narrow energy range. In the present setup, the mirrors are placed on the four faces of rotatable rectangular parallelepiped mirror holders, and the experimenters can select four different $h\nu$. Also, in order to cut the fundamental laser light which remains coaxial to the HHG, we employ a ultrathin Al filter after the mirror chamber, which stops the incident beams as well as blocks the inflow of the rare gas to the measurement chamber, where ultrahigh vacuum is required. The pump and probe beams are focused to the sample, and the energy and emission angles of the photoelectrons are measured by a Scienta R4000 hemispherical electron energy analyzer.

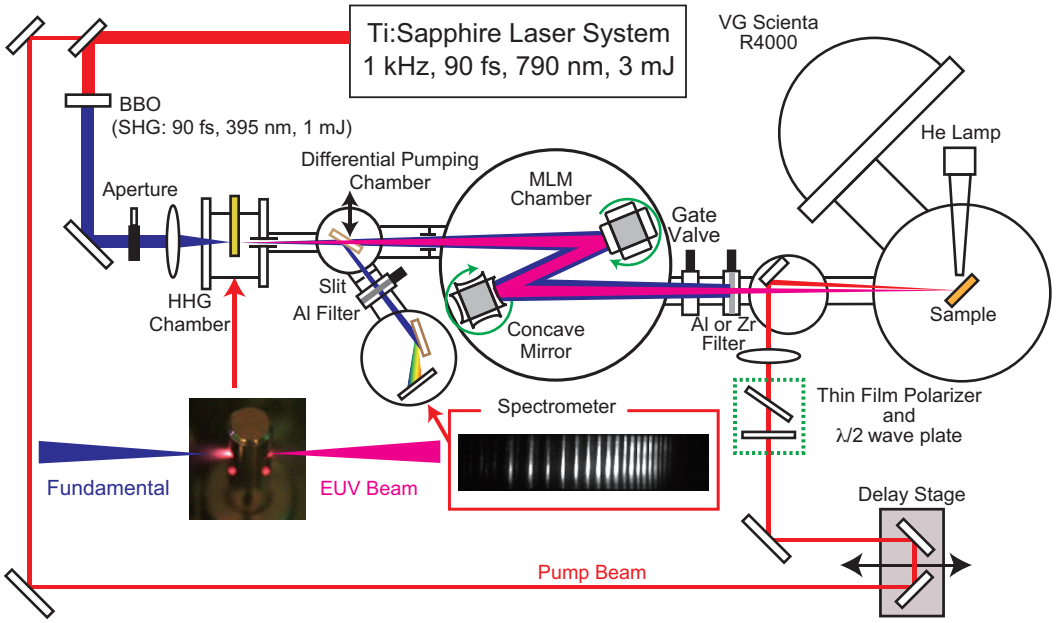

Figure 2.9: Schematic optical layout of a time-resolved ARPES system equipped with vacuum-ultraviolet laser at Institute for Solid State Physics (ISSP).

Figure 2.10 shows an overview of the TrARPES system. During my Ph.D. study, I have been involved in the construction of this apparatus, in particular of the multilayer mirror chamber, HHG chamber, delay stage and pump line, in addition to vacuum pumping system related to those chambers. Here I summarize technical difficulties which I have tackled. The first difficulty lies in the generation of HHs.

For the stable and efficient production of HHs, the pressure of rare gas jet should be increased, while it must be immediately pumped out of chamber to protect the system. For this purpose, we have prepared a metallic tube with a pair of small holes (see left bottom of Fig. 2.9) through which the fundamental laser is impinged to generate HHs. The rare gas is pumped out by a large turbo molecular pump with diameter of $\sim$ 70 cm attached below the chamber. During operation, the pressure of the HHG chamber is kept at $\sim 10^{-3}$ Torr to obtain sufficient count rate. The second difficulty is the overlapping of pump and probe beams at the focusing point of the hemispherical analyzer. To achieve this, before the measurement, we first optimize the sample position by maximizing the photoemission count rate from the He discharge lamp, then confirm the overlapping of visible pump beam and fundamental laser at the sample spot by monitoring the CCD image from behind the analyzer or by employing a pin hole attached to the tip of the sample manipulator [93].

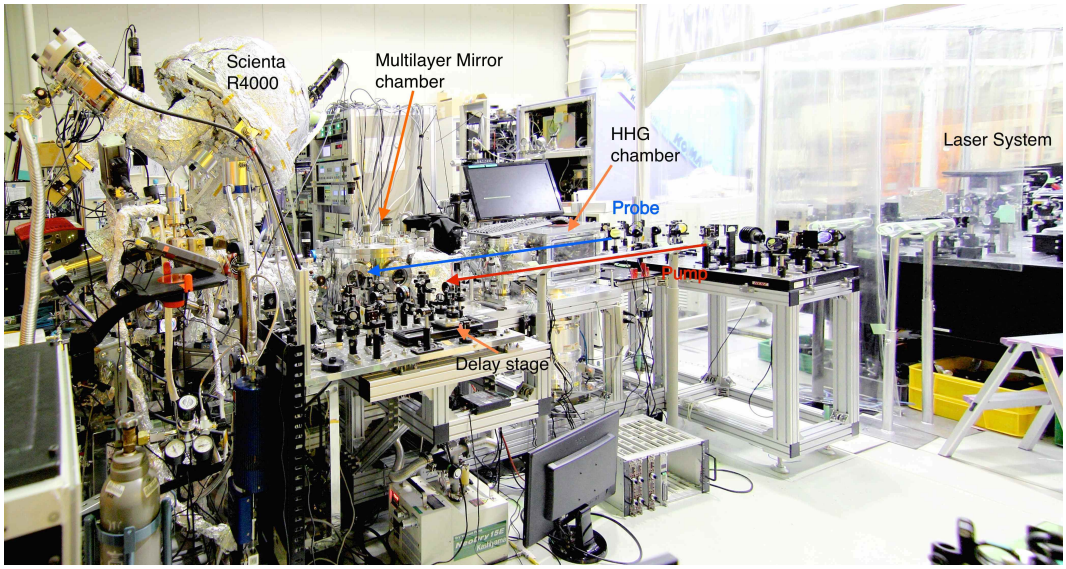

Figure 2.10: Overview of the new time-resolved ARPES system at ISSP.

2.8 Resonant inelastic x-ray scattering

Inelastic scattering experiments provide direct information about various elementary excitations in solids. The most extensively used technique is neutron scattering. Due to its high energy resolution, it has uncovered elementary excitations in the cuprates [94]. However, neutron scattering has several technological limitations. First, it is difficult to detect high energy excitations because of the limited energy transfer from neutrons to the system. Second, due to the low cross section of the neutron beam with the system, it is inevitable to prepare large amount of single

crystals, which makes it impossible to measure systems whose single crystals are difficult to grow, and thin film samples.

The newly developing photon scattering technique we employed in the present work is resonant inelastic x-ray scattering (RIXS) [95, 96]. Since it is an inelastic photon scattering in the x-ray regime, it is also sometimes called x-ray Raman scattering. Figure 2.11 (a) shows a schematic diagram of RIXS process [96]. First, electrons in the core level are excited to the unoccupied states by absorbing the incoming photons. Second, the core holes are filled by valence electrons with the emission of outgoing photons. In total, this process creates an excitation with momentum $\hbar\boldsymbol{k} - \hbar\boldsymbol{k}'$ and energy $\hbar\omega_{\boldsymbol{k}} - \hbar\omega_{\boldsymbol{k}'}$. By measuring the direction and energy of the scattered light, we can investigate into the dispersion of the elementary excitations in solids. RIXS has several advantages. First, since RIXS utilizes the x-ray absorption edges, the cross sections of x-rays and electron is resonantly enhanced and much larger than the cross section of neutron scattering. Therefore RIXS can be applied to small single crystals and thin film samples. It also leads to the chemical selectivity of the scattering process, which is useful when more than one chemical elements coexist in the system. Second, since the energy difference between incoming and outgoing photons is transferred to the system, the transfer energy can be larger than neutron scattering. Thus high energy excitations including charge-transfer excitations, d-d excitations, in addition to magnons and phonons, are within the scope of RIXS. Figure 2.11 (b) shows the time development of the energy resolution of RIXS at the Cu L_3 edge. Before 2000, the energy resolution was larger than 1 eV; recent technological advances in the third-generation synchrotron light sources with improved brilliance and low emittance, improved CCD photon detectors have improved the resolution down to $\sim$ 100 meV in 2008. For these reasons, RIXS can be considered as the complimentary technique to neutron scattering. In the following we describe the principles and recent technological advances in RIXS.

2.8.1 Dynamical structure factor

2.8.2 Fluctuation-dissipation theorem

Suppose the the system investigated is described by Hamiltonian H and the external force $F(t)$ is applied to the system as a perturbation. We write the hamiltonian of the perturbation as

$$H_{\text{ext}} = -\hat{A}F(t), \tag{2.96}$$

where A is the operator of the physical quantity conjugate to the external force $F(t)$. Under the external force, the equation of motion of the density matrix is

$$i\hbar\frac{\partial}{\partial t}\rho(t) = [H + H_{\text{ext}}, \rho(t)]. \tag{2.97}$$

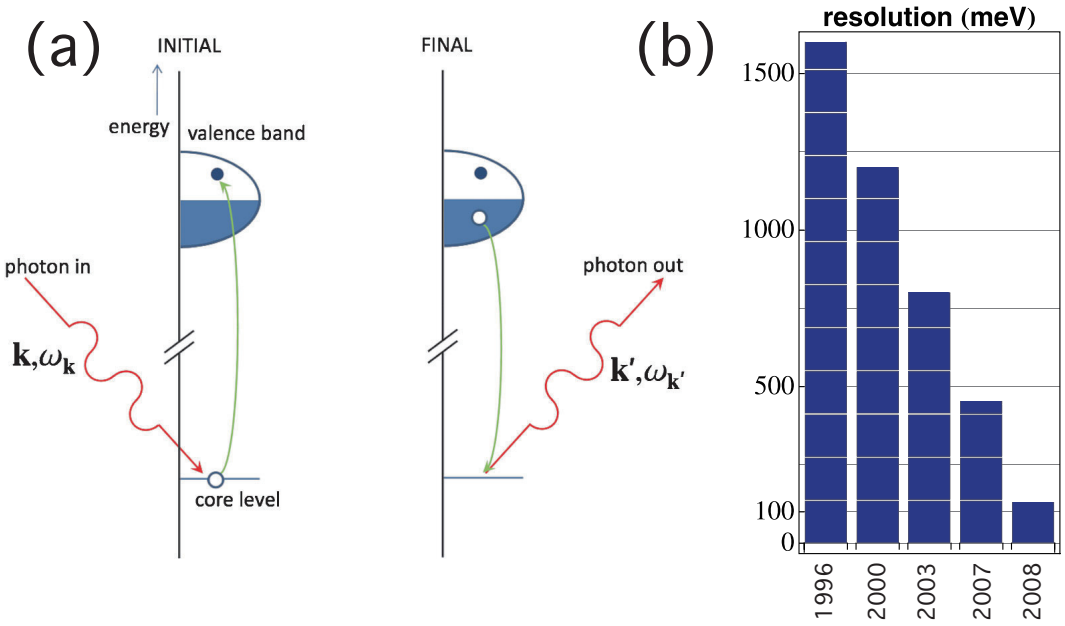

Figure 2.11: (a) Schematics of direct resonant inelastic x-ray scattering (RIXS). (b) Development of soft x-ray RIXS resolution at the Cu L_3 edge [96].

The expectation value of a physical quantity $\hat{B}$ at time t is, to the linear order of the perturbation,

$$\begin{aligned}\overline{B(t)} &= \mathrm{Tr}(\rho(t)B) \\ &= \langle B\rangle + \frac{1}{i\hbar}\int_{-\infty}^{t} dt' \langle [A, B(t-t')]\rangle F(t'),\end{aligned} \tag{2.98}$$

where $\langle B\rangle = \mathrm{Tr}(B)$ is the expectation value of $\hat{B}$ in the equilibrium ($t = \infty$) state and $B(t) = e^{iHt/\hbar}Be^{-iHt/\hbar}$ is the Heisenberg representation. Defining the generalized susceptibility in the following form,

$$\Delta B(t) = \overline{B(t)} - \langle B\rangle = \mathrm{Re}[\chi_{BA}(\omega)F_0 e^{-i\omega t}] \tag{2.99}$$

we can derive

$$\chi_{BA}(\omega) = \frac{i}{\hbar}\int_0^{\infty} dt \langle [B(t), A]\rangle e^{i\omega t}, \tag{2.100}$$

which is the well-known Kubo formula. If we define advanced ($-$) and retarded Green's functions ($+$)

$$G^{\pm}_{BA}(t) = \pm\frac{i}{\hbar}\theta(t)\langle [B(t), A]\rangle, \tag{2.101}$$

the generalized susceptibility is the Fourier transform of the retarded Green's function:

$$\chi_{BA}(\omega) = -G^{+}_{BA}(\omega). \tag{2.102}$$

The dynamical structure factor is defined as

$$S_{BA}(\omega) = \int_{-\infty}^{\infty} \frac{dt}{2\pi} \langle B(t)A \rangle e^{i\omega t}. \tag{2.103}$$

It is related to the Green's functions in the following way:

$$S_{BA}(\omega) = \frac{1}{2\pi} \frac{i}{1 - e^{-\beta\hbar\omega}} [G^{+}_{BA}(\omega) - G^{-}_{BA}(\omega)]. \tag{2.104}$$

In the case $B = A^{\dagger}$, it can also be rewritten as

$$S_{BA}(\omega) = \frac{1}{\pi} \frac{1}{1 - e^{-\beta\hbar\omega}} \mathrm{Im}\chi_{BA}(\omega). \tag{2.105}$$

2.8.3 X-ray scattering cross sections

To compute the cross sections of x-ray scattering process, we start with the Hamiltonian for electrons in a quantized electromagnetic field

$$\begin{aligned} H = & \sum_i \frac{1}{2m} \left(\boldsymbol{P}_j - \frac{e}{c} \boldsymbol{A}(\boldsymbol{r}_j) \right)^2 + \sum_{ij} V(\boldsymbol{r}_{ij}) \\ & - \frac{e\hbar}{2mc} \sum_j \boldsymbol{s}_j \cdot \nabla \times \boldsymbol{A}(\boldsymbol{r}_j) - \frac{e\hbar}{2(mc)^2} \sum_j \boldsymbol{s}_j \cdot \boldsymbol{E}(\boldsymbol{r}_j) \times \left(\boldsymbol{P}_j - \frac{e}{c} \boldsymbol{A}(\boldsymbol{r}_j) \right) \\ & + \sum_{\boldsymbol{k}\lambda} \hbar\omega_{\boldsymbol{k}} \left(c^{\dagger}_{\boldsymbol{k}\lambda} c_{\boldsymbol{k}\lambda} + \frac{1}{2} \right), \end{aligned} \tag{2.106}$$

where the vector potential $\boldsymbol{A}(\boldsymbol{r})$ is expanded by creation and annihilation operators $c^{\dagger}_{\boldsymbol{k}\lambda}$ and $c_{\boldsymbol{k}\lambda}$ as

$$\boldsymbol{A}(\boldsymbol{r}) = \sum_{\boldsymbol{k}\lambda} \left(\frac{2\pi\hbar c^2}{V\omega_{\boldsymbol{k}}} \right)^{1/2} (\boldsymbol{\epsilon}_{\boldsymbol{k}\lambda} c_{\boldsymbol{k}\lambda} e^{i\boldsymbol{k}\cdot\boldsymbol{r}} + \boldsymbol{\epsilon}^{*}_{\boldsymbol{k}\lambda} c^{\dagger}_{\boldsymbol{k}\lambda} e^{-i\boldsymbol{k}\cdot\boldsymbol{r}}), \tag{2.107}$$

where λ denotes two polarizations. The application of the Coulomb gauge leads to the transversality of the waves:

$$\boldsymbol{k} \cdot \boldsymbol{\epsilon}_{\boldsymbol{k}\lambda} = 0. \tag{2.108}$$

The vector potential is linear in c and $c^{\dagger}$ so that the x-ray scattering event occurs in second order for terms linear in $\boldsymbol{A}$ and in first order for quadratic terms. Since the fourth spin-orbit term is already of order $(v/c)^2$, we will omit linear terms in $\boldsymbol{A}$ and

keep only quadric terms and those independent of $\boldsymbol{A}$. Substituting $\boldsymbol{E} = -\nabla\phi + \dot{\boldsymbol{A}}$, the fourth term becomes

$$-\frac{e\hbar}{2(mc)^2}\left(\sum_j \boldsymbol{s}_j \cdot (-\nabla\phi_j \times \boldsymbol{P}_j) + \sum_j \boldsymbol{s}_j \frac{e}{c^2} \cdot [\dot{\boldsymbol{A}}(\boldsymbol{r}_j) \times \boldsymbol{A}(\boldsymbol{r}_j)]\right). \tag{2.109}$$

We now write

$$H = H_0 + H_R + H' \tag{2.110}$$

with

$$H_0 = \sum_j \frac{1}{2m}\boldsymbol{P}_j^2 + \sum_{ij} V(\boldsymbol{r}_{ij}) + \frac{e\hbar}{2(mc)^2}\sum_j \boldsymbol{s}_j \cdot (\nabla\phi_j \times \boldsymbol{P}_j) \tag{2.111}$$

$$H_R = \sum_{\boldsymbol{k}\lambda} \hbar\omega_{\boldsymbol{k}} \left(c^\dagger_{\boldsymbol{k}\lambda} c_{\boldsymbol{k}\lambda} + 1/2\right) \tag{2.112}$$

$$\begin{aligned} H' = {} & \frac{e^2}{2mc^2}\sum_j \boldsymbol{A}^2(\boldsymbol{r}_j) - \frac{e}{mc}\sum_j \boldsymbol{A}(\boldsymbol{r}_j)\cdot\boldsymbol{P}_j - \frac{e\hbar}{mc}\sum_j \boldsymbol{s}_j \cdot [\nabla \times \boldsymbol{A}(\boldsymbol{r}_j)] \\ & - \frac{e\hbar}{2(mc)^2}\frac{e}{c^2}\sum_j \boldsymbol{s}_j \cdot [\dot{\boldsymbol{A}}(\boldsymbol{r}_j) \times \boldsymbol{A}(\boldsymbol{r}_j)] \end{aligned} \tag{2.113}$$

$$\equiv H'_1 + H'_2 + H'_3 + H'_4. \tag{2.114}$$

Among the perturbation terms, H'_1 and H'_4 are quadratic in $\boldsymbol{A}$, whereas H'_2 and H'_3 are linear. The x-ray cross sections are calculated as the transition probability from the initial state $|a\rangle$, an eigenstate of H_0 with energy eigenvalue E_a, with an incoming photon $\boldsymbol{k}\lambda$, to the final state $|b\rangle$ with a scattered photon $\boldsymbol{k}'\lambda'$. To the second order, the transition probabity per unit time is given by the Fermi's golden rule

$$w = \frac{2\pi}{\hbar}\left|\langle f|\, H\, |i\rangle + \sum_n \frac{\langle f|\, H'\, |n\rangle\, \langle n|\, H'\, |i\rangle}{E_i - E_n}\right|^2 \delta(E_i - E_f), \tag{2.115}$$

$$|i\rangle = |a;\boldsymbol{k}\lambda\rangle\,, |f\rangle = |b;\boldsymbol{k}'\lambda'\rangle\,, E_i = E_a + \hbar\omega_{\boldsymbol{k}}, E_f = E_b + \hbar\omega_{\boldsymbol{k}'}. \tag{2.116}$$

Since both the initial and final states contain one photon, H'_1 and H'_4 contribute to the first order term and H'_2 and H'_3 to the second order term. When only the low-lying excitations are investigated, $\omega_{\boldsymbol{k}} \sim \omega'_{\boldsymbol{k}}$, the first order term becomes

$$\begin{aligned} &\langle b;\boldsymbol{k}'\lambda'|H'_1 + H'_4\,|a;\boldsymbol{k}\lambda\rangle = \\ &\qquad \frac{2\pi\hbar c^2}{V\omega}\frac{e^2}{mc^2}\left(\langle b|\sum_j e^{i\boldsymbol{q}\cdot\boldsymbol{r}_j}\,|a\rangle\,\boldsymbol{\epsilon}'\cdot\boldsymbol{\epsilon} - i\frac{\hbar\omega}{mc^2}\,\langle b|\sum_j e^{i\boldsymbol{q}\cdot\boldsymbol{r}_j}\boldsymbol{s}_j\,|a\rangle\cdot\boldsymbol{\epsilon}'\times\boldsymbol{\epsilon}\right), \end{aligned} \tag{2.117}$$

where $\boldsymbol{\epsilon} = \boldsymbol{\epsilon}_{\boldsymbol{k}\lambda}$, $\boldsymbol{\epsilon}' = \boldsymbol{\epsilon}^*_{\boldsymbol{k}'\lambda'}$ and $\boldsymbol{q} = \boldsymbol{k} - \boldsymbol{k}'$. The contribution from the first term is called Thomson scattering, which depends on the Fourier transform of the electron density $\sum_j e^{i\boldsymbol{q}\cdot\boldsymbol{r}_j}$. The second term is smaller than the first term by the factor $\hbar\omega/mc^2$ ($\sim 2 \times 10^{-3}$ for 1 keV x-rays) and depends on the Fourier transform of the spin density $\sum_j e^{i\boldsymbol{q}\cdot\boldsymbol{s}_j}\boldsymbol{r}_j$. The differential cross section is obtained from the transition probability:

$$\frac{d^2\sigma}{d\Omega' dE'} = w\rho(E_f)/I_0 \tag{2.118}$$

$$\rho(E_f) = \frac{V}{(2\pi)^3}\frac{\omega_{\boldsymbol{k}}^2}{\hbar c^3}, I_0 = \frac{c}{V}. \tag{2.119}$$

Including the second order terms, the final expression becomes

$$\begin{aligned}\frac{d^2\sigma}{d\Omega' dE'} = \left(\frac{e^2}{mc^2}\right)^2 \Bigg| \langle b| \sum_j e^{i\boldsymbol{q}\cdot\boldsymbol{r}_j} |a\rangle \, \boldsymbol{\epsilon}'\cdot\boldsymbol{\epsilon} - i\frac{\hbar\omega}{mc^2}\langle b| \sum_j e^{i\boldsymbol{q}\cdot\boldsymbol{r}_j}\boldsymbol{s}_j |a\rangle \cdot \boldsymbol{\epsilon}'\times\boldsymbol{\epsilon} \\ + \frac{\hbar^2}{m}\sum_c\sum_{ij}\Bigg(\frac{\langle b|\,(\boldsymbol{\epsilon}'\cdot\boldsymbol{P}_i/\hbar - i(\boldsymbol{k}'\times\boldsymbol{\epsilon}'\cdot\boldsymbol{s}_i))e^{-i\boldsymbol{k}'\cdot\boldsymbol{r}_i}|c\rangle\langle c|\,(\boldsymbol{\epsilon}\cdot\boldsymbol{P}_j/\hbar + i(\boldsymbol{k}\times\boldsymbol{\epsilon}\cdot\boldsymbol{s}_j))e^{i\boldsymbol{k}'\cdot\boldsymbol{r}_i}|a\rangle}{E_a - E_c + \hbar\omega_{\boldsymbol{k}} - i\Gamma_c/2} \\ + \frac{\langle b|\,(\boldsymbol{\epsilon}\cdot\boldsymbol{P}_j/\hbar - i(\boldsymbol{k}\times\boldsymbol{\epsilon}\cdot\boldsymbol{s}_i))e^{+i\boldsymbol{k}\cdot\boldsymbol{r}_i}|c\rangle\langle c|\,(\boldsymbol{\epsilon}'\cdot\boldsymbol{P}_j/\hbar - i(\boldsymbol{k}'\times\boldsymbol{\epsilon}'\cdot\boldsymbol{s}_j))e^{-i\boldsymbol{k}'\cdot\boldsymbol{r}_i}|a\rangle}{E_a - E_c + \hbar\omega_{\boldsymbol{k}'}}\Bigg)\Bigg|^2 \\ \times \delta(E_a - E_b + \hbar\omega_{\boldsymbol{k}} - \hbar\omega_{\boldsymbol{k}'}).\end{aligned} \tag{2.120}$$

In the non-resonant x-ray scattering, the second order term gives much smaller contribution than the first-order terms. When we ignore the spin-dependent term, the differential cross section can be rewritten as

$$\begin{aligned}\frac{d^2\sigma}{d\Omega' dE'} &= \left(\frac{e^2}{mc^2}\right)^2 (\boldsymbol{\epsilon}'\cdot\boldsymbol{\epsilon})^2 \left|\langle b| \sum_i e^{i\boldsymbol{q}\cdot\boldsymbol{r}_i}|a\rangle\right|^2 \delta(E_a - E_b + \hbar\omega_{\boldsymbol{k}} - \hbar\omega_{\boldsymbol{k}'}) \\ &= \left(\frac{e^2}{mc^2}\right)^2 (\boldsymbol{\epsilon}'\cdot\boldsymbol{\epsilon})^2 \left|\langle b|\,\rho^\dagger_{\boldsymbol{q}}\,|a\rangle\right|^2 \delta(E_a - E_b + \hbar\omega),\end{aligned} \tag{2.121}$$

where $\rho^\dagger_{\boldsymbol{q}} = \int d\boldsymbol{r} e^{i\boldsymbol{q}\cdot\boldsymbol{r}}\rho(\boldsymbol{r}) = \sum_i e^{i\boldsymbol{q}\cdot\boldsymbol{r}_i}$ is the Fourier transform of the density operator and $\hbar\omega = \hbar\omega_{\boldsymbol{k}} - \hbar\omega_{\boldsymbol{k}'}$ is the energy transfer. In the actual experiment, the initial state is the thermal average of all possible states, and the final electronic state is not analyzed so that the transitions to the all possible electronic final states have to be summed. Therefore the total transition probability $R(\boldsymbol{q},\omega)$ with momentum

transfer $\boldsymbol{q}$ and energy transfer $\hbar\omega$ is

$$\begin{aligned} R(\boldsymbol{q},\omega) &= \left(\frac{e^2}{mc^2}\right)^2 (\boldsymbol{\epsilon}'\cdot\boldsymbol{\epsilon})^2 \sum_a e^{\beta(\Omega-E_a)} \sum_b \langle a|\,\rho_{\boldsymbol{q}}\,|b\rangle\,\langle b|\,\rho_{\boldsymbol{q}}^\dagger\,|a\rangle \int_{-\infty}^{\infty}\frac{dt}{2\pi}e^{i(E_a-E_b+\omega)t} \\ &= \left(\frac{e^2}{mc^2}\right)^2 (\boldsymbol{\epsilon}'\cdot\boldsymbol{\epsilon})^2 \int_{-\infty}^{\infty}\frac{dt}{2\pi}e^{i\omega t} \sum_a e^{\beta(\Omega-E_a)} \sum_b \langle a|\,e^{iHt}\rho_{\boldsymbol{q}}e^{-iHt}\,|b\rangle\,\langle b|\,\rho_{\boldsymbol{q}}^\dagger\,|a\rangle \\ &= \left(\frac{e^2}{mc^2}\right)^2 (\boldsymbol{\epsilon}'\cdot\boldsymbol{\epsilon})^2 \int_{-\infty}^{\infty}\frac{dt}{2\pi}e^{i\omega t}\langle\rho_{\boldsymbol{q}}(t)\rho_{\boldsymbol{q}}^\dagger\rangle \\ &= \left(\frac{e^2}{mc^2}\right)^2 (\boldsymbol{\epsilon}'\cdot\boldsymbol{\epsilon})^2 S(\boldsymbol{q},\omega), \end{aligned} \tag{2.122}$$

where $\Omega = \mathrm{Tr}(e^{-\beta H})$ is the grand potential, $\langle\cdot\rangle$ represents thermal average, and $S(\boldsymbol{q},\omega)$ is the charge dynamical structure factor.

2.9 RIXS system at National Synchrotron Radiation Research Center

We describe a newly-developed RIXS beamline BL05A1 at National Synchrotron Radiation Research Center (NSRRC), based on active-grating monochromator (AGM) and active-grating spectrometer (AGS) principle [97]. Figure 2.12 (a) shows the schematic illustration of this principle. The key aspect of the layout is that the two gratings and the optical paths are symmetrically designed with respect to the sample. First, a point-like photon source is created by an entrance slit. Photons within a energy window of $\Delta E \sim 500$ meV, via AGM monochrometer, disperse to different positions of the sample. Supposing that that the incident photons are elastically scattered by the system, the outgoing light takes the symmetric path with respect to the sample. Since the light source is point-like by the entrance slit, all the elastically scattered photons focus to the same positions in the CCD. Thus photons counted at different positions on the CCD correspond to inelastically scattered ones. In this manner, the RIXS scattering event within the bandwidth of the incident beam can be collected simultaneously. Assuming that the scattering event is not strongly dependent on the incident energy, this is so efficient photon counting scheme that high signal-to-ratio data within a reasonable experimental time can be expected. Figure 2.12 (b) shows the optical layout of the beamline. The distance from the sample to the gratings is 2.5 m, and that between the AGS grating and the CCD is 3.5 m. In the present status, the polarization of the scattered light is not analyzed.

In order to change the momentum transfer in the RIXS process, one has to change the detector position. In the soft x-ray RIXS, however, this is a formidable task since the entire equipment must be stored in a ultrahigh-vacuum of $\sim 10^{-9}$

Torr, unlike in the hard x-ray RIXS case. Figure 2.13 (a) shows the main chamber of the RIXS system. To change the detector position with respect to the sample, ICF 70 flanges equipped with gate valves are arranged at every 15 degrees' interval, and the detector can be connected either of the flanges. In Fig. 2.13 (b) the overall measurement system is shown. The AGS grating chamber and the CCD detector system are located on a rotation stage (blue foundation), and can be rotated simultaneously.

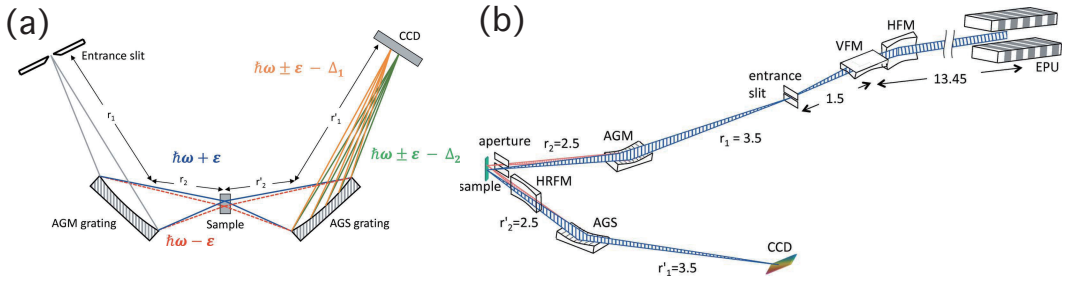

Figure 2.12: (a) AGM-AGS principle employed in the RIXS beamline BL05A1 at NSRRC. (b) Schematic illustration of optical layout in BL05A1 [97]. Distances are indicated in units of meter.

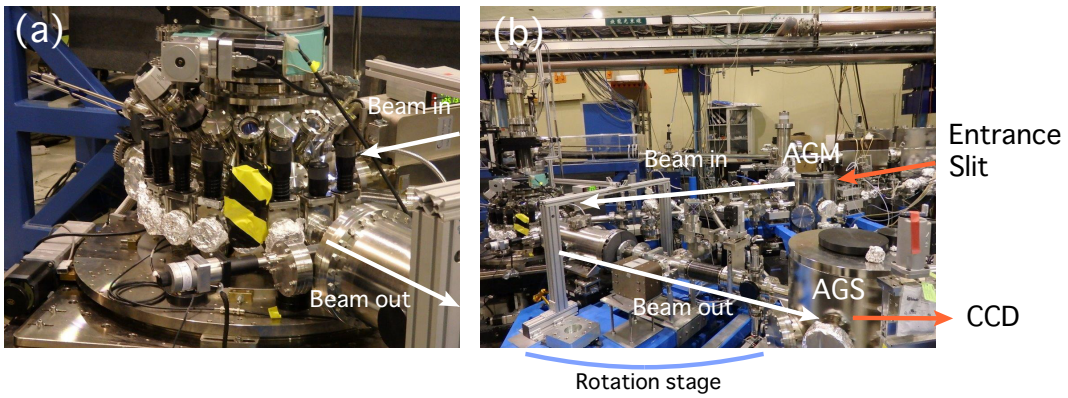

Figure 2.13: (a) Main chamber of the RIXS system. ICF 70 franges equipped with gate valves that connect the main chamber and the detector are arranged at every 15 degrees. (b) Overall picture of the RIXS system. The vacuum chambers including AGS and CCD are placed on top of a rotatable stage.

2.10 WIEN2k package

To gain wider insights to the electronic structure, we have performed first-principles band calculations using WIEN2k package [98] and compared the results with ARPES data. The program package WIEN2k performs electronic structure calculations

of solids within density functional theory. It is based on the full-potential (linearized) augmented plane-wave + local orbitals method, one among the most accurate schemes for band structure calculations.

Chapter 3

Angle-resolved photoemission spectroscopy of $SrFe_2(As_{0.65}P_{0.35})_2$

3.1 Introduction

Since the discovery of high-temperature superconductivity in the iron pnictides and calcogenides [1], the mechanism of Cooper pairing and the symmetry of the order parameter have been the central issues of debate [15, 99]. In the spin-fluctuation-mediated superconductivity, intra-orbital nesting between hole and electron Fermi surfaces (FSs) brings about a sign-changing $s^{\pm}$-wave superconducting (SC) state [8,9,100]. In orbital-fluctuation (OF)-mediated superconductivity, an s^{++}-wave SC state without sign change is realized [17, 19]. For the heavily overdoped systems like $Ba_{1-x}K_xFe_2As_2$, whose hole FSs at the zone center are absent or much smaller than electron FSs, d-wave pairing [101] and time-reversal symmetry-broken $s+id$-wave pairing have been proposed. The diversity of the SC gap structure among various materials and doping elements characterizes the FeSCs in comparison with the cuprates [102].

Among them, the isovalently-substituted $BaFe_2(As_{1-x}P_x)_2$ (Ba122P) system [20] has attracted particular attention since the presence of line nodes in the SC order parameter was proposed from NMR [31], penetration depth and thermal conductivity measurements [27]. Since the existence of line nodes is not imposed by the A_{1g} symmetry of the order parameter but is realized by an accidental crossing of the zero surface of the order parameter and the FSs, a careful experimental investigation is required to determine the location of nodes in the momentum space.

The structure of nodal SC gap is susceptible to the microscopic pairing mechanism. In the spin-fluctuation-mediated pairing, the SC gap tends to change its sign along the nesting vector and the pnictogen height can serve as a switch between nodeless and nodal pairings [11] since the pnictogen height sensitively controls the radii of FSs and consequently the spin susceptibility. For crystal parameters of

Ba122P, Suzuki *et al.* [38] calculated three-dimensional SC gap structure within the RPA. They have shown that the SC gap on the outer hole FS around the Z point with d_{z^2} orbital character is small (below 2 meV) and changes sign, as we have seen in Fig. 1.20 (a). On the other hand, when the orbital-fluctuation exchange is included, Saito *et al.* [39] showed that a nodal s-wave state appears with loop-shaped nodes on electron FSs due to a competition between attractive and repulsive interactions (Fig. 1.20 (b)). Furthermore, in stark contrast with spin-fluctuation scenario, the gap function on the outer hole FS around the Z point becomes comparable or even larger than the other hole FSs, because the interorbital correlations develop in all the d orbitals.

Thus the information about the orbital dependence of the SC gap and location of nodes will clarify the microscopic mechanism. For this purpose, the SC gap of Ba122P has been studied by utilizing various experimental probes. Shimojima *et al.* [35] has found a nearly isotropic, orbital-independent SC gap opening on the three hole FSs around the Z point by high-resolution laser-based angle-resolved photoemission spectroscopy (ARPES). Also, Yamashita *et al.* observed a fourfold oscillation in angle-resolved thermal conductivity as a function of magnetic field direction within the basal plane [34]. Taking into account Shimojima *et al.*'s result, Yamashita *et al.* concluded that loop-like line nodes appear on the outer electron FS [103] to explain their observations.

ARPES measurements utilizing variable energy photons from synchrotrons can directly probe the spectral function at entire momenta in the BZ and are supposed to solve the dispute. However, no consensus on synchrotron-based ARPES data on Ba122P has been achieved so far. Zhang *et al.* [36] reported the observation of a horizontal line node on the outer hole FS around the Z point and claimed the consistency of the data with the Suzuki *et al.*'s calculation. On the other hand, Yoshida *et al.* [37] reported finite and orbital-independent SC gaps on all the hole FSs and an anisotropy of the SC gap on the inner electron FS, and pointed out the importance of orbital fluctuations. To resolve this controversy on Ba122P and the microscopic mechanism, a more systematic study on the nodal versus full gap behaviors is necessary.

A related system $SrFe_2(As_{1-x}P_x)_2$ (Sr122P) has a slightly higher optimal critical temperature (x = 0.35, T_c = 33 K) than that of Ba122P (x = 0.30, T_c = 30 K), and its parent compound $SrFe_2As_2$ has a much higher Néel temperature (T_N) of 197 K than that of $BaFe_2As_2$ (T_N = 138 K) [21]. While Sr122P and Ba122P share nearly the same pnictogen heights from the square Fe lattice, the c-axis length is significantly shorter in Sr122P than in Ba122P reflecting the smaller ionic radius of the Sr^{2+} than Ba^{2+} ions. In a previous work on as-grown samples [26], we measured the band dispersions and FSs of Sr122P. We have clarified that the outer hole FS is more strongly warped along the k_z direction than the corresponding one

in Ba122P, and that the inner hole FS is an ellipsoidal pocket. The presence of line nodes in Sr122P is also suggested from the ^{31}P-NMR [23], specific heat [24], and penetration depth measurements [30]. It is, therefore, conceivable that a similar mechanism gives rise to nodal SC gaps in Ba122P and Sr122P and also to some differences arising from the stronger three-dimensionality and the accidental nature of line nodes in the s-wave SC state. Thus Sr122P is an ideal system for the above purpose of examining the SC gaps in a systematic way and a new insight into the nodal SC gaps in iron pnictides would be obtained. In particular, the change in the gap function on the more enlarged outer hole FS around the Z point with d_{z^2} orbital character, which is sensitive to the microscopic mechanism, may clarify the dominant pairing interaction.

3.2 Experimental

Sr122P single crystals were prepared by the self-flux method described in Ref. 24 and postannealed to achieve the optimal $T_c = 33$ K. The T_c was determined by the onset of Meissner diamagnetic signal with a transition width $\Delta T_c \simeq 5$ K. ARPES experiments were carried out at beamline 5-4 of Stanford Synchrotron Radiation Lightsource (SSRL) and at a laser ARPES apparatus at Institute for Solid State Physics (ISSP). In order to obtain clean surfaces, samples were cleaved *in situ* at pressure better than 1×10^{-10} Torr before measurements. Cleavage occurs along the ab planes. The kinetic energy and momenta of photoelectrons were measured using Scienta R4000 electron energy analyzers. In the following, the x and y axes point from Fe towards the nearest neighbor Fe atoms, the X, Y axes point from Fe towards the second nearest neighbor Fe atoms, and the z axis is parallel to the c-axis. In-plane (k_X,k_Y) and out-of-plane momenta (k_z) are expressed in units of π/a and $2\pi/c$, where $a = 3.90$ Å and $c = 12.09$ Å are the in-plane and out-of-plane lattice constants. Calibration of the Fermi level (E_F) was achieved in reference to the spectra of gold which was in electrical contact with the samples. Incident photons from 21 eV to 35 eV from the synchrotron were linearly polarized. For laser ARPES, the incident photons with $h\nu = 6.998$ eV were linearly s-polarized. The total energy resolution was $\Delta E \sim 6$ meV at $T = 5$ K for synchrotron-radiation ARPES, and $\Delta E \sim 1$ meV at $T = 3$ K for laser ARPES.

3.3 Results and discussion

In-plane FS mappings taken with $h\nu = 24$ eV and 28 eV are shown in Figs. 3.1 (a) and (b), respectively. The first Brillouin zone of Sr122P is also shown in the inset of (a). $h\nu = 24$ eV approximately corresponds to the $k_z = \pi$ plane at the

zone center, and $h\nu = 28$ eV crosses the X [(π, π)] point, judging from the radius of the hole FSs [26] and the elongation of the ϵ FS along the (0,0)-(π, π) line [34]. There are three hole-like bands crossing E_F around the Z point, which form three circular FSs, while two electron-like bands cross E_F around the (π, π) point. These FS topologies are the same as those for as-grown samples [26], demonstrating that the annealing process does not greatly modify the electronic structure. FS mapping along the k_z direction reported in Ref. [26] is reproduced in Fig. 3.1 (c). The orbital character of the hole bands crossing E_F are $d_{xz/yz}$ (β,γ) around the Γ point, and d_{xy} (α), $d_{xz/yz}$ (β), and d_{z^2} (γ) around the Z point. The orbital character for electron bands is $d_{xz/yz}$ (δ) and d_{xy} (ϵ).

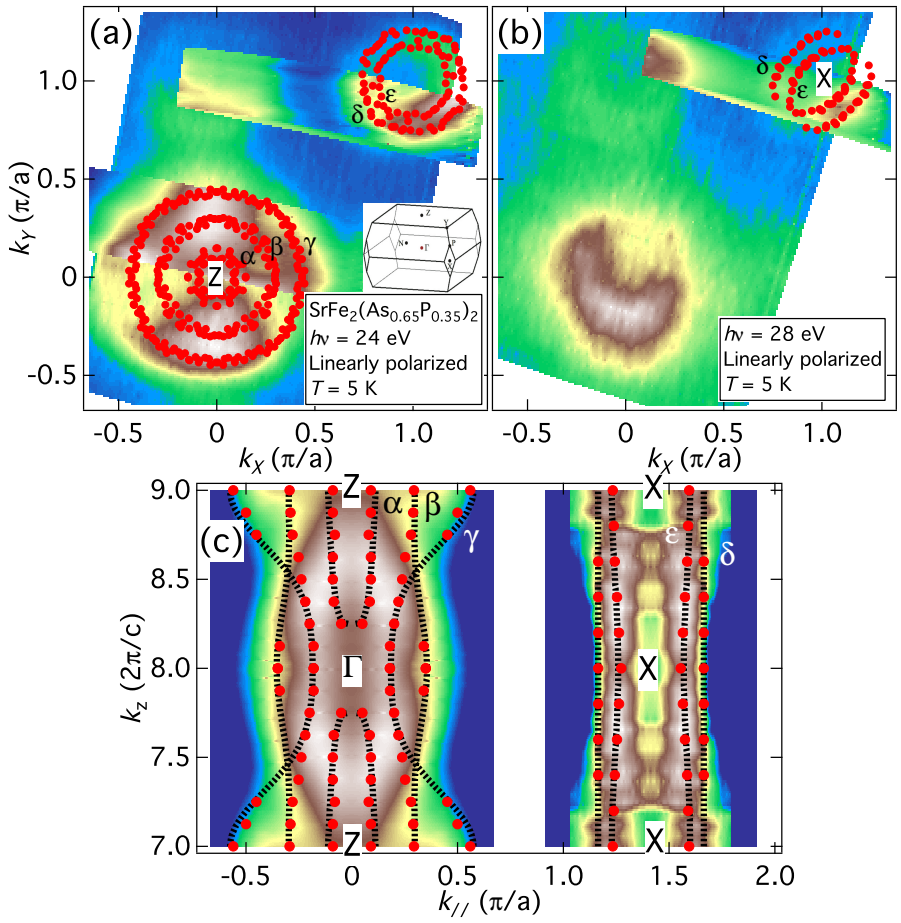

Figure 3.1: (a),(b) In-plane Fermi surface (FS) mapping for $SrFe_2(As_{1-x}P_x)_2$ (Sr122P) ($x = 0.35$) taken with $h\nu = 24$ eV [(a)] and 28 eV [(b)]. Filled circles indicate the k_F positions and their symmetrized points. The first Brillouin zone of Sr122P is shown in the inset of panel (a). (c) FS mapping taken in the k_z-$k_{||}$ plane for Sr122P reproduced from Ref. [26].

Now we investigate the SC gap in the momentum space. Figure 3.2 (a) shows

FS mapping taken with the 7 eV laser. The observation of three FSs and the radius of the outer FS demonstrate that $h\nu = 7$ eV measures a plane close to the Z point. We define the FS angle θ with respect to the nearest Fe-Fe direction as indicated in panel (a). Symmetrized energy distribution curves (EDCs) below and above T_c for the three FSs are shown in Figs. 3.2 (b)-(d). The symmetrization of the spectra with respect to E_F eliminates the effect of the Fermi cutoff and enables us to directly visualize the SC gap opening and their magnitude [104]. The closure of the gaps above T_c demonstrates that the gaps originate from superconductivity. To extract the gap size from the data, symmetrized EDCs below T_c were fitted to the phenomenological low-energy spectral function of the form [105]

$$A(k_F, \omega) = -\frac{1}{\pi} \frac{\Sigma''(k_F, \omega)}{[\omega - \Sigma'(k_F, \omega)]^2 + [\Sigma''(k_F, \omega)]^2}, \tag{3.1}$$

with the self-energy at k_F,

$$\Sigma(k_F, \omega) = -i\Gamma_1 + \Delta^2/[\omega + i\Gamma_0]. \tag{3.2}$$

Here, Γ_1 is the single-particle scattering rate, Δ is the SC gap, and Γ_0 is the inverse pair lifetime. A finite Γ_0 well reproduces the spectral broadening in the pseudogap state of the cuprates [105]. Although the importance of the Γ_0 term has been pointed out [103], here we set $\Gamma_0 = 0$ because the symmetrized EDCs do not show maxima at $\omega = 0$ and the EDCs at 40 K (just above $T_c = 33$ K) in panels (b)-(d) do not show any signature of pseudogap. When the spectra have clear coherence peaks and deep gap at $\omega = 0$ as in the α and β FSs, this fitting procedure works well and the gap size thus deduced yields the coherence peak position [panels (b) and (c)] . However, in the absence of clear SC peaks due to the small gap or low quasiparticle weight as in the case of the γ FS [panel (d)], the fitting is quite unstable and wide parameter sets can reproduce the spectral lineshapes, making it difficult to extract SC gap values. Therefore we estimate the SC gap of the γ FS from the shoulder structures of the low-T spectra if they exist, as indicated by the circles. We notice that the shoulder positions exhibit angular dependence, and the almost absent in -2° and -15° spectra. Note that even when there is no signature of SC gap shoulder, positive Δ with comparable Γ_1 can reproduce spectra like the -15° one in panel (d), as pointed out by Khodas *et al.* [103]. Further, the spectral intensity of the γ band is weaker than other bands. Thus we do not intend to claim the presence of nodes simply because of "no gap" throughout this chapter, as done for Ba122P by Zhang *et al.* [36]. The extracted SC gap is plotted in Fig. 3.2 (e) as a function of θ. The α and β FSs have isotropic gaps of ~ 5 meV and 4 meV, respectively. On the other hand, the γ FS shows a signature of anisotropy with the minimum around $\theta = 0°$ and the maxima around $\theta = 45°$.

In order to further quantify the anisotropy in the γ FS, we show the difference EDCs between below and above T_c in Fig. 3.3 (a). Almost concomitant with the

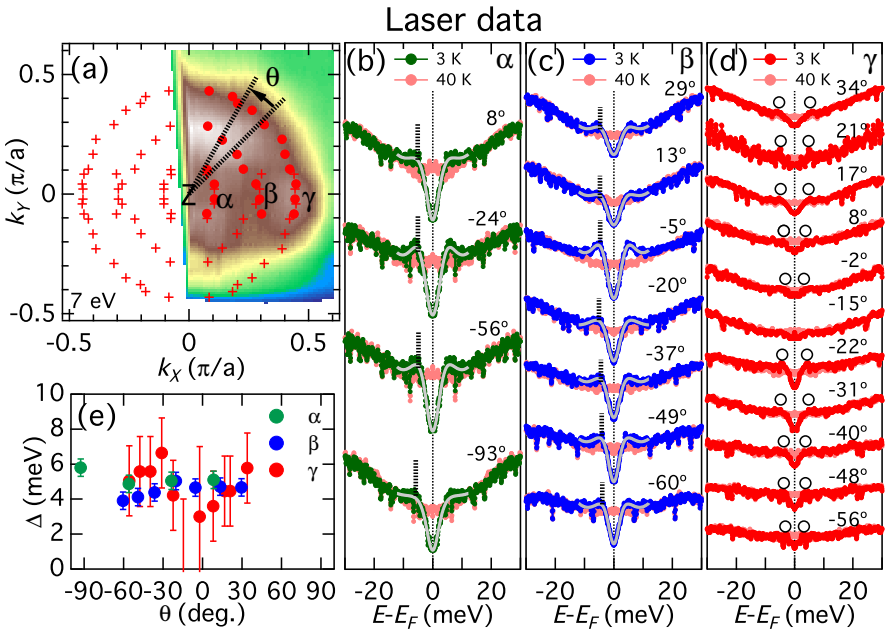

Figure 3.2: (a) FS mapping of the hole FSs taken with $h\nu = 7$ eV laser. Red circles indicate the k_F positions, where the superconducting (SC) gap sizes are estimated, and the crosses show their symmetrized points. FS angle θ is defined with respect to the Fe-Fe direction as indicated in the figure. (b)-(d) Symmetrized energy distribution curves (EDCs) at k_F's for the inner (α), middle (β), and outer (γ) FSs, respectively. Blue and red spectra show the data for 3 K and 40 K, respectively. The gray curves indicate the fitted curves. The vertical bars indicate the estimated SC gaps. For the γ FS, where the SC coherence peaks are almost absent, we determine SC gap from the shoulder structures of the spectra, as indicated by the circles. (e) SC gap Δ plotted as a function of the FS angle θ.

anisotropy of the shoulders, the spectral weight transfer, shown by the blue area in panel (a), also exhibits angular dependence. The spectral weight transfer is plotted in Fig. 3.3 (b) as a function of θ. It also show a signature of anisotropy with a minimum around $\theta = 0°$. Although the spectral weight is not itself a direct measure of SC gap but a quasiparticle weight and/or the superfluid density [106, 107], the anisotropic spectral weight may imply the angular dependence of the orbital character or the anisotropic SC gap.

In order to study wider momentum space, we employed synchrotron ARPES. Figure 3.4 (a) shows symmetrized energy-momentum (E-k) ARPES intensity plots for the hole FSs taken with $h\nu = 23$ eV photons, which again corresponds to the $k_z = \pi$ plane with the Z point at the zone center. The k_F positions are indicated by arrows, and the momentum cuts in the Brillouin zone (BZ) are illustrated in Fig. 3.4 (b). As we have seen in the laser data, the SC coherence peak is the highest for the α sheet, and the smallest for the γ sheet. The symmetrized EDCs are shown in Figs.

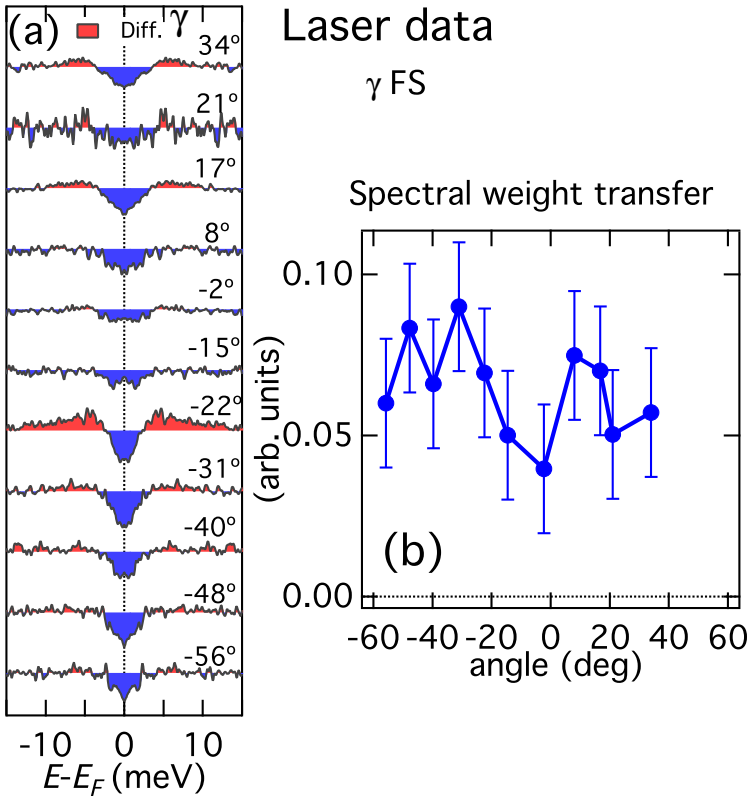

Figure 3.3: (a) Difference symmetrized EDC spectra between 3 K and 40 K for the γ FS. Red (blue) area indicates the increase (decrease) of the spectral weight. (c) Plot of the reduction of spectral weight [blue area in panel (a)] as a function of θ.

3.5 (c)-(e). We observe more pronounced SC coherence peaks for the α FS [panel (c)] than the laser data, probably reflecting better photoemission cross sections at $h\nu = 23$ eV or because 7 eV does not exactly measure the plane around the Z point. For the β FS, the spectral shape is similar to the laser data. For the γ FS, we again observe an indication of anisotropy from the shoulders indicated by the circles. The estimated SC gap is plotted in panel (f). We again obtain isotropic gaps of $\Delta \sim$ 8 meV for the α FS and 6 meV for the β FS. For the γ FS, the amplitude of the anisotropic shoulder is $\sim$ 5 meV around $\theta = \pm 45^\circ$ and 135°, and a signature of gap minima around $\theta = 90^\circ$ (equivalent to $\theta = 0^\circ$), consistent with the laser data. However, we also observe flat symmetrized EDCs between $-14^\circ < \theta < 49^\circ$ [Figs. (e1) and (e2)], probably because the momentum cuts approach the FS edge, which tends to reduce the photoemission intensity and leads to featureless EDCs.

In order to study the k_z dependence of the SC gap, we have performed measurements by varying photon energy. Figure 3.5 shows E-k intensity plots for the hole FSs taken along the k_z direction using $h\nu =$ 23-31 eV photons. At the zone center, $h\nu =$23 eV corresponds to the Z point and $h\nu =$31 eV to the Γ point. We

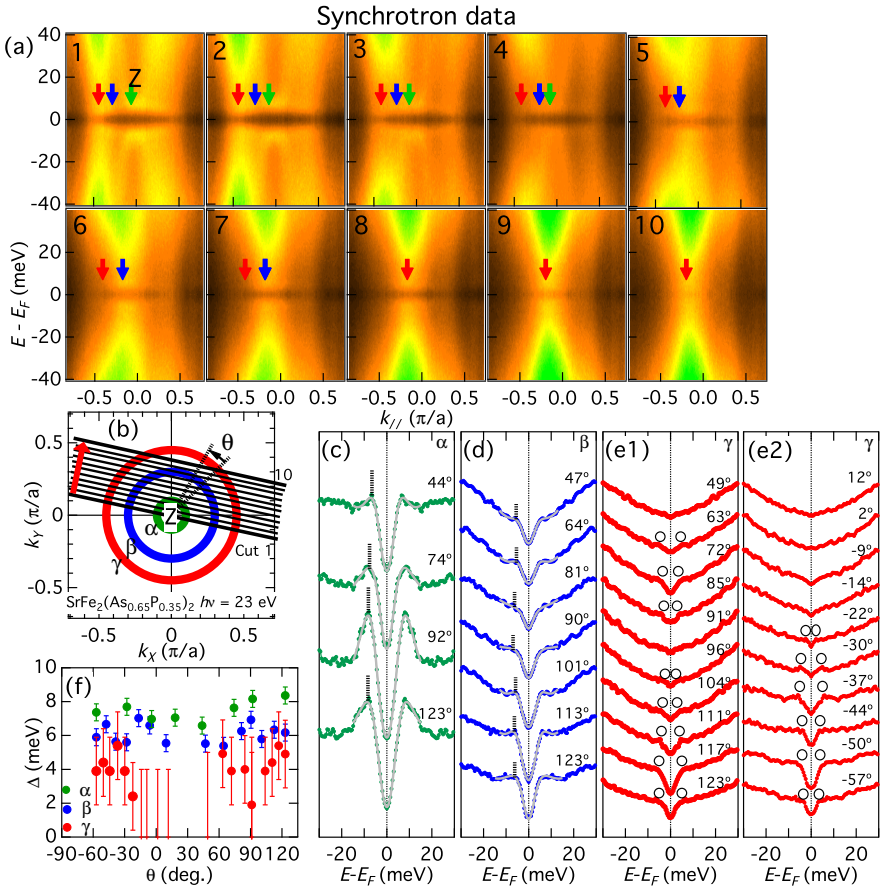

Figure 3.4: (a) Symmetrized energy-momentum (E-k) intensity plots at 5 K for the hole FSs taken with $h\nu = 23$ eV photons. The k_z value corresponds to that of the Z point at the zone center. The location of each cut is indicated in panel (b). The k_F positions are shown by arrows. (b) Schematic figure of the hole FSs. (c)-(e) Symmetrized EDCs. Estimated gap is indicated by dotted lines [(c), (d)] and circles [(e1), (e2)]. (f) SC gap as a function of θ.

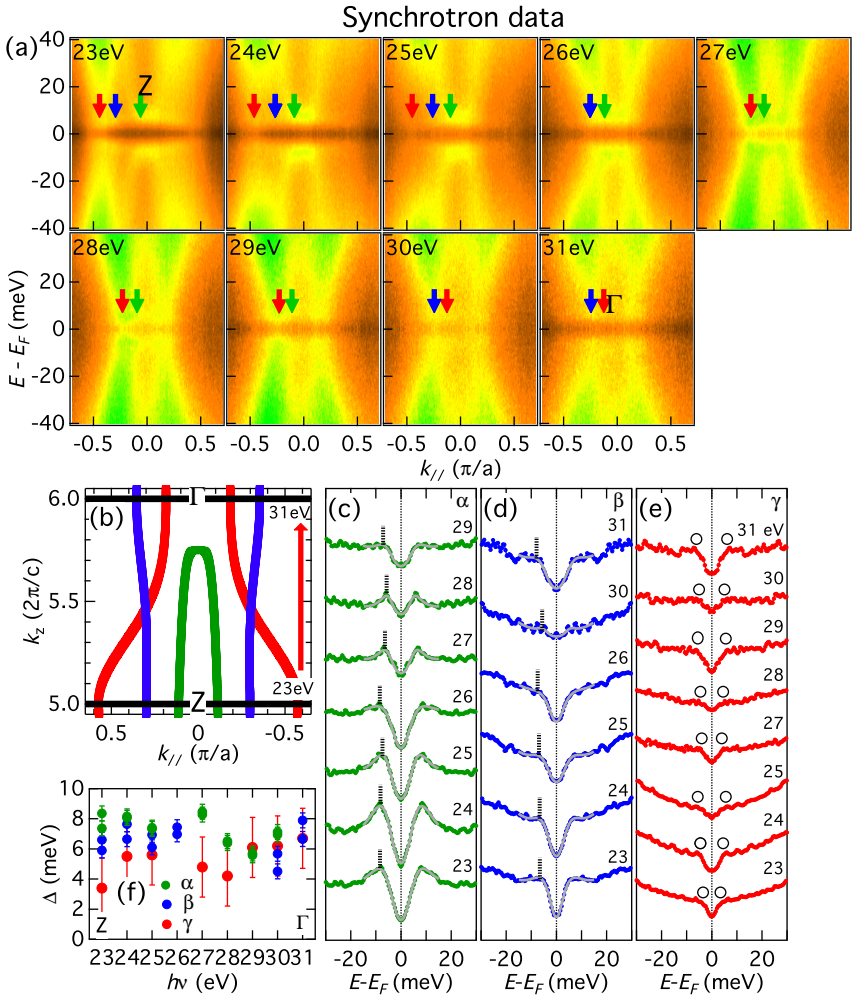

Figure 3.5: (a) Symmetrized E-k intensity plots for the hole FSs taken along the k_z direction using $h\nu$ = 23-31 eV photons. (b) Schematic figure of hole FSs along the k_z direction. (c)-(e) Symmetrized EDCs. (f) SC gap as a function of the incident photon energy.

observe a strong warping of the γ FS as $h\nu$ is varied, as illustrated in Fig. 3.5 (b). Symmetrized EDCs are plotted in Figs. 3.5 (c)-(e) and the estimated gap is plotted in panel (f). As k_z moves from the Z point toward the Γ point, the gap on the α FS becomes smaller and the coherence peak height also becomes lower. The line shape of the β FS is almost unchanged. The gap of the γ FS slightly increases. This behavior can be explained by the modifications of the radii and the orbital component of the FSs. For the α FS, the decrease of the gap and spectral weight is explained by the gradual decrease of the FS radius and accordingly the deterioration of nesting condition between the α and ϵ FSs. For the β FS, since it is almost two-dimensional, the gap size does not show significant k_z dependence. For the γ FS, it has the d_{z^2} character around the Z point and the gap is small since it there is no d_{z^2} orbital component in the electron pockets. As it approaches the Γ point, it acquires the $d_{xz/yz}$ character and the radius of the γ FS becomes comparable to that of the δ FS. As a result, the intraorbital scattering between the γ and δ FSs can be enhanced, leading to the gradual increase of the gap.

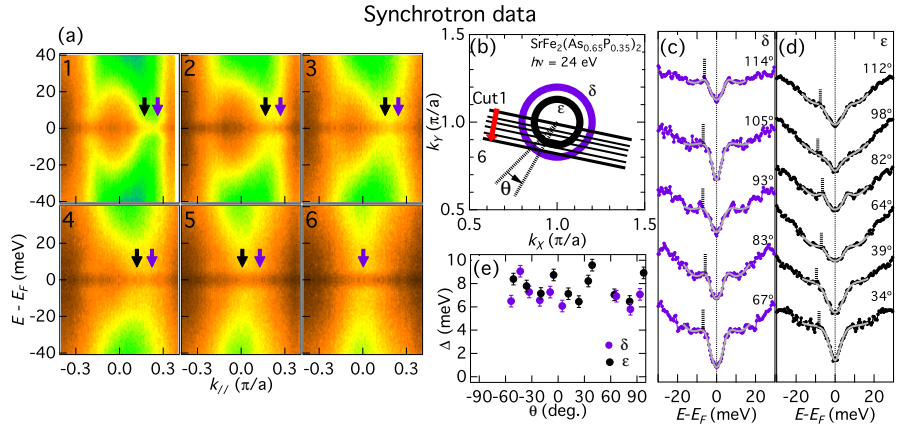

Figure 3.6: (a) Symmetrized E-k intensity plots for the electron FSs taken with $h\nu = 24$ eV photons. (b) Schematic figure of the electron FSs. (c), (d) Symmetrized EDCs. (e) SC gap as a function of θ.

Next we move on to the electron FSs. Figure 3.6 (a) shows symmetrized E-k intensity plots for the electron FSs taken with $h\nu = 24$ eV photons. It can be seen that the SC gap is finite for all k_F's. Judging from the fact that the two electron FSs are almost circular at (π, π) point as illustrated in Fig. 3.6 (b), $h\nu = 24$ eV corresponds to k_z = 5.25 $(2\pi/c)$ plane. The symmetrized EDCs are shown in Figs. 3.6 (c) and (d). We observe SC coherence peaks in the δ sheet. For the ϵ sheet, although the background level is high due to the presence of the δ band below the ϵ band, we still observe gapping at $\omega = 0$. The estimated SC gap is plotted in Fig. 3.6 (e). Both δ and ϵ FSs have isotropic SC gaps of $\Delta \sim 8$ meV. This isotropic gap is in contrast to the observed line nodes [34] and gap anisotropy [37] in the electron

pockets of Ba122P.

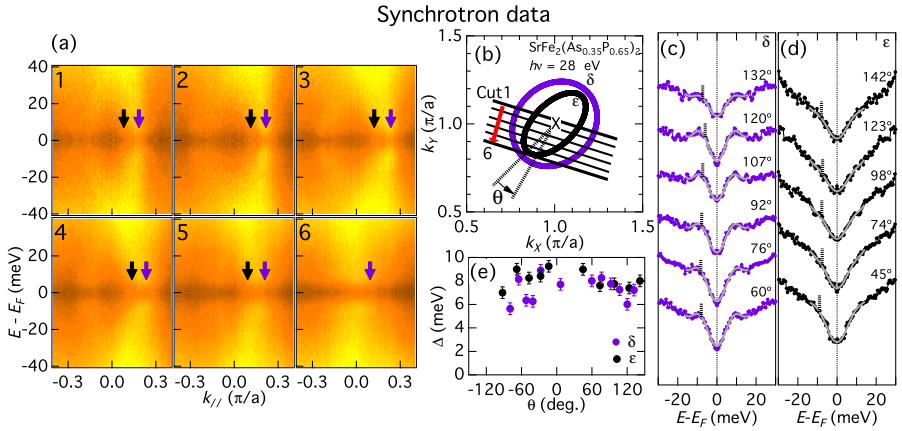

Figure 3.7: (a) Symmetrized E-k intensity plots for the electron FSs taken with $h\nu = 28$ eV photons. (b) Schematic figure of the electron FSs. The k_z at (π, π) for 28 eV corresponds to that of the X point. (c), (d) Symmetrized EDCs. (e) SC gap as a function of θ.

To investigate the k_z dependence of the gap on the electron FSs, we performed in-plane measurements with another $h\nu$ of 28 eV. Fig. 3.7 (a) shows symmetrized E-k intensity plots. $h\nu = 28$ eV corresponds to the $k_z = 5$ $(2\pi/c)$ plane and includes the X point, as illustrated in Fig. 3.7 (b). One again observes that the SC gap is finite for all k_F's. The symmetrized EDCs are shown in Figs. 3.6 (c) and (d). The line shapes are close to those in Fig. 3.6. The SC gap is plotted in Fig. 3.6 (e). Again we obtain almost isotropic gaps of ~ 8 meV both for the δ and ϵ FSs. From these results, it is safe to exclude the possibility of nodes on the electron FSs.

Although it is not possible to exactly determine the three-dimensional nodal structure from the limited momentum cuts in our data, they are most likely around the $\theta = 0^\circ$ line on the γ hole FS around the Z point considering the anisotropic small gap and very low coherence peaks. For the shape of the node, vertical line nodes in the entire k_z seems unlikely, considering the increase of the γ FS gap near the Γ point, as we have seen in Fig. 3.5 (e). From these considerations, we propose that there exists dramatic reduction or a possible sign change on the γ hole FS, around the Z point, and around the $\theta = 0^\circ$ line (the Z-X line).

Here we discuss the relationship of the present result and theoretical calculations. Suzuki *et al.* [38] calculated the gap structure of Ba122P based on spin-fluctuation exchange and showed that sign reversal occurs on the γ FS around the Z point, consistent with the present result. Also, Saito *et al.* calculated it by considering both spin- and orbital-fluctuation exchange. They showed that, without orbital-fluctuation exchange, the γ FS has 4 meV gap on the $k_z = 0$ plane and very small sign-reversed gap around the $k_z = \pi$ plane, indicating the sign reversal near the $k_z = \pi$ plane, reproducing Suzuki *et al.*'s result. Further, the gap on the $k_z = \pi$

plane is the largest for α, intermediate for β, and smallest (and negative) for γ FS, consistent with the present data. On the other hand, when orbital-fluctuation exchange is included, the SC gap on all the hole FS becomes of the same sign, the gap on the electron FSs becomes anisotropic, and nodes may be formed on the electron FSs depending on the microscopic parameters. The latter two predictions are inconsistent with the present data. Also, the gap of the hole FSs on the $k_z = \pi$ plane is the largest for the γ FS, in conflict with the present data. From these observations, the gap structure of Sr122P can qualitatively be explained within by spin-flucutuation exchange mechanism. Quantitatively, however, Suzuki *et al.* showed that the sign-reversed gap on the γ FS has (negative) maximum on the Z-X line, 45° rotated from the present result. Since the calculated gap is small (below 2 meV) around the Z point and the enlarged three-dimensionality of Sr122P, a direct calculation with the parameter sets of Sr122P is necessary.

For the hole FSs, one notices that the spectral weight of SC coherence peak, or equivalently the gap area, is strongly FS dependent; highest for α, intermediate for β, and the lowest for γ FS. The ratio of the coherence peak intensity with respect the total spectral weight is associated to superfluid density in the cuprates [106, 107]. The present observation indicates that superconductivity with different superfluid density coexists in Sr122P.

Finally, we would like to mention the effect of impurity on the SC gap structure. A recent study on the effects of electron irradiation and natural disorder in Sr122P single crystals [108] shows that the low-temperature behavior of the penetration depth can be described by a power-law function $\Delta\lambda(T) = AT^n$, with n close to one for pristine annealed samples and larger than two for electron-irradiated ones, implying that the nodes are accidental and can be lifted by the introduction of disorder. For Ba122P, Mizukami *et al.* [109] also found that the nodal state changes to a nodeless state with fully gapped excitations by introducing nonmagnetic point defects by electron irradiation. Theoretically, Kontani *et al.* [17] proposed a possibility of crossover from $s^{\pm}$ wave to s^{++} wave with increasing the impurity concentrations. The present annealed samples, which yielded $n \sim 1$ in Strehlow *et al.*'s penetration depth measurement [108], can be reasonably regarded as "pure", and a comparison with theory with low impurity concentration is justified. To further clarify this issue, direct ARPES investigation into the change of SC gap structure with different impurity concentrations is left for future studies.

3.4 Conclusion

In conclusion, we have measured the SC gaps of optimally-doped Sr122P in the wide three-dimensional momentum space by laser-based and synchrotron-radiation ARPES. Around the Z point, the α and β hole FSs have isotropic SC gap of 8 meV

and 6 meV, respectively. The gap on the γ FS is anisotropic with the amplitude of 5 meV with minima along the Fe-Fe direction. The electron FSs have isotropic gap of 8 meV, and almost independent of the k_z. As for the location of nodes, we propose that there exists dramatic reduction or a possible sign change in the γ hole FS, around the Z point, and around the $\theta = 0^\circ$ line. The present observation is qualitatively consistent with the theoretical calculations based on spin-flucutuation exchange. We also found the spectral weight of the coherence peak is the highest for the inner hole FS and the lowest for the outer hole FS, which suggests that superconductivity with different superfluid density coexists in Sr122P.

Chapter 4

Time- and angle-resolved photoemission spectroscopy of $BaFe_2As_2$

4.1 Introduction

Ultrafast phenomena in condensed matter have been the subject of intense research after the advent of ultrafast laser. In order to investigate nonequilibrium transient states in solids, the pulsed photons are divided into pump and probe portions: pump pulses excite the system and the probe pulses measure various physical quantities of the transient states after a variable delay time. On the other hand, angle-resolved photoemission spectroscopy (ARPES) is a versatile tool to study the electronic structure of solids with momentum resolution. Combining these strengths, time- and angle-resolved photoemission spectroscopy (TrARPES) was realized shortly after the technological achievement of laser-based ARPES. TrARPES technique has been utilized to study ultrafast dynamics of various materials including charge-density-wave materials [110, 111], cuprate superconductors [112], graphene [113, 114], and topological insulators [115, 116].

$BaFe_2As_2$ (Ba122), one of the parent compounds of iron-based superconductors (FeSCs), exhibits stripe-type antiferromagnetic (AFM) order below the Néel temperature (T_N) of 138 K. Nesting between the hole Fermi surfaces (FSs) at the zone center and electron ones at the zone corner is considered to enhance the spin-density-wave instability with the ordering vector $\boldsymbol{Q} = (\pi/a, \pi/a, 2\pi/c)$. The AFM order coexists with the orthorhombic lattice distortions, which entails the orbital differentiation between the d_{xz} and d_{yz} orbitals. Due to the availability of high-quality single crystals, the equilibrium electronic structure of Ba122 and that of the doped superdoncutors have been extensively studied in order to clarify the competition and interplay between various order parameters [117–119].

As for time-resolved experiments of FeSCs, coherent A_{1g} phonon oscillations have been found in various physical quantities in previous studies. Mansart *et al.* [43] found oscillatory components overlaid on exponential decay in the transient reflectivity spectra of $Ba(Fe_{0.92}Co_{0.08})_2As_2$. TrARPES studies on $Ba/EuFe_2As_2$ [44, 45] found oscillations of the chemical potential of the electrons after the pump pulse. Time-resolved x-ray diffraction experiments [47, 49] directly measured the oscillations of the intensity of the Bragg reflections from $BaFe_2As_2$. Although the existence of coherent lattice dynamics has been well established so far, a natural question remains: Since the first process is the absorption of photons by the excitation of valence electrons, electron distribution should be observed well above E_F, up to the photon energy ($h\nu$) of pump beam. Furthermore, since it is not to the crystal lattice but to the electronic system that the optical pump directly transfers its energy, modifications of the electronic structure should precede the subsequent excitation of phonons, as described by phenomenological two-temperature models [50,51]. Here, because the rise of the electronic temperature after optical excitation is higher than T_N, the electronic system may undergo a phase transition to the paramagnetic (PM) state. In equilibrium, the reconstruction of the band structure across the SDW transition was clearly observed by ARPES by changing temperature [120]. Therefore, one expects that the phase transition can be induced by optical pump and the relaxation to the SDW ground state is detectable by TrARPES. Furthermore, since investigations into SDW materials by TrARPES have limited, TrARPES studies will give us insight into the dynamics of SDW formation in general.

To perform TrARPES, probe beam with $h\nu$ larger than work functions of solids is required, which is normally achieved by employing higher harmonics (HHs) generated through nonlinear crystals like β-BaB_2O_4; however, the $h\nu$ is typically below 6-7 eV, limiting accessible momentum space close to the Γ point. For FeSCs, in particular, the information about electron pockets around the X point cannot be obtained. To overcome this hurdle, we have employed HHs generated by focusing fundamental light to rare gas jet [121]. This method can create photons in the extreme ultraviolet regime ($h\nu > 20$ eV), which are high enough to probe the entire Brillouin zone (BZ) of FeSCs. A previous work by Yang *et. al.* [46] utilized a similar setup and observed a global oscillation of the chemical potential due to the A_{1g} photon modes of As atoms both at the Γ and X points. However, the time-resolved data in that work were limited to temporal evolution of energy distribution curves (EDCs).

4.2 Experimental

In the present work, we have performed TrARPES measurements of the SDW state in Ba122 in order to directly measure transient spectral functions both around the Γ and X points. The fundamental laser systems are 1 kHz Ti:Sapphire lasers operating at a wavelength (λ) of 790 and 800 nm, respectively, with a pulse width of 90 fs. The second harmonics with $\lambda = 394$ and 400 nm generated by a 0.5-mm-thick β-BaB_2O_4 crystal are employed as the source of HH generation. HHs were generated by irradiating the second harmonics to Ar gas jet and the 9th harmonics with $h\nu = 28.3$ and 27.9 eV were selected by a pair of SiC/Mg multilayer mirrors by suppressing other higher harmonics [122]. Ba122 single crystals were cleaved *in situ* prior to measurements to obtain fresh surfaces. Cleavage occurs along the ab plane. Single crystals were not detwinned and, therefore, the ARPES intensity is the superposition of intensities from two inequivalent domains in the SDW state. The kinetic energies and the momenta of photoelectrons were measured using a Scienta R4000 hemispherical electron energy analyzer. The total energy resolution was 250 meV. All the measurements were done at 10 K, which was well below the T_N of the equilibrium SDW state. The structure of Ba122 in the PM state has a space group symmetry of I4/mmm and its first BZs for the PM and antiferromagnetic (AFM) states are shown in Fig. 4.1 (c). We shall use the notation of the PM BZ to specify positions in momentum space. In-plane (k_X, k_Y) and out-of-plane (k_z) momenta are expressed in units of π/a and $2\pi/c$, respectively, where $a = 3.97$ Å and $c = 13.00$ Å are the in-plane and out-of-plane lattice constants, respectively. The k_X, k_Y, k_z axes are also shown in Fig. 4.1 (c).

Before going to the experimental results, I summarize experimental hurdles specific to the present work on Ba122. First and formost, it needed great care to reduce the space-charge effects between photoelectrons. Since HH generation is a nonlinear optical process, the fundamental laser pulse width must be made as short as possible in order to increase the instantaneous amplitude of the electric field. However, the HHs generated in this way excite too much photoelectrons instantaneously and the space-charge effect between them was extremely large, making it almost impossible to obtain reasonable TrPES spectra. In particular, Ba122 is a multiband system with a high DOS near E_F, and the space-charge effect in Ba122 is much stronger than in other materials recently studied such as graphene and cuprate superconductors. In order to avoid this, we had to severely reduce the fundamental laser fluence by carefully keeping finite count rates. This process makes the photoemission count rate extremely low. It took about one entire week to obtain the results below for each cut. Still, the signal-to noise ratio is not enough to allow qualitative analysis of EDCs. To overcome this difficulty, higher repetition rate of fundamental laser, and improvement of the shape of the metallic tube for more efficient HH

generation are desired in future.

Second, since the photoemission intensity from HHs is extremely weak and the resolution is above 200 meV, it is impossible to map out the FS or to know the exact momenta by looking at the ARPES spectra. To perform reliable measurements, He discharge lamp must also be equipped to the measurement chamber as another photon source. The actual measurements were performed as follows: First, we map out the FS by He discharge lamp in order to check the direction of the sample and to find the manipulation rotation angles corresponding to normal emission. Then we switch to the HHs, and rotate the sample to desired positions.

4.3 Results and discussion

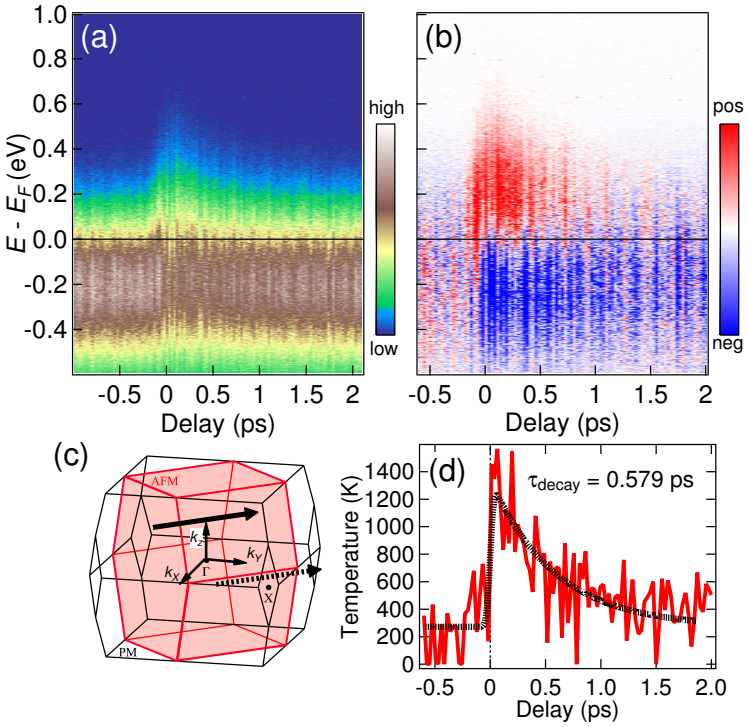

Figure 4.1: (a) Temporal evolution of angle-integrated photoemission intensity around the $(0, 0, 6.5)$ point of the Brillouin zone (BZ). (b) Difference spectra of (a) from the average intensity before the arrival of pump pulse. (c) First BZs of the paramagnetic (black) and antiferromagnetic (red) states. We shall use the paramagnetic notation below. Solid and dotted arrows indicate the momentum cuts for the $(0, 0, 6.5)$ and $(1, 1, 6.1)$ point, respectively. (d) Temporal evolution of the electronic temperature (T_e). T_e is evaluated by fitting the photoemission intensity to the Fermi-Dirac distribution function convoluted with the instrumental function. Black dotted line shows the fit to a decay function of the form $T_e(t) = A + B\Theta(t)\exp(-t/\tau_{\text{decay}})$, where $\Theta(t)$ is the Heaviside step function.

Now we move on to the experimental results. Figure 4.1 (a) shows the temporal evolution of angle-integrated photoemission (PES) spectra around the zone center. With $h\nu = 27.9$ eV probe photons the momentum cut is on the $k_z = 6.5(2\pi/c)$ plane as shown by a solid arrow in panel (c). One sees that upon the arrival of a pump pulse at $t = 0$, the electron population above the Fermi level (E_F) suddenly increases and it decays afterwards. To improve the visibility of the data, we show difference spectra in Fig. 4.1 (b). Here, the average spectrum before $t = 0$ has been subtracted. It is clear that just after $t = 0$ the population above E_F increases while that below E_F decreases, and that the population inversion is weakened with delay time. In order to quantify the transient state, we show in Fig. 4.1 the electronic temperature T_e as a function of delay time. T_e is determined by fitting the PES intensity at each delay time to a Fermi-Dirac distribution function convoluted with the Gaussian with a resolution of 250 meV. After the pulse, T_e reaches ~ 1400 K. T_e has been fitted to a decay function of the form $T_e(t) = A + B\Theta(t)\exp(-t/\tau_{\text{decay}})$ where $\Theta(t)$ is the Heaviside step function. The best fit is shown by a dotted curve. We obtain a decay constant of $\tau_{\text{decay}} = 0.579$ ps around the Γ point.

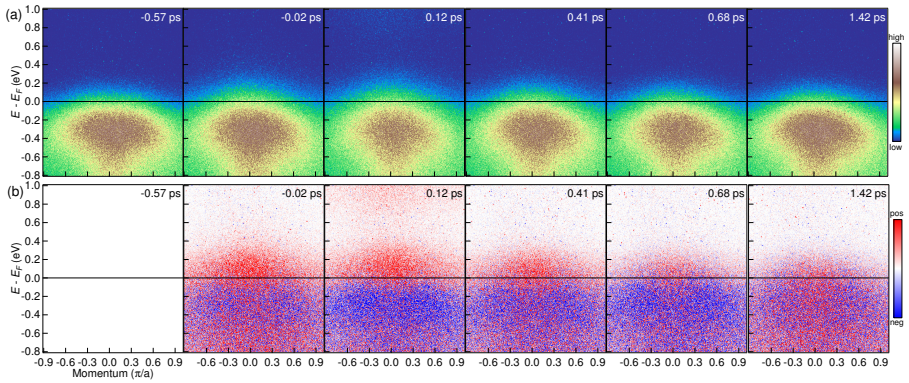

Figure 4.2: (a) Time-resolved angle-resolved photoemission (ARPES) spectra around the $(0, 0, 6.5)$ point. (b) Difference TrARPES spectra from the spectrum before the pump arrival (-0.47 ps).

In order to study the momentum-resolved spectral function during the relaxation, we show in Fig. 4.2 (a) the TrARPES spectra taken at different delay times. The momentum cut is the same as that of Fig. 4.1. To highlight the change of the spectra, we also show difference TrARPES spectra in Fig. 4.2 (b). Here, the spectrum at -0.47 ps has been subtracted from each spectrum. Before the pump pulse (-0.47 ps), the spectrum represents that of the SDW state. Although the identification is not obvious under the resolution of the present setup, we consider the spectra to be those of the SDW state from comparison with ARPES data at 10 K ($< T_N$) and 200 K ($> T_N$). After the arrival of pump pulse ($t \geq -0.02$ ps), electrons start to occupy states above E_F. At 0.12 ps, we observe an inversely populated states

above the gap ($E - E_F > 0.6$ eV) which have parabolic intensity distribution. At 0.41 ps, this inverse population disappears, indicating the fast decay of electrons. As for the intensity between $0 < E - E_F < 0.4$ eV, it already exists at -0.02 ps, reaches maximum around 0.12 ps, and slowly decays as a function of time. At 1.42 ps, there is almost no separation of positive and negative area in the difference spectrum, indicating that the electronic system has relaxed back to the equilibrium state.

Here we discuss the implications of the present data for ultrafast phase transition. In the following, we argue that the observed hot electron states are likely to be those of the PM states caused by the melting of the SDW state. We compare in Figs. 4.3 (a) and (b) the difference spectrum at 0.12 ps and calculated band dispersion at $k_z = 6.5$ $(2\pi/c)$ in the PM state. For the intensity increase shown by red, we observe a population inversion above 0.6 eV and a gap between $0.4 < E - E_F < 0.6$ eV. This is qualitatively consistent with the calculated PM band structure shown in Fig. 4.3 (b), and quantitatively the smaller gap in experiment can be ascribed to the experimental resolution of 250 meV. However, there also is slight intensity increase between the gap, $0.4 < E - E_F < 0.6$ eV. Here we list possible reasons for this. The first possibility is that not the entire measured region exhibits phase transitions. Since the beam profile of the probe beam is a gaussian, there always is inhomogeneity in the pumping power in the sample. Therefore some portion of the probed area may remain in the SDW state, which can contribute to the increased count in $0.4 < E - E_F < 0.6$. The second possibility is the contribution from the multiphoton absorption. Since we utilized pulse laser for the photoexcitation of the electrons, there is a large possibility for electrons to absorb more than one photon. Multiphoton absorption is particularly strong when the pump and probe pulses overlap since it is a nonlinear process. Since the multiphoton absorption does not require intermediate states unlike in the absorption of pump photons, it may contribute to finite counts where the unoccupied states do not exist.

In order to argue that the transient spectrum at 0.12 ps is not that of SDW, it would be helpful to compare the data with the DFT calculation of the SDW state. Since the Ba122 samples were not detwinned, we show the results for two inequivalent domains in Fig. 4.3 (c). It is well known that electronic structure calculations of the parent compounds of FeSCs greatly overestimate the AFM ordered moment [123, 124], and the reduction of the ordered moment by the LDA+U method with negative U greatly modifies the band structure [120]. However, Terashima *et al.* [125] showed that the standard DFT calculation reasonably accounts for the AFM FSs of Ba122 determined by the Shubnikov-de Haas oscillation measurements. Therefore we have used the standard GGA functional and reproduced the results of Terashima *et al.*. One observes that there are much more bands near E_F in the SDW state due to the AFM band folding. In particular, the band bottoms of

domain 1 at 0.3 eV and the flat band at 0.6 eV of domain 2 are not clearly resolved in the present measurement. However, we cannot rule out the possibility that the weak intensity increase between $0.2 < E - E_F < 0.6$ originates from these SDW bands.

To gain further insight from the intensity decrease shown in blue, equilibrium spectra taken with $h\nu = 63$ eV (Z point) for the SDW (20K) and PM (150 K) states are shown in Figs. 4.3 (d) and (e), respectively. We note that the blue intensity in panel (a) shows a parabolic feature as indicated by a blue dotted line. We ascribe this to a parabolic feature observed in the equilibrium the SDW state as indicated by a black dotted line in Fig. 4.3 (d), which does not appear in the PM state [Fig. 4.3 (e)]. The disappearance of this feature by raising the temperature from the SDW state to the PM state is also reported in Ref. 120. Thus the data at -0.47 ps can be naturally assigned to those of the SDW state, as expected from the sample temperature 10 K $< T_N$ in the equilibrium state.

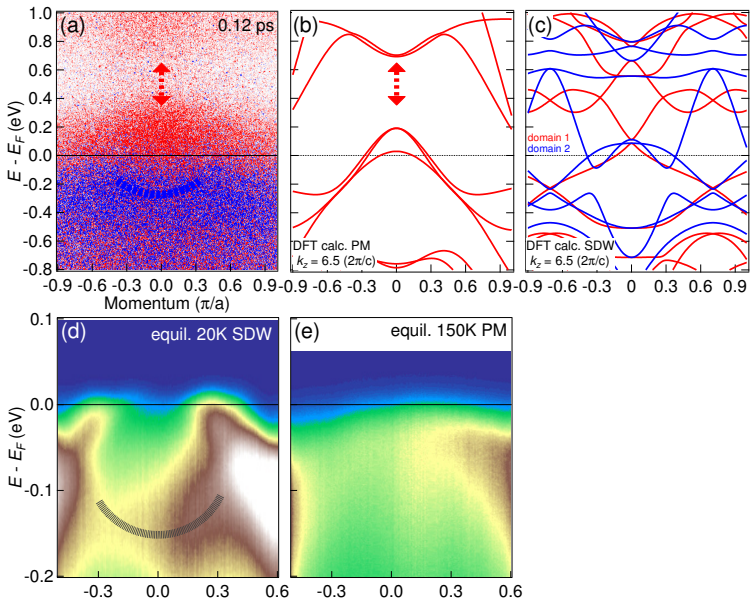

Figure 4.3: (a) Difference TrARPES spectrum at 0.12 ps. The blue dotted curve is a guide to the eye indicating a characteristic parabolic intensity decrease. Blue dotted line indicates the bottom of a characteristic parabolic feature. (b),(c) Density-functional theory (DFT) band structure around the $(0, 0, 6.5)$ point for the PM and SDW states, respectively. (d), (e) Equilibrium ARPES spectra around the Z point for the antiferromagnetic (20 K) and paramagnetic (200 K) states, respectively. Black dotted line in panel (d) indicates a parabolic feature which appears only in the SDW state.

The observation of population inversion at the conduction band bottom is made possible due to the relatively slow relaxation of excited electrons across the band gap at the zone center. Indeed, inverse population after optical pump was also ob-

served in bilayer graphene but not in single layer graphene [113, 114]. Here, the existence of this band gap in bilayer graphene leads to a longer lifetime carriers at the minimum of the conduction band as compared to the Dirac cone dispersions in the monolayer one.

Next we investigate the dynamics of excited electrons around the zone corner. Figure 4.4 shows the temporal evolution of angle-integrated PES spectra at the (1,1,6.1) point. We employed $h\nu = 28.3$ eV and the momentum cut in the BZ is indicated by a dotted arrow in Fig. 4.1 (c). The difference spectra are also shown in Fig. 4.4 (b). As in the case of the (0,0,6.5) point, the intensity above E_F increases and that below E_F decreases at $t = 0$, and this change weakens with time. The evolution of T_e is plotted in Fig. 4.4 (c). T_e rises up to $\sim$ 900 K just after the pump pulse. We obtain a decay parameter 0.604 ps, close to 0.579 ps around the (0,0,6.5) point.

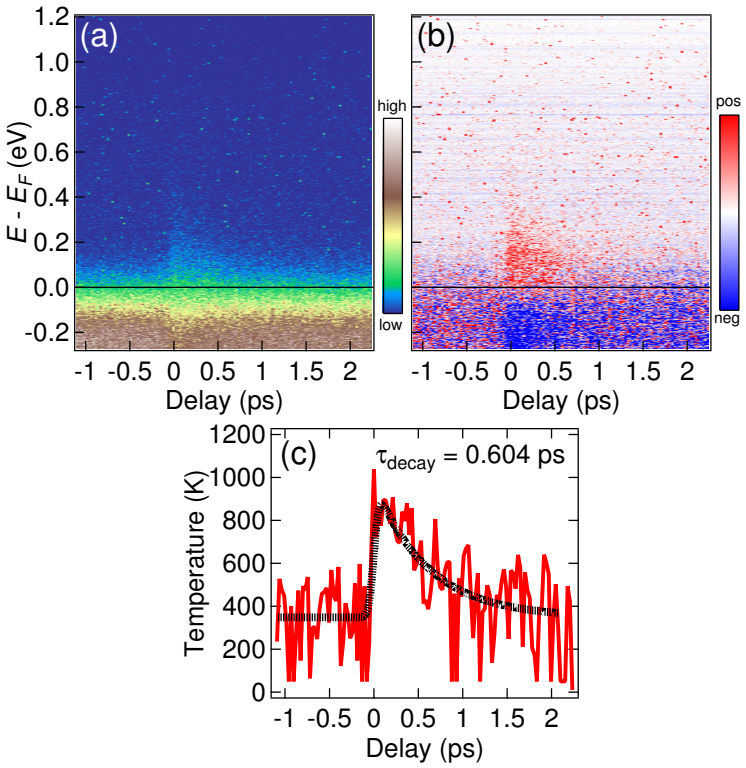

Figure 4.4: (a) Temporal evolution of angle-integrated PES spectra around the $(1, 1, 6.1)$ point. The momentum cut is indicated by a dotted arrow in Fig. 4.1 (c). (b) Difference spectra of (a) from the average intensity before the arrival of pump pulse. (c) Temporal evolution of T_e.

TrARPES spectra around the (1,1,6.1) point are shown in Fig. 4.5 (a) and the difference spectra are shown in Fig. 4.5 (b). Although the modifications in the spectra are weaker than those in the zone center, we observe an intensity increase after

the pump pulse. Note that we do not observe population inversion well above E_F within our measurement range. To understand the difference between the results for the (0,0,6.5) and (1,1,6.1) points, we also show calculated PM band structure in Fig. 4.5 (c). The lowest states above E_F at (1,1,6.1) point are located at 0.873 eV above E_F, which is much higher than those at the $(0, 0, 6.5)$ point. Furthermore, one of the two bands located around $\sim$ 1 eV above E_F is rather flat; as a result, the lifetime of excited electrons around the (1,1,6.1) point can be much shorter than around that at (0,0,6.5), because they can easily decay into different momentum states via electron-phonon and/or electron-electron interactions. To support the interpretation, we also show the calculated SDW band structure for two domains in Fig. 4.5 (d). As in the (0,0,6.5) point, there are more bands in the SDW state than in the PM state. In particular, there are three electron band bottoms between $0.2 < E - E_F < 0.6$ eV, where long exciton lifetime is expected. The absence of the observation of transient population in this range corroborates our assignment of the transient state between 0.1 and 0.2 ps to the PM state. However, there also is possibility that reduced phototemission matrix element at the zone corner prevented us from observing the population inversion. In the present experimental setup, four different photon energies are available, and it is possible to probe different k_z by selecting higher photon energies. Future measurements of different k_z will help us better interpret the present observations.

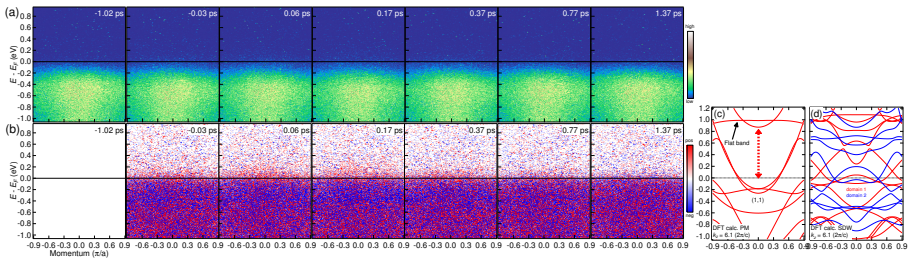

Figure 4.5: (Color online) (a) TrARPES spectra around the $(1, 1, 6.1)$ point. (b) Difference TrARPES spectra from the spectrum before the pump arrival ($t = -1.02$ ps). (c),(d) DFT band structure around the (1,1,6.1) point in the PM [(c)] and AFM [(d)] states, respectively.

While the hot electrons above the band gap decay quickly (< 0.41 ps), the hot electrons close to E_F persist for a longer time, which can be interpreted as the thermalized electronic states. For the time scale of the relaxation of near-E_F states, we compare the present decay constants with those from previous works. The present value $\sim$ 0.60 ps for 10 K is close to 0.8 ps for $EuFe_2As_2$ [44], 0.38 ps for Ba122 [46] . Also, it is comparable with 0.6-0.8 ps for superconducting $Ba_{1-x}K_xFe_2As_2$ [126] estimated from time-resolved reflectivity. As for the A_{1g} phonon modes, we did not observe oscillatory intensity modulation near E_F. Mansart *et al.* [43] performed time-resolved reflectivity measurements of $Ba(Fe_{0.92}Co_{0.08})_2As_2$ with various pump

fluences and found that, while the phonon oscillation is barely visible at $\sim$ 1.3 mJ/cm^2 in the course of the exponential decay of the reflectivity, it becomes more prominent at higher flux ($\sim$ 2 mJ/cm^2) and makes the relaxation slower. We need further investigation into the pump fluence dependence of the transient states in the future.

4.4 Conclusion

In conclusion, we have studied the ultrafast dynamics of the $BaFe_2As_2$ in the SDW state by TrARPES from rare-gas HHs. The probe photons with the $h\nu$ of 27.9 and 28.3 eV have been created by HH from Ar gas jet, high enough to investigate the dynamics at the Brillouin zone corner, which is inaccessible by conventional HHs from nonlinear crystals. We observed electronic modifications from the SDW band structure within $\sim$ 1 ps after the 1.5 eV pump pulse. Inverse populations above the band gap above E_F were observed at 0.12 ps at the zone center and they decay rapidly. The 0.12 ps spectrum is consistent with the band structure calculation of the PM state, which is expected from the high electronic temperature above 1000 K. However, under the present resolution of 250 meV, interpretation of the data within the SDW is also possible. For clarifying this issue, measurements with different photon energy will be necessary. After the fast decay of the optically excited electrons, a thermalized state appears and survives for a relatively long time. Decay constants both around the Γ point and the X point are $\sim$ 0.60 ps, in agreement with previous TrARPES and time-resolved reflectivity measurements.

Chapter 5

Soft x-ray spectroscopic studies of $\mathbf{Ba_{1-x}K_x(Zn_{1-y}Mn_y)_2As_2}$

Part of this chapter is based on published papers "Photoemission and x-ray absorption studies of the isostructural to Fe-based superconductors diluted magnetic semiconductor $Ba_{1-x}K_x(Zn_{1-y}Mn_y)_2As_2$", H. Suzuki, K. Zhao, G. Shibata, Y. Takahashi, S. Sakamoto, K. Yoshimatsu, B. J. Chen, H. Kumigashira, F.-H. Chang, H.-J. Lin, D. J. Huang, C. T. Chen, Bo Gu, S. Maekawa, Y. J. Uemura, C. Q. Jin and A. Fujimori, Phys. Rev. B **91**, 140401(R) (2015) (Editor's Suggestion) and "Fermi Surfaces and p-d Hybridization in the Diluted Magnetic Semiconductor $Ba_{1-x}K_x(Zn_{1-y}Mn_y)_2As_2$ Studied by Soft X-ray Angle Resolved Photoemission Spectroscopy", H. Suzuki, G. Q. Zhao, K. Zhao, B. J. Chen, M. Horio, K. Koshiishi, J. Xu, M. Kobayashi, M. Minohara, E. Sakai, K. Horiba, H. Kumigashira, Bo Gu, S. Maekawa, Y. J. Uemura, C. Q. Jin and A. Fujimori, Phys. Rev. B **92**, 235120 (2015).

5.1 Introduction

Diluted magnetic semiconductors (DMSs) have received much attention due to the possibility of utilizing both charge and spin degrees of freedom in electronic devices [52–54, 56, 75]. In order to realize functional spintronics devices, it is important to have a full control of the carrier density and ferromagnetic Curie temperature (T_C). Prototypical DMS systems such as $Ga_{1-x}Mn_xAs$, $In_{1-x}Mn_xAs$ and $Ga_{1-x}Mn_xN$, however, show severely limited chemical solubility due to the substitution of divalent Mn atoms for the trivalent Ga or In sites. Besides, the simultaneous doping of charge and spin induced by Mn substitution prevents us from optimizing the charge and spin densities independently, although the tuning of the charge density by applying gate voltage is possible and can be used to control T_C [127].

A newly-found DMS, $Ba_{1-x}K_x(Zn_{1-y}Mn_y)_2As_2$ [84] (Mn-$BaZn_2As_2$), is isostructural to the "122"-type iron-based high-temperature superconductors [2] and has a T_C as high as 230 K [85]. This material has an advantage that the charge reservoir Ba layer and the ferromagnetic ZnAs layer are spatially separated, which allows us to control the amount of hole carriers by K substitution to the Ba layer and that of magnetic elements by substituting Mn to the ZnAs layer rather independently. In addition, the substitution of Mn atoms for isovalent Zn atoms enables us to circumvent the difficulty of limited chemical solubility in $Ga_{1-x}Mn_xAs$ and related DMSs, which makes it possible to obtain bulk specimens. Anomalous Hall effect observed in Mn-$BaZn_2As_2$ [84] provides evidence that ferromagnetism here is intrinsic as in $Ga_{1-x}Mn_xAs$ [128, 129]. This new series of DMSs, together with the new "111"-type materials Li(Zn,Mn)As [82] and Li(Zn,Mn)P [83], opens up new possibilities for the next generation spintronics devices. To achieve this goal, it is important to investigate the electronic and magnetic structure of Mn-$BaZn_2As_2$ and clarify the advantages of this material as compared with the archetypal Mn-doped-based DMS materials like $Ga_{1-x}Mn_xAs$ and $In_{1-x}Mn_xAs$. Furthermore, Mn-$BaZn_2As_2$ bulk single crystals have recently been successfully synthesized with T_C = 60 K ($x = 0.3$, $y = 0.15$) [130]. This is an important step toward the understanding of the electronic structure of this material and consequently the mechanism of carrier-induced ferromagnetism in DMSs in general. Also, a magnetic anisotropy has been found in the magnetization hysteresis curves with the easy axis along the c-axis [130]. For future applications, this magnetic anisotropy leads to the possibility of high density storage device design.

In the present chapter, we have performed x-ray absorption spectroscopy (XAS) and resonance photoemission spectroscopy (RPES) measurements on Mn-$BaZn_2As_2$ ($x = 0.3$, $y = 0.15$, $T_C = 180$ and 230 K). We have also performed x-ray magnetic circular dichroism (XMCD) and resonant inelastic x-ray scattering (RIXS) measurements on Mn-$BaZn_2As_2$ ($x = 0.3$, $y = 0.15$, T_C = 60 K) single crystals to study the magnetic ground state and electronic excitations of Mn. XMCD directly probes the ferromagnetic component of magnetic moments in the ground states and RIXS allows us to investigate electronic excitations with element specificity. Here, we study the magnetic states and electronic configuration of Mn by utilizing photons around the Mn $L_{2,3}$ edge.

Polycrystalline samples were synthesized under high pressure by the method described in Ref. 84. XAS measurements for samples with $T_C = 230$ K were performed at the Dragon Beamline BL-11A of National Synchrotron Radiation Research Center (NSRRC), Taiwan. The spectra were taken in the total-electron yield (TEY: probing depth $\sim$ 5 nm) mode. The monochromator resolution was $E/\Delta E > 10000$ and the x-rays were circularly polarized. The samples were filed *in situ* before the measurements to obtain fresh surfaces. photoemission experiments

for polycrystalline samples with $T_C = 180$ K and single crystals were performed at Beamline 2 of Photon Factory, High-Energy Accelerator Research Organization. Calibration of the Fermi level (E_F) was achieved using the E_F of gold which was in electrical contact with the samples. Incident photon energies from 635 eV to 643 eV were linearly polarized. In order to gain insight further into the electronic structure of the host semiconductor $BaZn_2As_2$, we have performed density-functional theory (DFT) calculations.

XMCD measurements were performed at the Dragon Beamline BL-11A of National Synchrotron Radiation Research Center (NSRRC), Taiwan. X-ray absorption (XAS) and XMCD spectra were taken in the total-electron yield (TEY: probing depth $\sim$ 5 nm) mode. XMCD signal is defined as the difference between absorption spectra taken with circularly polarized x-rays of different helicities. Here, the XMCD spectrum was obtained by switching the direction of the external magnetic field (± 1 T). The monochromator resolution was $E/\Delta E > 10000$. The single crystals oriented along the c-axis (2 mm $\times$ 2 mm) were cleaved *in situ* before the measurements to obtain fresh surfaces. External magnetic field was applied along the c axis and the angle between the incident light and the magnetic field was 30°. RIXS measurements were performed at the undulator beam line BL-05A1 of NSRRC. The optical layout of the present RIXS system with an active-grating monochromator and an active-grating spectrometer designed for the efficient collection of inelastically scattered x-rays is described in Ref. 97. The zero energy loss line is determined from the peak position of the elastic scattering peak of reference polycrystalline carbon and the total energy resolution around the Mn L_3 edge estimated from its full width half maximum was 80 meV ($E/\Delta E \simeq 8000$). The RIXS spectra were measured with two linear polarizations at 20 K under a vacuum of 1.0×10^{-9} Torr. The polarizations of the scattered x-rays were not analyzed.

5.2 Density functional theory calculation of $BaZn_2As_2$

First, in order to understand the electronic structure of the host semiconductor, we have performed band-structure calculations on $BaZn_2As_2$ using the Wien2k package [98]. Figure 5.1 (a) shows the calculated band structure and the density of states (DOS). $BaZn_2As_2$ has space group $I4/mmm$ and the first Brillouin zone is shown in the inset of the right panel. The calculations were done using the experimentally determined tetragonal lattice constants $a = 4.12$ Å, $c = 13.58$ Å [84] and the arsenic height $h_{\mathrm{As}} = 1.541$ Å [131]. First we tried the local density approximation (LDA) and generalized gradient approximation (GGA) exchange functionals [132,133], but they gave overlapping conduction and valence bands, inconsistent with the semiconducting electrical conductivity with a band gap of 0.23 eV [134]. This is the well-known underestimation of band gap in LDA and GGA, and there-

fore we next employed the so-called modified Becke-Johnson exchange potential (mBJ) implemented in Wien2k program [135] with a standard mixing factor for the exact-exchange term of 0.25 [136]. We thus obtained a semiconducting band structure with the valence-band maximum at the Γ point and the conduction-band minimum at the Z point, in agreement with the previous calculation using optimized atomic positions [137]. A significant reduction of the resistivity at $T = 0$ through K substitution to $BaZn_2As_2$ [84], from 1×10^4 Ω cm ($x = 0$) to 5×10^{-1} Ω cm ($x = 0.1$), is caused by the downward shift of E_F. Unlike the iron pnictide superconductors, the conduction bands are composed mainly of Ba $5d$ and As $4d$ orbitals, and the valence bands are composed of the Zn $4p$ and As $4p$ orbitals. Weakly dispersive bands around -7.5 eV originate from the Zn $3d$ orbitals and have a DOS as high as 50 eV^{-1} at the peak position.

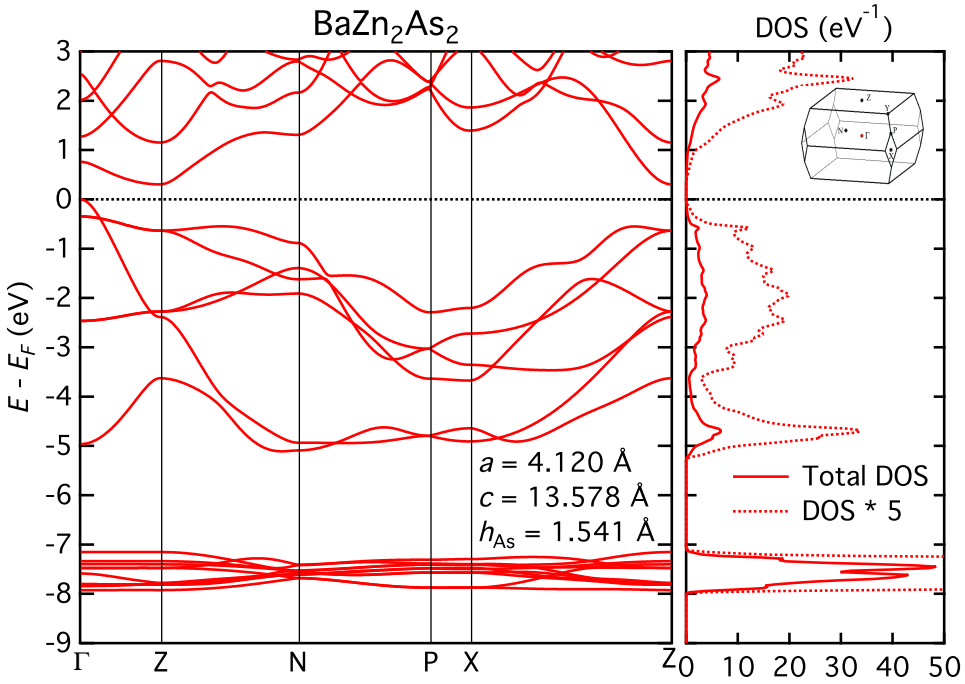

Figure 5.1: Band structures and the density of states for $BaZn_2As_2$ calculated using modified Becke-Johnson exchange potential. The lattice parameters $a = 4.120$ Å , $c = 13.578$ Å [84] and $h_{\mathrm{As}} = 1.541$ Å [131] are used in the calculation.

5.3 X-ray absoption spectroscopy

In order to clarify the electronic states of the doped Mn, we have performed XAS measurements in the photon energy regions around the $L_{2,3}$ edge of Mn. Figure 5.2

shows the Mn $L_{2,3}$ absorption edges of $Ba_{0.7}K_{0.3}(Zn_{0.85}Mn_{0.15})_2As_2$ compared with those of some reference systems. The line shapes of $Ba_{0.7}K_{0.3}(Zn_{0.85}Mn_{0.15})_2As_2$ is intermediate between two DMS systems $Ga_{0.922}Mn_{0.078}As$ [138] (GaMnAs) and $Ga_{0.958}Mn_{0.042}N$ [139] (GaMnN), indicating that the Mn atoms take the valence of 2+ and that Mn $3d$ orbitals strongly hybridize with the surrounding As $4p$ orbitals as in GaMnAs and GaMnN. From the shoulder structures around $h\nu = 640$ and 643 eV, which are more pronounced than in GaMnAs and weaker than in GaMnN, we see that the strength of hybridization is weaker than in GaMnAs but stronger than in GaMnN. The line shape has more localized nature than metallic compounds Mn metal [140] and Mn doped into $BaFe_2As_2$ [141]. However, it does not have clear multiplet structures seen in the spectra of $LaMnO_3$ and MnO [142], consistent with the semi-metallic conductivity in Mn-$BaZn_2As_2$.

5.4 Resonant photoemission spectroscopy

In order to extract the local electronic structure of the doped Mn, we performed RPES experiments using photon energies around the Mn L_3 edge. In RPES, one makes use of the property that the cross-section of photoemission from an atomic orbital is enhanced by quantum-mechanical interference between direct photoemission of a d electron, $3d^n + h\nu \rightarrow 3d^{n-1} + e^-$, and absorption followed by a Coster-Krönig transition $2p^6 3d^n + h\nu \rightarrow 2p^5 3d^{n+1} \rightarrow 2p^6 3d^{n-1} + e^-$ [143, 144]. This effect is useful in extracting the $3d$ partial density of states (PDOS) of a transition element in solids. Following the observed x-ray absorption spectra, we measured the valence-band photoemission spectra with photon energies from the off-resonance to on-resonance regions. A series of photoemission spectra taken with a small photon energy interval enables us to clearly identify the resonance enhancement of Mn $3d$-related photoemission features.

Figure 5.3 (a) shows the valence-band spectra taken with photon energies in the Mn L_3 absorption region. Photon energies used are shown by arrows on the XAS spectrum in panel (b). The high DOS of the Zn $3d$ states is clearly observed $\sim$ 10 eV below E_F. Note that, regardless of hole doping in Mn-$BaZn_2As_2$, the Zn $3d$ peak is located at $\sim$ -10 eV. (In DFT calculation, it is calculated to be $\sim$ -7.5 eV, see Fig. 5.1. Similar discrepancy of the Zn $3d$ energy level between DFT and photoemission is also found in Zn-doped $BaFe_2As_2$ [145, 146].) Photon-energy-independent peaks observed at -15 eV and -18 eV originate from the Ba $5p$ and K $3p$ orbitals, respectively. Most importantly, one can see the enhancement of spectral features in -8 $\sim$ 0 eV as the photon energy approaches on-resonance energy at 638.5 eV and the subsequent reduction of spectral weight at higher photon energies.

In order to highlight the resonance enhancement of Mn $3d$-derived spectral weight, we show on-off the difference spectra in Fig. 5.9. The off-resonance spec-

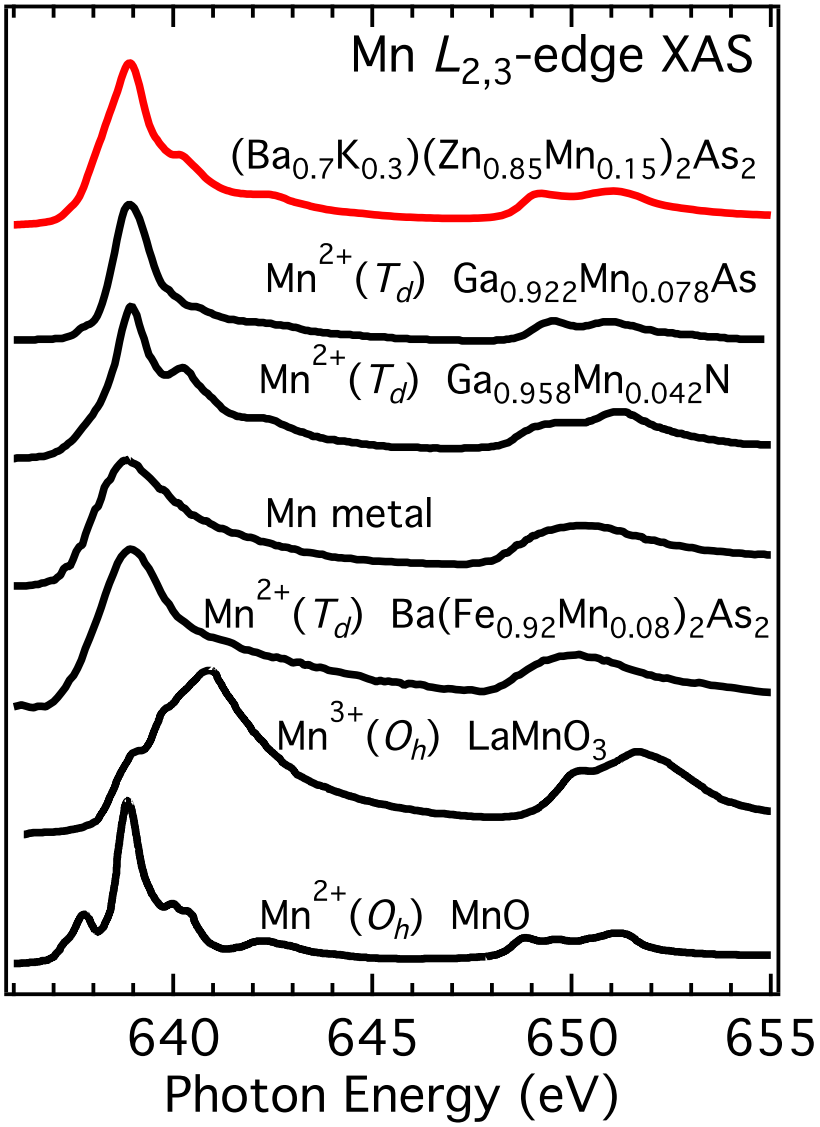

Figure 5.2: Mn $L_{2,3}$-edge XAS spectra of $Ba_{0.7}K_{0.3}(Zn_{0.85}Mn_{0.15})_2As_2$ (Mn-$BaZn_2As_2$). The spectrum is compared with those of $Ga_{0.922}Mn_{0.078}As$ [138], $Ga_{0.958}Mn_{0.042}N$ [139], Mn metal [140], $Ba(Fe_{0.92}Mn_{0.08})_2As_2$ [141], $LaMnO_3$, and MnO [142]. The valence and the local symmetry of the Mn atom are indicated for each compound.

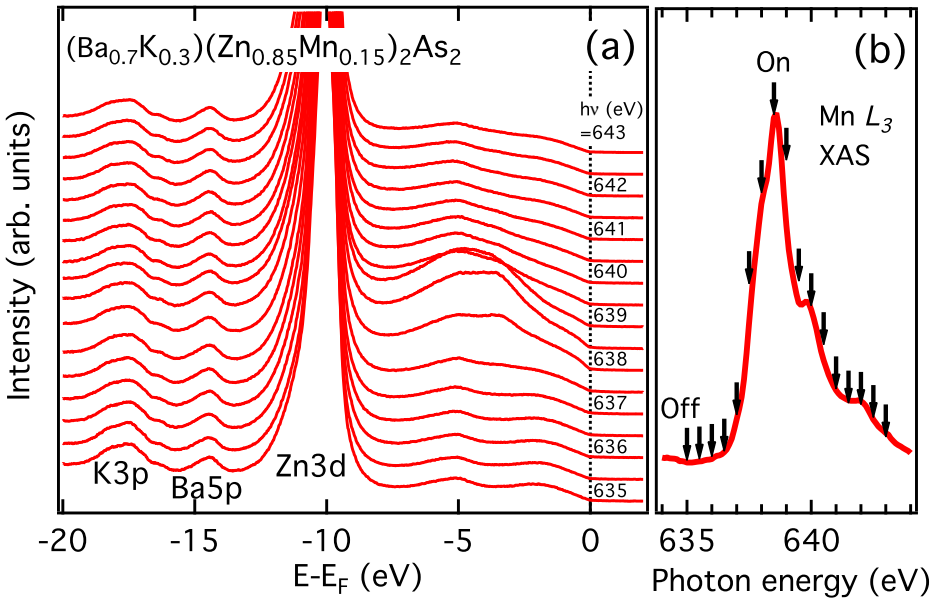

Figure 5.3: (a) Evolution of the valence-band photoemission spectra of Mn-$BaZn_2As_2$ with photon energy $h\nu$ = 635-643 eV. Excitation photon energies are shown by arrows on the XAS spectrum in panel (b).

trum ($h\nu$ = 635 eV) at the bottom of Fig. 5.9 (a) has been subtracted from each spectrum. The strongest enhancement around the Mn L_3 edge ($h\nu$ = 638.5 eV) is seen around -4 eV. Vertical bars indicate a constant kinetic energy characteristic of Auger emission. The absence of clear Auger peaks represents that the core hole created in the Mn $2p$ level is not efficiently screened before the Coster-Krönig decay due to the low Mn $3d$ PDOS around E_F (below). From this result, we see that the Mn $3d$ electrons are essentially localized and do not form band states with the As $4p$ valence band. The absence of Auger emission is similar to RPES spectra taken at Mn L_3 edges in Mn-doped $BaFe_2As_2$ [141], which demonstrates the localized nature of Mn $3d$ electrons in the metallic FeAs layer, and is in contrast with the strong Auger feature observed at the Co $L_{2,3}$ edges in $Ca(Fe_{0.944}Co_{0.056})_2As_2$ [148], which clearly signifies the metallic nature of Co $3d$ electrons and the high Co $3d$ PDOS at E_F.

By subtracting the off-resonance spectra from the on-resonance spectra, we have deduced the PDOS of Mn $3d$ orbitals as shown in Fig. 5.9 (b). The DOS is low at E_F, finite between -2 eV and E_F and takes a maximum at -4 eV. Mn $3d$ spectral weight is widely distributed from $\sim$ -10 eV to $\sim$ -2 eV. The deduced PDOS is compared with that of $Ga_{0.957}Mn_{0.043}As$ [147] in Fig. 5.9 (c). Except that the peak in $Ga_{0.957}Mn_{0.043}As$ is about 0.4 eV deeper than that of Mn-$BaZn_2As_2$, the

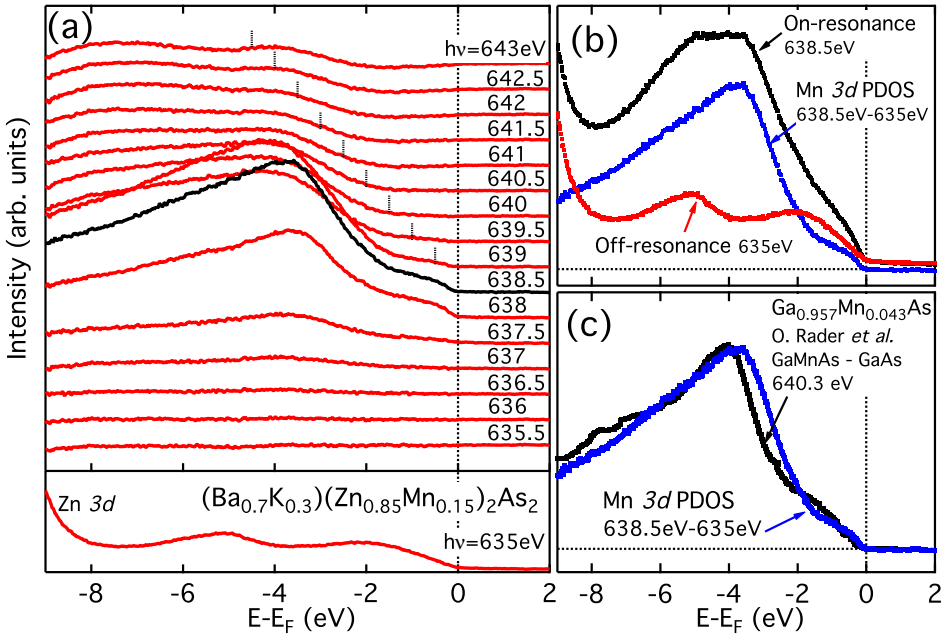

Figure 5.4: (a) Evolution of the valence-band photoemission difference spectra of Mn-$BaZn_2As_2$ for photon energies $h\nu$ = 635-643 eV. Off-resonance photoemission spectrum at the bottom of the panel ($h\nu$ = 635 eV) has been subtracted from the original spectra in order to highlight the resonant enhancement of the spectral weight. On-resonance spectrum is shown by a black curve. Vertical bars indicate a constant kinetic energy characteristic of Auger-electron emission if it existed. The absence of clear Auger peaks reflects the localized nature of the Mn 3d electrons. (b) Mn 3d partial density of states deduced by subtracting the off-resonance spectrum ($h\nu$ = 635 eV) from the on-resonance spectra ($h\nu$ = 638.5 eV). (f) Mn 3d PDOS of $Ga_{0.957}Mn_{0.043}As$ [147] compared with that of Mn-$BaZn_2As_2$.

overall spectral shapes are quite similar, indicating that the electronic states of doped Mn are alike in these two DMS systems. This similarity originates from the same chemical valence 2+ of the Mn atoms and the tetrahedral coordination by the As $4p$ orbitals.

From the obtained energy levels, we gain insight into the location of hole carriers doped by K substitution in Mn-$BaZn_2As_2$. The Zn $3d$ orbital is located as deep as 10 eV below E_F and thus cannot accommodate holes. Also, since the Mn $3d$ PDOS has a maximum at -4 eV and very little contribution at E_F, they cannot accept holes either. Therefore, holes are predominantly introduced into the valence band composed mainly of the As $4p$ states. Thus Mn atoms have the valence of 2+ as observed in the XAS spectrum in Fig. 5.2. Taking into account the total magnetization of 1.1 μ_B/Mn (Fig. 1.34), we conclude that the local magnetic moments with $S = 5/2$ are formed there in the presence of Hund's coupling between electrons of d^5 configuration. The reduction of the magnetization per Mn from the expected 5 μ_B/Mn will be discussed below together with the XMCD results.

The formation of the local magnetic moments affects the hole mobility. Upon K doping into the parent compound ($x = y = 0$), the resistivity at $T = 0$ significantly decreases from 1×10^4 Ω cm ($x = 0$) to 5×10^{-1} Ω cm ($x = 0.1$) [84]. On the other hand, it does not radically decrease in samples with $y = 0.1$, from 4 Ω cm ($x = 0$) to 2 Ω cm ($x = 0.3$). This behavior indicates that, while hole carriers introduced into the As $4p$-derived valence band are originally itinerant, they are weakly bound to the local magnetic moments and lose mobility in the Mn-doped samples.

5.5 ARPES with vacuum-ultraviolet photons

Next we move on to ARPES results on single crystals with $T_c = 60$ K. A valence band ARPES spectrum taken with $h\nu$ = 60 eV for a cut containing the Γ point is shown in Fig. 5.5. Due to the low photoemission cross section of the As $4p$ orbitals at 60 eV [149] and the short probing depth of VUV photoemission, the As $4p$ valence band was difficult to detect, although the Zn $3d$ levels were clearly detected. Unlike the parent compound of iron-pnictide superconductors, $BaFe_2As_2$, where the Fe $3d$ orbitals make dominant contribution to the electronic states near the Fermi level (E_F), the Zn $3d$ level is located at $E \sim$ -10 eV as shown in the angle-integrated spectrum (Fig. 5.5), consistent with the result on polycrystals [150].

5.6 Soft x-ray ARPES results

For SX, the photoemission cross section from the As $4p$ orbitals is larger and the probing depth is longer, providing us with information about the bulk electronic

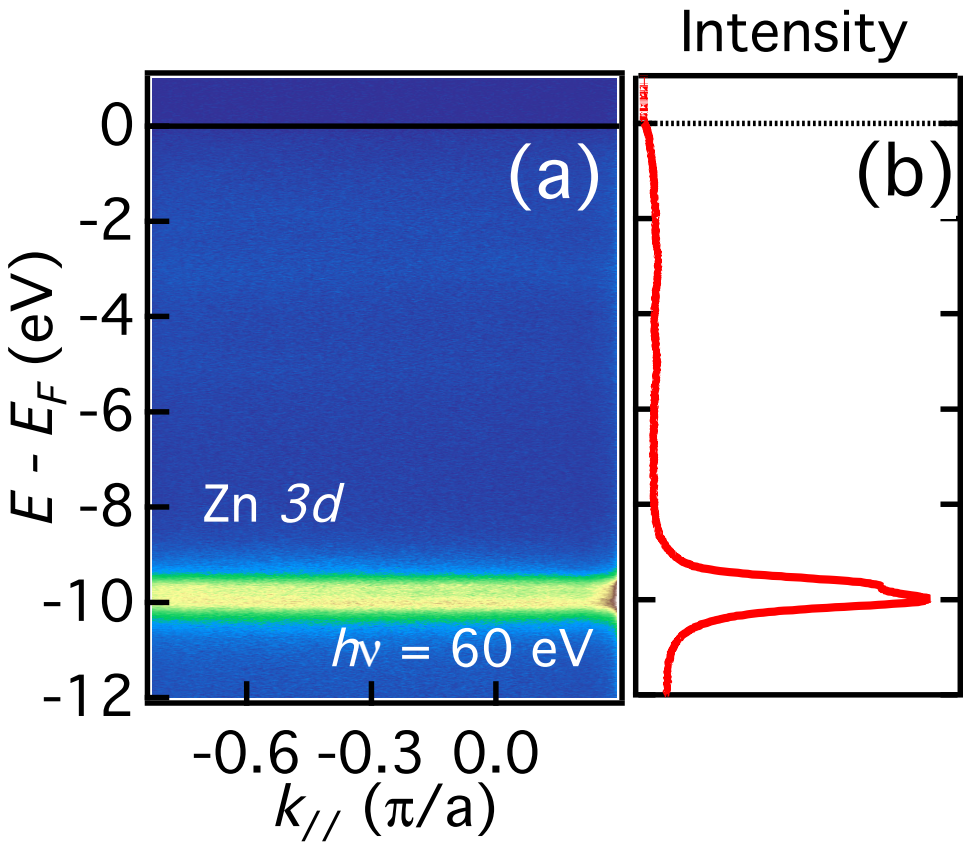

Figure 5.5: (a) ARPES spectrum taken with $h\nu = 60$ eV photons. (b) Angle-integrated photoemission spectra.

structure. Figures 5.6 (a) and (b) show ARPES spectra taken with $h\nu$ = 720 and 680 eV photons. Cuts in the first BZ are indicated in panel (e). The k_z positions for these photon energies are approximately those of the Γ and Z points, respectively. The corresponding second derivatives along the energy directions are also shown in Figs. 5.6 (c) and (d). We observe multiple dispersive bands near E_F.

To clarify the effect of hole and Mn doping on the electronic structure, we compare in Figs. 5.7 (a) and (b) the peak positions of the ARPES data and the DFT band dispersion of $Ba_{0.7}K_{0.3}Zn_2As_2$. The peak positions have been determined by fitting the energy distribution curves (EDCs) and momentum distribution curves to Gaussian-convoluted Lorentzian functions. While the experimental dispersion is qualitatively well reproduced by the DFT calculation, the band bottom/top energies are not correctly predicted. Figure 5.7 (c) shows the calculated Fermi surfaces (FSs) of $Ba_{0.7}K_{0.3}Zn_2As_2$. There are two hole pockets around the Γ point, a corrugated hole cylinder located at the zone center, and an electron pocket around the Z point. The three hole-like dispersions around the Γ point and hole-like dispersion around

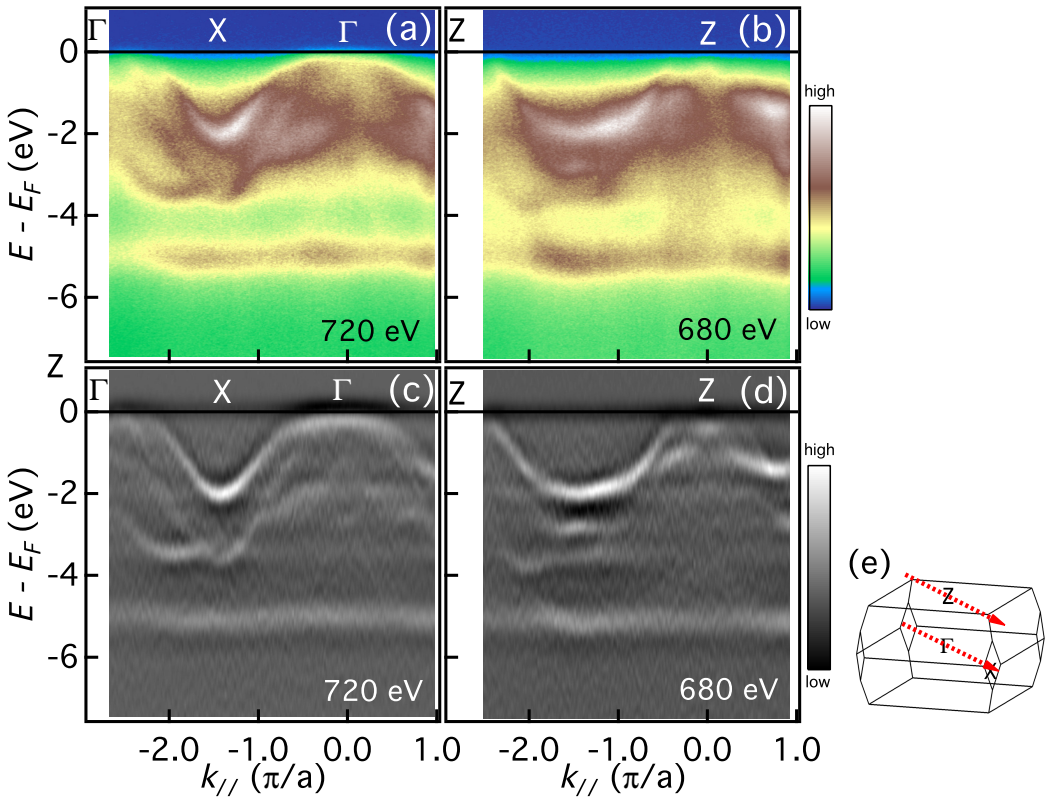

Figure 5.6: (a), (b) Soft x-ray angle-resolved photoemission spectroscopy (ARPES) intensity taken with $h\nu = 720$ and 680 eV photons . (c), (d) Corresponding second derivatives with respect to energy. (e) The first Brillouin zone. The momentum cuts are shown by arrows.

the Z point observed by ARPES can be assigned to the calculated three hole FSs. The Fermi momenta (k_F's) in units of π/a are 0.6 (outer), 0.50 (middle) and 0.26 (inner) around the Γ point, and 0.33 around the Z point, respectively, as shown by the arrows in Fig. 5.7 (a) and (b). k_F's in the outer two bands around the Γ point are estimated by linear extrapolation of the band dispersions. While we cannot clearly resolve the tiny electron pocket around the Z point, the slightly enhanced intensity at $E = 0$, $k_{\|} = 0$ suggests the presence of an electron pocket. The presence of FSs in the host material is contrasted with GaMnAs, where no clear Fermi surface crossing has been observed [151].

Constant energy mapping at E_F is shown in Fig. 5.8. To obtain the mapping, ARPES intensity within the energy window of $\Delta E = \pm 250$ meV has been integrated. Mapping at $h\nu = 600$ eV corresponds to the $k_z = 27.3$ $(2\pi/c)$ plane as illustrated in the right. Strong intensities appear around (0, 0) and $(2\pi, 0)$, consistent with the calculated FSs located at the zone center.

In order to extract information about the Mn $3d$ impurity levels as we have done

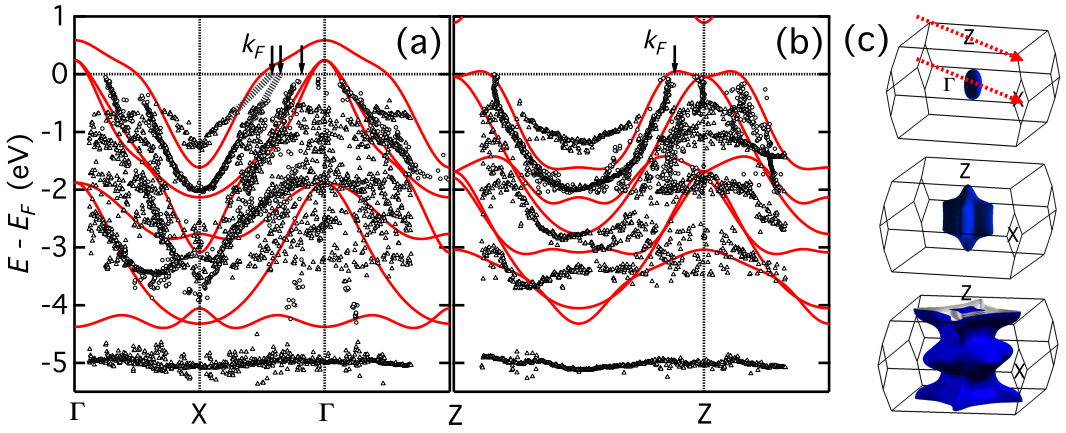

Figure 5.7: (a), (b) Comparison of the peak positions between the ARPES data and density-functional-theory band dispersion of the host material $Ba_{0.7}K_{0.3}Zn_2As_2$. Cuts are the same as those in Fig. 5.6. The peak positions have been determined by fitting the energy distribution curves (triangles) and momentum distribution curves (circles) to Lorentzian functions convoluted with the instrumental Gaussian function. Arrows indicate experimental Fermi wave vectors (k_F's) of the hole bands that form Fermi surfaces (FSs). The k_F's of outer two bands in panel (a) is determined by linear extrapolation of the peaks to the Fermi level. (c) Calculated FSs. Top: Hole FS, Middle: Hole FS, Bottom: Hole FS centered at the Γ point and electron FS centered at the Z point.

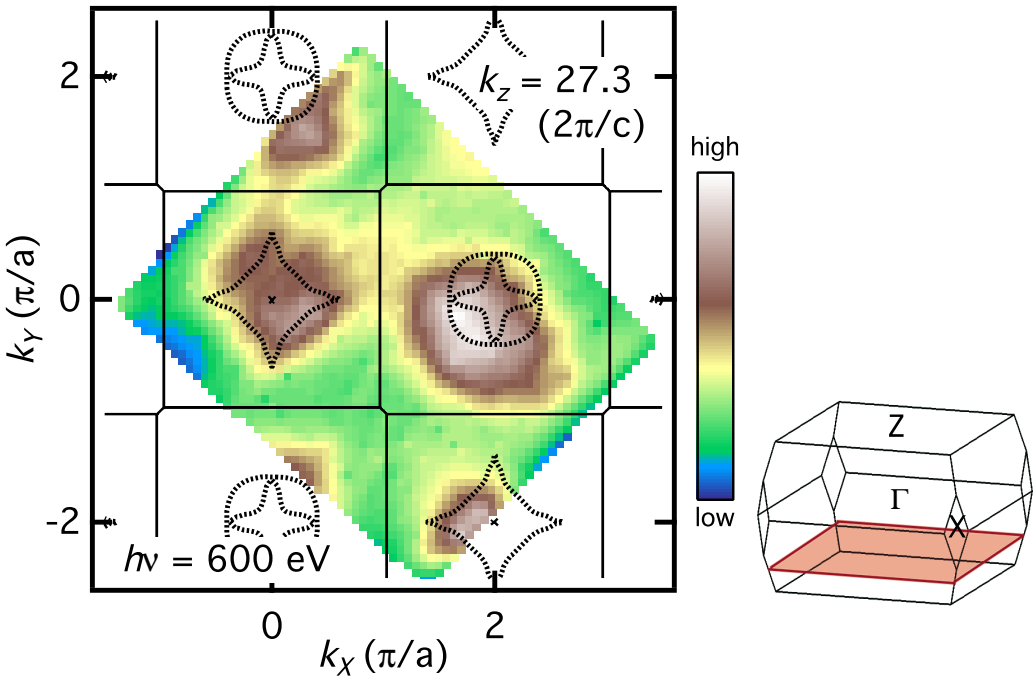

Figure 5.8: Photoemission intensity integrated within the energy window of $\Delta E = \pm 250$ meV for the $k_z = 27.3$ $(2\pi/c)$ plane. Dotted lines show the calculated FSs.

for polycrystals, we performed resonance ARPES measurements around the Mn L_3-edge. From the XAS spectra shown in Fig. 5.9 (a), we determined the on- and off-resonance energies to be 637 eV and 640 eV, respectively. ARPES spectra taken with these energies are shown in Figs. 5.9 (b) and (c). The change in these spectra enables us to clearly identify the resonance enhancement of Mn $3d$-related photoemission features around -3.5 eV. From the color plot we observe enhanced nondispersive intensity due to the Mn $3d$ states overlaid on the the host bands, which are barely seen due to the overwhelmingly strong Mn $3d$-related features. The strongest intensity enhancement around -3.5 eV corresponds to the main DOS of the Mn $3d$ PDOS, as we have observed for the polycrystals.

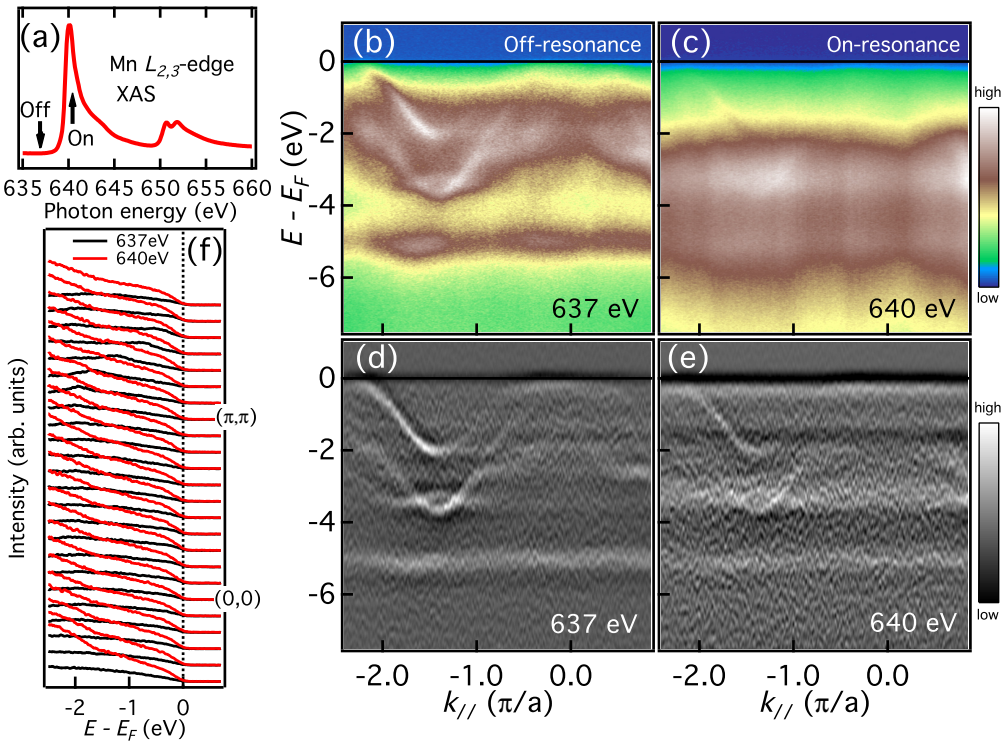

Figure 5.9: (a) Mn $L_{2,3}$-edge x-ray absorption spectrum of Mn-$BaZn_2As_2$. Off- and on-resonance photon energies are chosen to be 637 eV and 640 eV, respectively. (b), (c) ARPES energy-momentum intensity taken with on- and off-resonance energy photons. (e), (f) Second derivatives of the on- and off-resonance ARPES spectra. (f) Energy distribution curves of on- (red) and off- (black) resonance ARPES spectra.

In order to further clarify the Mn $3d$-derived states near E_F, we plot in Figs. 5.9 (d) and (e) the second derivatives of the on- and off-resonance ARPES spectra and compare the corresponding EDCs in Fig. 5.9 (f). By comparing panels (d) and (e), one finds that a nondispersive feature appears slightly below E_F ($\sim$ 0.3 eV) for all momenta. The EDCs taken on resonance [Fig. 5.9 (f)] prove that the near-

E_F feature does not originate from the Fermi cutoff but from non-dispersive states located slightly below E_F, and the increase of the second derivative is due to the bending of DOS at -0.3 eV. This nondispersive DOS continues to slowly increase down to -2 eV, and starts to rise faster as it approaches the main Mn 3d PDOS. A dispersionless impurity state below E_F has also been found in a resonance SX ARPES study of GaMnAs [151], where Mn $3d$-derived impurity band hybridized with the light-hole band of the host GaAs has been identified. Note that the impurity band is located deep in the valence bands in Mn-$BaZn_2As_2$, while it is located near the valence-band maximum (VBM) and is almost split off from it in GaMnAs. In addition, while the nondispersive intensity enhancement in GaMnAs is slightly peaked below E_F [151], the enhancement in Mn-$BaZn_2As_2$ is not peaked but shows a gradual increase. This difference may originate from the weaker hybridization between the Mn $3d$ and As $4p$ orbitals in Mn-$BaZn_2As_2$ than in GaMnAs, as we have seen in the XAS spectra (Fig. 5.2).

Now we discuss possible origins of the impurity bands in the Mn-doped DMSs. While Mn-$BaZn_2As_2$ and GaMnAs are shown to have "impurity bands", it has been reported that impurity band is absent in another p-type DMS $In_{1-x}Mn_xAs$ (InMnAs) [152]. The highest T_C's so far reported are 230 K for Mn-$BaZn_2As_2$ [85], 185 K for GaMnAs [63], and 55 K for InMnAs [62]. In InMnAs, free carriers rather than carriers in the impurity band explain the existence of the Drude component in the optical conductivity [153, 154]. In Ref. 152, the origin of the absence of impurity band is attributed to the weaker hybridization between the Mn $3d$ orbitals and the $4p$ orbitals of As ligands due to longer Mn-As distance than GaMnAs. The present observation of the impurity band in Mn-$BaZn_2As_2$ corroborates the importance of the strong hybridization for the emergence of impurity levels and the high-T_C carrier-induced ferromagnetism. Note that the metallic transport in Mn-$BaZn_2As_2$ is caused by the multiple host bands crossing E_F, whereas the VBM of GaMnAs is located below E_F and the Mn $3d$ impurity band is responsible for metallic transport in GaMnAs. These observations suggest that, in spite of the different nature of carriers which mediate magnetic interactions between the Mn spins, ferromagnetism is induced as long as the Mn $3d$-As $4p$ hybridization is strong enough.

Here we discuss the relationship between the present results and the recent theoretical study by Glasbrenner *et al.* [155]. First, the supercell calculation in Ref. 155 shows that the main Mn $3d$ PDOS in $Ba(Zn_{0.875}Mn_{0.125})_2As_2$ is located at $\sim$ -3.4 eV and its width is less than 1 eV. While the peak position is consistent with our observations, the width is underestimated as compared with the wide Mn $3d$ PDOS [150]. Second, the calculation predicts the emergence of an $\uparrow$ band as a result of hybridization between the As $4p$ and the narrow Mn $3d$ band and the $\uparrow$ band disperses from the original Mn $3d$ $\uparrow$ level toward E_F and above. However, in our experiment, the Mn $3d$-related spectral weight is broad and nondispersive up to E_F.

This may reflect the strong local electron correlations among the Mn $3d$ electrons and the randomness of the Mn atoms substituting the Zn sites. As for the reduction of the saturated magnetic moment of Mn from 5 μ_B expected from the high-spin configuration of Mn $3d$ electrons to $\sim$1 μ_B, it can be explained by the competition between the antiferromagnetic (AFM) superexchange coupling between the nearest-neighbor Mn spins and the longer-range FM coupling between them mediated by As holes as described in Ref. 155. Indeed, the end material $BaMn_2As_2$ is an AFM insulator with a high Néel temperature (T_N) of 625 K and the hole-doped metallic system $Ba_{1-x}K_xMn_2As_2$ remains AFM with a slight reduction of T_N (480 K for x $\sim$ 0.4) [156]. In order to achieve ferromagnetism, therefore, the average Mn-Mn distance must be sufficiently elongated and the AFM interaction strength must be reduced as in the present dilute Mn case. Interestingly, it has been reported that the As $4p$ conduction band in $Ba_{1-x}K_xMn_2As_2$ shows itinerant ferromagnetism and coexists with the Mn AFM order [157, 158]. It is, therefore, natually expected that such an unconventional magnetic state, in which FM and AFM interactions coexist and compete with each other, can exist in Mn-$BaZn_2As_2$ as well.

5.7 X-ray magnetic circular dichroism

In order to investigate the ferromagnetic ordering of Mn spins, we performed XMCD measurements on Mn-$BaZn_2As_2$ single crystals. Figure 5.10 (a) shows the Mn $L_{2,3}$-edge XAS spectra of Mn-$BaZn_2As_2$. Magnetic fields of $\pm$ 1 T were applied along the c-axis. The single peak structure of the L_3 main peak evidences that Mn-$BaZn_2As_2$ does not contain extrinsic Mn components such as oxidized Mn atoms at the surface unlike in the case of GaMnAs [138]. The XMCD spectrum defined as the difference between the XAS spectra taken with positive and negative magnetic fields is shown in Fig. 5.10 (b). From the experimental XMCD spectra we have determined the spin and orbital magnetic moments separately by applying the XMCD sum rule [159, 160]. The $3d$ electron occupation number appearing in the sum rule was set to 5. The estimated spin and orbital magnetic moments are respectively m_{spin}= 0.45 μ_{B} and m_{orb}= 0.05 μ_{B}. We attribute the small spin moment compared with 5 μ_{B}, the value expected for Mn^{2+} (d^5), to a competition between the antiferromagnetic superexchange interaction for the nearest-neighbor Mn atoms and ferromagnetic (FM) interaction through long-range coupling mediated by the itinerant carriers. A theoretical work predicts that the effective exchange coupling J_H^{eff} between Mn pairs changes sign from antiferromagnetic (AFM) to FM when they are separated by more than 3 Å for hole-doped cases $x = 0.2$ and 0.4 [155]. Indeed, the end compound $BaMn_2As_2$ is a local-moment AFM insulator with the extraordinarily high Néel temperature of $T_N = 625$ K, and the AFM order remains robust in the hole-doped system $Ba_{1-x}K_xMn_2As_2$ up to $x = 0.40$ [156]. The XMCD mag-

netic moments are smaller than the total magnetic moment of $\sim 0.8\ \mu_B$ estimated from SQUID magnetometry [130]. The almost quenched orbital magnetic moment reaffirms the $S = 5/2$ high spin configuration of Mn $3d$ electrons, and the nonzero value reflects the finite contribution of the charge-transfered states to the ground state.

5.8 Resonant inelastic x-ray scattering

Finally we investigate the electronic excitations of Mn by RIXS measurement. Figure 5.11 (a) shows the experimental setup of the RIXS experiment. The detector angle 2θ is fixed at 90° throughout this work, and the polarization of incident photons was kept either within or perpendicular to the scattering plane (referred to as π and σ scattering geometries, respectively). The momentum transfer $\boldsymbol{q}$ in the Brillouin zone of $Ba_{1-x}K_x(Zn_{1-y}Mn_y)_2As_2$ is shown in panel (b). At the Mn L_3 edge with $2\theta = 90°$ geometry, the magnitude of $\boldsymbol{q}$ was 0.602 π/a or 0.993 $2\pi/c$, where $a = 4.12$ Å and $c = 13.58$ Å are in-plane and out-of-plane lattice constants, respectively. The incident angle θ_i can be with respect to the a-b plane was varied by rotating the sample with the rotation axis perpendicular to the scattering plane. In momentum space, this corresponds to rotating the $\boldsymbol{q}$ vector within the Γ-XZ plane as illustrated in the figure. In the specular scattering geometry ($\theta_i = 45°$), the $\boldsymbol{q}$ vector nearly corresponds to the Γ-Z distance ($2\pi/c = 0.606\ \pi/a$).

Figure 5.11 (c) shows XAS spectra in the Mn $L_{2,3}$-edge region of Mn-$BaZn_2As_2$ collected in the total-fluorescence-yield mode. The L_3 edge of Mn is located at 639 eV. Figure 5.11 (d) shows RIXS spectra taken with various incident photon energies ($h\nu$) across the L_3 edge with σ polarizations. At the L_3 peak, we observed a broad feature between -6 eV and -1 eV. As we shall show below, this broad feature originates from the d-d excitation of the Mn ion. Upon detuning the photon energy from the L_3 edge toward higher energies, we observe a broad contiuous excitations that exhibit fluorescent behavior. These excitations originate from emission from the intermediate states where electrons in the As $4p$ valence band screen the Mn $2p$ core holes.

In Fig. 5.12, we compare the RIXS spectrum taken at the Mn L_3 peak and the spectra calculated for GaMnAs using the CI cluster model [161]. Calculations were performed both for the Mn^{2+} and Mn^{3+} states with parameters determined by XAS and XMCD. We observe that the broad feature originates from the d-d excitations. The d-d excitation profiles are much broader than the experimental energy resolution of 80 meV. As an origin of the broading, the fast decay of the final states can be considered, as theoretically proposed for Mn impurity in Ag [162]. Indeed, the broad d-d excitation profile has been found in GaMnAs as well [161], where the the small band gap of the host GaAs opens a decay channel for

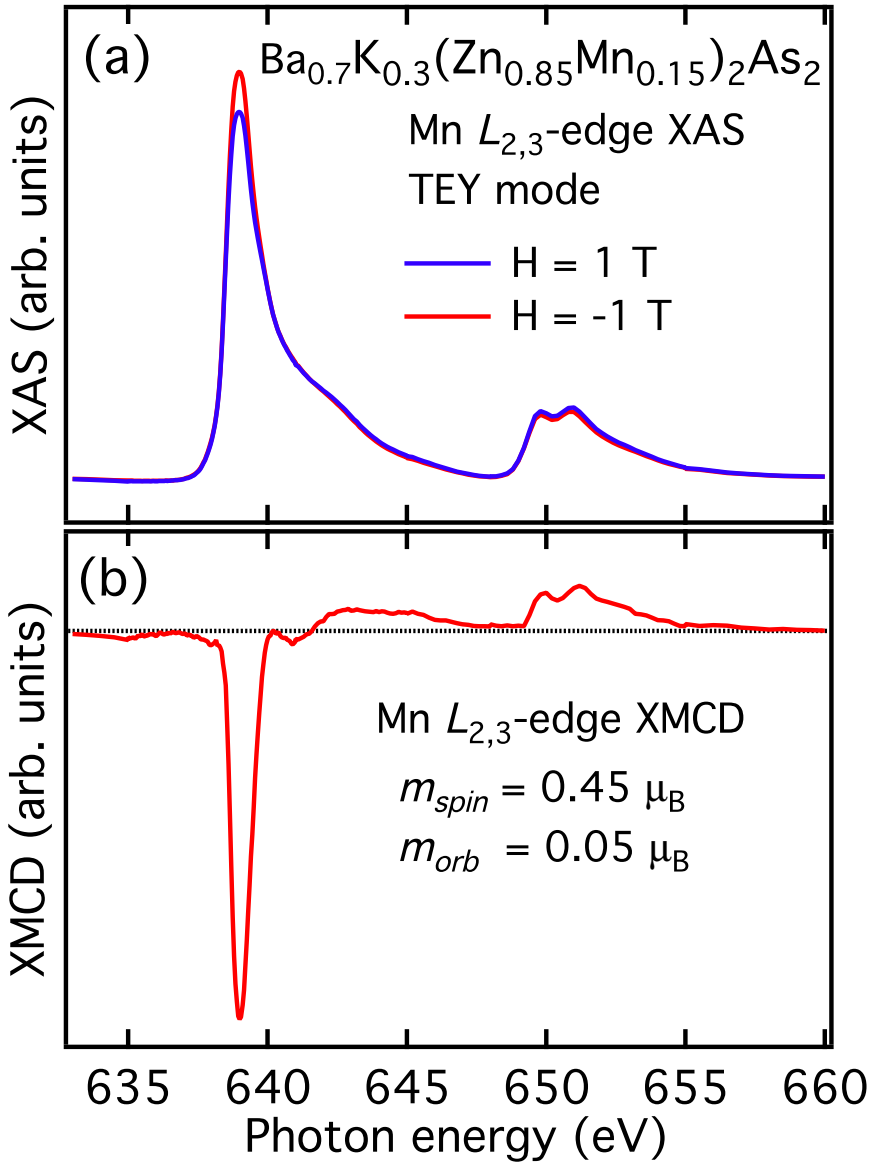

Figure 5.10: (a) X-ray absorption spectra of $Ba_{0.7}K_{0.3}(Zn_{0.85}Mn_{0.15})_2As_2$ single crystals at the Mn $L_{2,3}$ edge taken in total-electron-yield mode. Magnetic field of $\pm$ 1 T was applied along the c axis, and x-rays were incident 30° from the c-axis. (b) X-ray magnetic circular dichroism at the Mn $L_{2,3}$ edge. The spin and orbital moments are deduced to be 0.45 and 0.05 μ_B, respectively.

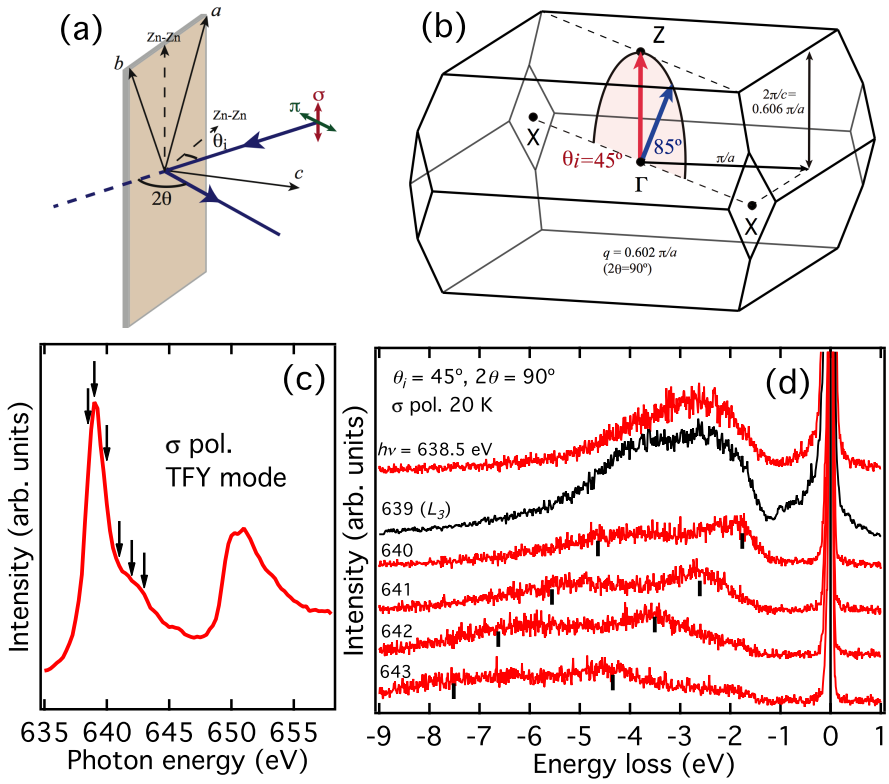

Figure 5.11: (a) Experimental setup of the resonant inelastic x-ray scattering (RIXS). (b) Momentum transfer $\boldsymbol{q}$ in the Brillouin zone of $Ba_{1-x}K_x(Zn_{1-y}Mn_y)_2As_2$. (c) XAS spectra taken in the total-fluorescence-yield mode. The photon energies employed for RIXS measurements are indicated by arrows. (d) Incident energy dependence of the RIXS spectra taken with σ polarizations. Vertical bars indicate constant emission energies characteristic of fluorescent emission.

the d-d excitations into the continuum of electron-hole pairs in the GaAs host. The same decay channel as in GaMnAs is expected to be present in Mn-$BaZn_2As_2$ and considering the narrower band gap of 0.23 eV of $BaZn_2As_2$ [134] than that (1.42 eV) of GaAs, electron-hole pair creation can be more efficient. For the peak positions of the d-d excitations, in GaMnAs, Kobayashi *et. al.* [161] found that the main loss peak at -3 eV is more prominent than other structures and concluded that the charge-transferred $3d^5\underline{L}$ state is more appropriate for the description of the Mn impurity state in GaMnAs. For Mn-$BaZn_2As_2$, on the other hand, the peaks are located at -4 and -2.5 eV, which correspond to the peaks in the calculated spectra for the Mn^{2+}, and the intensity between -4 and -2.5 eV is still high, which can be attributed to emission from the Mn^{3+} configuration as in GaMnAs. From this consideration, it can be concluded that, in Mn-$BaZn_2As_2$, both pure acceptor $3d^5$ with free holes and the $3d^5\underline{L}$ electron configuration with bound holes contribute to the ground state of Mn ions.

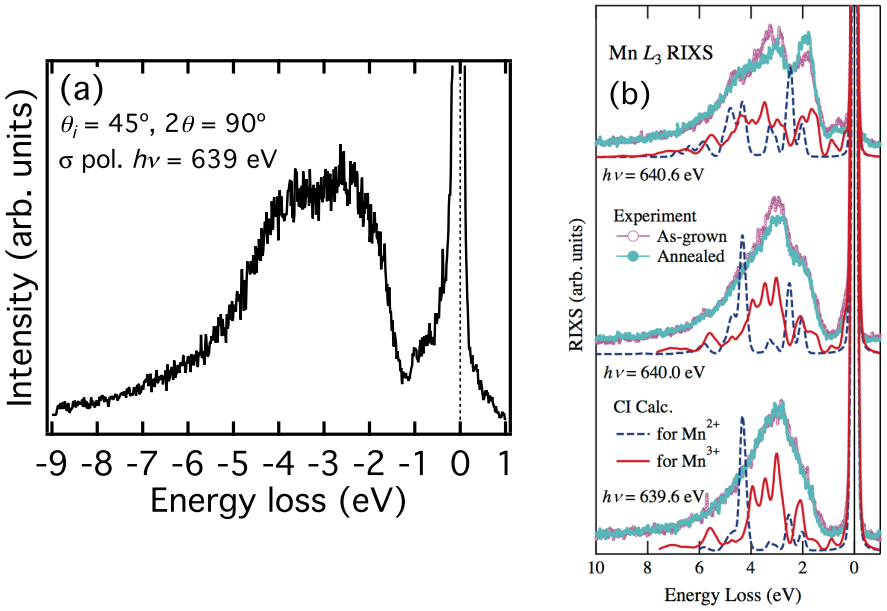

Figure 5.12: Comparison between present experiment and configuration-interaction (CI) calculation spectra for GaMnAs at the Mn L_3 edge [161]. Calculations are performed both for Mn^{2+} ($3d^5$ configuration) and for Mn^{3+} ($3d^5\underline{L}$ configuration) states.

In addition to the d-d excitation of relatively high energies primarily localized on the Mn ion, it is important to study extended and/or collective excitations in magnetic materials. In order to investigate such excitations, the momentum dependence of excitations in the lower energy region were measured with π polarization for various incident angles θ_i, as shown in Fig. 5.13 (a). The broad d-d peaks do not show momentum dispersions, as expected for local excitations. In the $2\theta = 90°$ scattering geometry, the π polarization vector of the incident light is orthogonal to the two polarization vectors of the scattered light. This condition suppresses elastic charge scattering [163] and prevents the high-energy tail of the elastic peak from obscuring low-energy excitations. Figure 5.13 (b) shows an expanded view of the low-energy part. Between -1.2 and -0.2 eV, we did not identify clear peak structures, and above -0.2 eV the tails of elastic peaks become dominant. Theoretical studies based on the p-d exchange model predict that ferromagnetic DMSs can support collective acoustic and optical spin-wave modes, and a continuum of Stoner excitations [164–166]. Their energy scales are determined by the zero-temperature spin-splitting gap $\Delta = cJ_{pd}S$ for the itinerant carriers, where c is the magnetic ion density, J_{pd} is the p-d exchange and $S = 5/2$ is the local spin. As typical parameters for GaMnAs, Ref. 165 takes $c = 1$ nm^{-3} and $J_{pd} = 0.15$ eV nm^3. Then the energy scale or the acoustic spin wave becomes $0.02\Delta \sim$10 meV, which is difficult to detect due to the presence of elastic peaks. On the other hand, the optical spin waves and Stoner excitations occur at much higher energy scales Δ ($\sim$ 0.4 eV) because the

latter corresponds to flipping a single spin in the itinerant-carriers, and this energy scale is within the reach of present measurements. The absence of clear features below -0.2 eV and $c = 2.6$ nm^{-3} for Mn-$BaZn_2As_2$ impose a constraint $J_{pd} < 0.06$ eV nm^3, which should be kept in mind in theoretical modeling. For studying this issue in more detail, low-energy RIXS measurements on GaMnAs will be desired in future works.

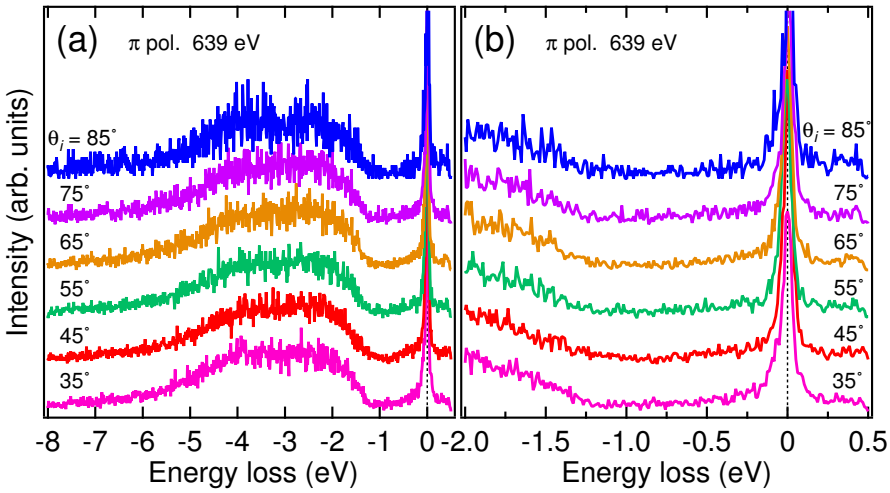

Figure 5.13: (a) RIXS spectra taken at the Mn L_3 edge with π polarizations for various incident angles θ_i. (b) Enlarged plot of the low energy-loss region.

5.9 Conclusion

In this chapter, we have studied the electronic and magnetic properties of newly synthesized DMS Mn-$BaZn_2As_2$, which is isostructural to the iron-based superconductor $BaFe_2As_2$, by soft x-ray spectroscopies. First, by using XAS and RPES techniques, we have studied the electronic structure of Mn-$BaZn_2As_2$ polycrystals, in particular that related to the Mn $3d$ states. Mn $L_{2,3}$-edge XAS spectrum indicates that the doped Mn atoms have the valence 2+ and are strongly hybridized with the As $4p$ orbitals as in archetypal DMSs GaMnAs. From the shoulder structures at $h\nu = 640$ and 643 eV, we conclude that the Mn $3d$-As $4p$ hybridization in Mn-$BaZn_2As_2$ is weaker than in GaMnAs but stronger than in GaMnN. The Mn $3d$ PDOS obtained by RPES shows a peak around $E_B = 4$ eV and is relatively high between $E_B = 0$-2 eV with little contribution at E_F. These electronic states below E_F leads to the d^5 electron configuration of Mn atoms with the local magnetic moment of $S = 5/2$. From comparison between DFT band dispersions of the host semiconductor $BaZn_2As_2$ and the experimental Mn $3d$ PDOS of Mn-$BaZn_2As_2$, we

conclude that doped holes go into the top of the As $4p$-derived valence band and are weakly bound to the Mn local spins.

Second, by using SX ARPES, we observed the valence bands of the Mn-$BaZn_2As_2$ composed mainly of As $4p$ states. Two hole pockets around the Γ point, a hole corrugated cylinder containing the Γ point, and an electron pocket around the Z point have been resolved, which give rise to the conduction in Mn-$BaZn_2As_2$. Resonance SX ARPES results suggest the presence of Mn $3d$ impurity band near E_F as in GaMnAs. However, the impurity band state in Mn-$BaZn_2As_2$ is not clearly peaked unlike in GaMnAs, probably reflecting the weaker Mn $3d$-As$4p$ hybridization. We propose that the strong hybridization between the Mn $3d$ and the As $4p$ states plays an important role in creating the impurity band and inducing high temperature ferromagnetism, but that the metallic transport can be induced either by the host valence band or the impurity band in Mn-doping based DMSs.

Third, we have probed the magnetic ground states and electronic excitations of Mn in Mn-$BaZn_2As_2$ by XMCD and RIXS. Ferromagnetic XMCD signal from the Mn L_3 edge is observed with spin moment of $0.45\mu_B$/Mn and almost quenched orbital moment $0.05\mu_B$/Mn, indicating that the Mn atoms take high-spin state of the $3d^5$ configuration with $S = 5/2$ and that there are competing ferromagnetic and antiferromagnetic interactions between the local moments. Mn L_3 edge RIXS spectra show a broad peak between 6 eV to 1 eV energy loss. From configuration-interaction cluster-model calculations, we assign it to d-d excitations from the Mn ground states. The RIXS line shape indicates that the ground state of Mn in Mn-$BaZn_2As_2$ consists not only of the charge-transferred $3d^5\underline{L}$ electron configuration with weakly bound holes but also of the pure $3d^5$ configuration with free holes. The broadness originates from the rapid decay of the d-d excitons to electron-hole pairs in the As $4p$ valence and conduction bands with a small indirect band gap of 0.3 eV.

Chapter 6

Summary and conclusion

In the present thesis, I present spectroscopic studies of 122-type iron-based superconductors and ferromagnetic diluted magnetic semiconductor $Ba_{1-x}K_x(Zn_{1-x}Mn_x)_2As_2$. Both materials belong to the $ThCr_2Si_2$-type crystal structure. In the former, superconductivity appress on FeAs layers by doping carriers or applying chemical pressure by isovalent doping. The competition between the antiferromagnetism of the parent compounds and superconductivity is analogous to the cuprates. In the latter, ferromagnetism can be achieved on the ZnAs layer by the separate doping of magnetic elements and charge carriers. The isovalent Mn^{2+} doping to the Zn^{2+} sites does not show low solubility and the independent control of charge and magnetic elements allows the high T_C of 230K. The interplay among ferromagnetism, antiferromagnetism, and superconductivity in two-dimensional electronic states in FeAs and ZnAs layers has been the central focus of the present thesis.

In Chap. 3, I presented an ARPES study of the nodal superconductor $SrFe_2(As_{1-x}P_x)_2$. Isovalent-substituted iron pnictide superconductors $SrFe_2(As_{1-x}P_x)_2$ and $BaFe_2(As_{1-x}P_x)_2$ share the almost same pnictogen heights and are both considered to have superconducting (SC) gap nodes, whereas the c-axis length is shorter in $SrFe_2(As_{1-x}P_x)_2$ than in $BaFe_2(As_{1-x}P_x)_2$. In order to investigate the effects of the shorter interlayer distance on the SC gap structures, we have measured SC gaps for $SrFe_2(As_{0.65}P_{0.35})_2$ in the three-dimensional momentum space by synchrotron and laser-based angle-resolved photoemission spectroscopy. While the three hole FSs show orbital-dependent SC gaps, the electron FSs have almost isotropic and k_z-independent SC gaps. We conclude that there exists a sign change around the Z-X line on the outer hole FS around the Z point. We also found the spectral weight of the coherence peak is largest for the inner hole FS.

In Chap. 4, ultrafast dynamics of the parent compound of the iron-based superconductors $BaFe_2As_2$ has been studied by time- and angle-resolved photoemission spectroscopy based on extreme-ultraviolet laser generated by higher harmonics from Ar gas. The band folding due to spin-density wave (SDW) order disappeared

within $\sim$ 1 ps after the arrival of 1.5 eV pump pulse, which we interpret as the melting of the SDW. The optically excited electrons above the band gap above E_F were observed at the zone center at 0.12 ps, and decay rapidly. After the fast decay of the optically excited electrons, a thermalized state appears and survives for a relatively long time. Exponential decay constants for the thermalized state to recover back to the SDW ground state are $\sim$ 0.60 ps both around the zone center and the zone corner.

In Chap. 5, we investigated the electronic structure of $Ba_{1-x}K_x(Zn_{1-x}Mn_x)_2As_2$ by XAS and RPES. Mn $L_{2,3}$-edge XAS indicates that the doped Mn atoms have the valence 2+ and strongly hybridize with the $4p$ orbitals of the tetrahedrally coordinating As ligands. The Mn $3d$ partial density of states (PDOS) obtained by RPES shows a peak around 4 eV and relatively high between 0-2 eV below the Fermi level (E_F) with little contribution at E_F, similar to that of the archetypal DMS $Ga_{1-x}Mn_xAs$. This energy level creates d^5 electron configuration with $S = 5/2$ local magnetic moments at the Mn atoms. Hole carriers induced by K substitution for Ba atoms go into the top of the As $4p$ valence band and are weakly bound to the Mn local spins.

Furthermore, we have investigated the electronic structure of $Ba_{1-x}K_x(Zn_{1-x}Mn_x)_2As_2$ single crystals by ARPES. Measurements with soft x-rays clarify the host valence-band electronic structure primarily composed of the As $4p$ states. Two hole pockets around the Γ point, a hole corrugated cylinder surrounding the Γ and Z points, and an electron pocket around the Z point are observed, and explain the metallic transport of $Ba_{1-x}K_x(Zn_{1-y}Mn_y)_2As_2$. This is contrasted with GaMnAs, where it is located above the As $4p$ valence-band maximum (VBM) and no Fermi surfaces have been clearly identified. Resonance soft x-ray ARPES measurements reveal a nondispersive (Kondo resonance-like) Mn $3d$ impurity band near the Fermi level, as in the case of GaMnAs. However, the impurity band is located well below the VBM, unlike the impurity band in GaMnAs, which is located around and above the VBM. We conclude that, while the strong hybridization between the Mn $3d$ and the As $4p$ orbitals plays an important role in creating the impurity band and inducing high temperature ferromagnetism in both systems, the metallic transport may predominantly occur in the host valence band in $Ba_{1-x}K_x(Zn_{1-y}Mn_y)_2As_2$ and in the impurity band in GaMnAs.

Finally, we have investigated the magnetic properties and electronic excitations of Mn in $Ba_{1-x}K_x(Zn_{1-y}Mn_y)_2As_2$ by XMCD and RIXS at the Mn $L_{2,3}$ edge. Ferromagnetic XMCD signals are observed with the spin moment of $0.45\mu_B$/Mn, but the nearly quenched orbital moment of $0.05\mu_B$/Mn and the line shapes indicate that the Mn atoms take the high-spin configurations of d^5, suggesting that there are competing ferromagnetic and antiferromagnetic interactions between the Mn local moments. RIXS spectra show broad peaks from 6 eV to 1 eV in energy loss which

originate from d-d orbital excitations from the ground states. From the comparison of the line shape with that of $Ga_{1-x}Mn_xAs$, we conclude that both pure acceptor $3d^5$ and charge-transferred $3d^5\underline{L}$ electron configurations constitute the ground state of Mn in $Ba_{1-x}K_x(Zn_{1-y}Mn_y)_2As_2$.

Acknowledgments

I would like to express sincere gratitude to all the people who have instructed me during my Ph. D. study.

First of all, I would like to express my sincere gratitude to my supervisor Prof. Atsushi Fujimori, who has endowed me with a lot of fruitful research projects that involve international collaborations. With his insightful advice I could learn the fundamentals of strongly-correlated electron systems and various synchrotron experimental techniques.

It was very fortunate that I could complete my degree through financial supports from Advanced Leading Graduate Course for Photon Science (ALPS) and the JSPS Research Fellowship for Young Scientists. I'm grateful to Prof. Makoto Gonokami and Prof. Junji Yumoto for instructing me the cutting-edge laser technology through ALPS program and proposing diverse career paths after Ph.D.. I also thank Prof. Tomoko Ohtsuki for giving me an internship opportunity at OFS.

For the ARPES work on $SrFe_2(As_{1-x}P_x)_2$, I'm grateful to Prof. Setsuko Tajima, Prof. Shigeki Miyasaka, and Dr. Tatsuya Kobayashi for providing us with high-quality single crystals of $SrFe_2(As_{1-x}P_x)_2$. I would also acknowledge the precious collaboration with Prof. Zhi-Xun Shen, Dr. Donghui Lu, Dr. Makoto Hashimoto and Dr. Ming Yi at SSRL.

I'm grateful to Prof. Shik Shin, Prof. Kozo Okazaki, Prof. Jiro Itatani, Dr. Masami Fujisawa, Mr. Takashi Yamamoto, Mr. Takashi Someya, Mr. Masaru Okada for allowing me to get involved in the construction of the new time-resolved ARPES apparatus and research projects at ISSP. I thank Dr. Masamichi Nakajima, Dr. Hiroshi Eisaki and Prof. Shin-ichi Uchida of AIST for providing us $BaFe_2As_2$ single crystals for the TrARPES experiments.

For the spectroscopic studies on the new ferromagnetic semiconductors, I feel obliged to Prof. Yasutomo J. Uemura of Columbia University and Prof. Changqing Jin of Chinese Academy of Sciences for giving me the research projects and supervision. I'm also thankful to Prof. Sadamichi Maekawa and Dr. Bo Gu of Japan Atomic Energy Agency for enlightening theory support and to Dr. Kan Zhao, Mr. Guoqiang Zhao and Ms. Bijuan Chen for synthesizing high-quality $Ba_{1-x}K_x(Zn_{1-y}Mn_y)_2As_2$ crystals. The XMCD and RIXS experiments have been

performed through close collaborations with Prof. Di-Jing Huang, Prof. C.-T. Chen, Dr. Jun Okamoto, Dr. W.-B. Wu, Dr. F.-H. Chang, Dr. H.-J. Lin, Mr. Z.-Y. Chen of NSRRC. For the soft x-ray ARPES experiments, I would like to thank Prof. Hiroshi Kumigashira, Prof. Koji Horiba, Dr. Masaki Kobayashi, Dr. Makoto Minohara, Dr. Enju Sakai for granting us limited beam times and their experimental support at KEK-PF.

I would like to thank all the current and former members of Fujimori group: Prof. Teppei Yoshida, Dr. Vijay Raj Singh, Dr. Shin-ichiro Ideta, Dr. Virendra Kumar Verma, Dr. Toshiharu Kadono, Dr. Enju Sakai, Dr. Kohei Yoshimatsu, Dr. Keisuke Ishigami, Mr. Yo Yamazaki, Mr. Ichiro Nishi, Dr. Leo Cristobal Ambolode II, Mr. Goro Shibata, Mr. Takayuki Harano, Mr. Yukio Takahashi, Mr. Masahumi Horio, Dr. Liang Liu, Ms. Xu Jian, Mr. Yosuke Nonaka, Mr. Keisuke Koshiishi, and Mr. Keisuke Ikeda. The international environment with different cultural/academic backgrounds has always motivated me.

I would like to thank Ms. Yuko Shimazaki, and Ms. Ami Ito for dealing with documentations and continuous encouragements during my graduate study.

Finally, I would like to thank my parents and wife for supporting the long student life and continuous encouragement.

January 2016
Hakuto Suzuki

References

[1] Y. Kamihara, T. Watanabe, M. Hirano, and H. Hosono, J. Am. Chem. Soc. **130**, 3296 (2008).

[2] J. Paglione and R. L. Greene, Nat. Phys. **6**, 645 (2010).

[3] C. de la Cruz, Q. Huang, J. W. Lynn, J. Li, W. R. II, J. L. Zarestky, H. A. Mook, G. F. Chen, J. L. Luo, N. L. Wang, and P. Dai, Nature **453**, 899 (2008).

[4] H. Luetkens, H. H. Klauss, M. Kraken, F. J. Litterst, T. Dellmann, R. Klingeler, C. Hess, R. Khasanov, A. Amato, C. Baines, M. Kosmala, O. J. Schumann, M. Braden, J. Hamann-Borrero, N. Leps, A. Kondrat, G. Behr, J. Werner, and B. Buchner, Nat. Mater. **8**, 305 (2009).

[5] S. Nandi, M. G. Kim, A. Kreyssig, R. M. Fernandes, D. K. Pratt, A. Thaler, N. Ni, S. L. Bud'ko, P. C. Canfield, J. Schmalian, R. J. McQueeney, and A. I. Goldman, Phys. Rev. Lett. **104**, 057006 (2010).

[6] C.-H. Lee, A. Iyo, H. Eisaki, H. Kito, M. T. Fernandez-Diaz, T. Ito, K. Kihou, H. Matsuhata, M. Braden, and K. Yamada, J. Phys. Soc. Jpn. **77**, 083704 (2008).

[7] D. S. Inosov, J. T. Park, P. Bourges, D. L. Sun, Y. Sidis, A. Schneidewind, K. Hradil, D. Haug, C. T. Lin, B. Keimer, and V. Hinkov, Nat. Phys. **6**, 178 (2010).

[8] I. I. Mazin, D. J. Singh, M. D. Johannes, and M. H. Du, Phys. Rev. Lett. **101**, 057003 (2008).

[9] K. Kuroki, S. Onari, R. Arita, H. Usui, Y. Tanaka, H. Kontani, and H. Aoki, Phys. Rev. Lett. **101**, 087004 (2008).

[10] T. Takimoto, T. Hotta, T. Maehira, and K. Ueda, J. Phys. Condens. Matter **14**, L369 (2002).

[11] K. Kuroki, H. Usui, S. Onari, R. Arita, and H. Aoki, Phys. Rev. B **79**, 224511 (2009).

[12] T. Shibauchi, A. Carrington, and Y. Matsuda, Annu. Rev. Condens. Matter Phys. **5**, 113 (2014).

[13] T. Kobayashi, S. Miyasaka, and S. Tajima, J. Phys. Soc. Jpn. **81SB**, SB045 (2012).

[14] S. Onari and H. Kontani, Phys. Rev. Lett. **103**, 177001 (2009).

[15] P. J. Hirschfeld, M. M. Korshunov, and I. I. Mazin, Rep. Prog. Phys. **74**, 124508 (2011).

[16] M. Sato, Y. Kobayashi, S. C. Lee, H. Takahashi, E. Satomi, and Y. Miura, J. Phys. Soc. Jpn. **79**, 014710 (2010).

[17] H. Kontani and S. Onari, Phys. Rev. Lett. **104**, 157001 (2010).

[18] M. Yoshizawa, D. Kimura, T. Chiba, S. Simayi, Y. Nakanishi, K. Kihou, C.-H. Lee, A. Iyo, H. Eisaki, M. Nakajima, and S. ichi Uchida, J. Phys. Soc. Jpn. **81**, 024604 (2012).

[19] S. Onari and H. Kontani, Phys. Rev. Lett. **109**, 137001 (2012).

[20] S. Kasahara, T. Shibauchi, K. Hashimoto, K. Ikada, S. Tonegawa, R. Okazaki, H. Shishido, H. Ikeda, H. Takeya, K. Hirata, T. Terashima, and Y. Matsuda, Phys. Rev. B **81**, 184519 (2010).

[21] T. Kobayashi, S. Miyasaka, S. Tajima, and N. Chikumoto, J. Phys. Soc. Jpn. **83**, 104702 (2014).

[22] M. Nakajima, S. Uchida, K. Kihou, C.-H. Lee, A. Iyo, and H. Eisaki, J. Phys. Soc. Jpn. **81**, 104710 (2012).

[23] T. Dulguun, H. Mukuda, T. Kobayashi, F. Engetsu, H. Kinouchi, M. Yashima, Y. Kitaoka, S. Miyasaka, and S. Tajima, Phys. Rev. B **85**, 144515 (2012).

[24] T. Kobayashi, S. Miyasaka, S. Tajima, T. Nakano, Y. Nozue, N. Chikumoto, H. Nakao, R. Kumai, and Y. Murakami, Phys. Rev. B **87**, 174520 (2013).

[25] T. Yoshida, I. Nishi, S. Ideta, A. Fujimori, M. Kubota, K. Ono, S. Kasahara, T. Shibauchi, T. Terashima, Y. Matsuda, H. Ikeda, and R. Arita, Phys. Rev. Lett. **106**, 117001 (2011).

[26] H. Suzuki, T. Kobayashi, S. Miyasaka, T. Yoshida, K. Okazaki, L. C. C. Ambolode, S. Ideta, M. Yi, M. Hashimoto, D. H. Lu, Z.-X. Shen, K. Ono, H. Kumigashira, S. Tajima, and A. Fujimori, Phys. Rev. B **89**, 184513 (2014).

[27] K. Hashimoto, M. Yamashita, S. Kasahara, Y. Senshu, N. Nakata, S. Tonegawa, K. Ikada, A. Serafin, A. Carrington, T. Terashima, H. Ikeda, T. Shibauchi, and Y. Matsuda, Phys. Rev. B **81**, 220501 (2010).

[28] K. Hashimoto, T. Shibauchi, S. Kasahara, K. Ikada, S. Tonegawa, T. Kato, R. Okazaki, C. J. van der Beek, M. Konczykowski, H. Takeya, K. Hirata, T. Terashima, and Y. Matsuda, Phys. Rev. Lett. **102**, 207001 (2009).

[29] P. J. Hirschfeld and N. Goldenfeld, Phys. Rev. B **48**, 4219 (1993).

[30] J. Murphy, C. P. Strehlow, K. Cho, M. A. Tanatar, N. Salovich, R. W. Giannetta, T. Kobayashi, S. Miyasaka, S. Tajima, and R. Prozorov, Phys. Rev. B **87**, 140505 (2013).

[31] Y. Nakai, T. Iye, S. Kitagawa, K. Ishida, S. Kasahara, T. Shibauchi, Y. Matsuda, and T. Terashima, Phys. Rev. B **81**, 020503 (2010).

[32] M. Yashima, H. Nishimura, H. Mukuda, Y. Kitaoka, K. Miyazawa, P. M. Shirage, K. Kihou, H. Kito, H. Eisaki, and A. Iyo, J. Phys. Soc. Jpn. **78**, 103702 (2009).

[33] M. Miyamoto, H. Mukuda, T. Kobayashi, M. Yashima, Y. Kitaoka, S. Miyasaka, and S. Tajima, Phys. Rev. B **92**, 125154 (2015).

[34] M. Yamashita, Y. Senshu, T. Shibauchi, S. Kasahara, K. Hashimoto, D. Watanabe, H. Ikeda, T. Terashima, I. Vekhter, A. B. Vorontsov, and Y. Matsuda, Phys. Rev. B **84**, 060507 (2011).

[35] T. Shimojima, F. Sakaguchi, K. Ishizaka, Y. Ishida, T. Kiss, M. Okawa, T. Togashi, C.-T. Chen, S. Watanabe, M. Arita, K. Shimada, H. Namatame, M. Taniguchi, K. Ohgushi, S. Kasahara, T. Terashima, T. Shibauchi, Y. Matsuda, A. Chainani, and S. Shin, Science **332**, 564 (2011).

[36] Y. Zhang, Z. R. Ye, Q. Q. Ge, F. Chen, J. Jiang, M. Xu, B. P. Xie, and D. L. Feng, Nat. Phys. **8**, 371 (2012).

[37] T. Yoshida, S. Ideta, T. Shimojima, W. Malaeb, K. Shinada, H. Suzuki, I. Nishi, A. Fujimori, K. Ishizaka, S. Shin, Y. Nakashima, H. Anzai, M. Arita, A. Ino, H. Namatame, M. Taniguchi, H. Kumigashira, K. Ono, S. Kasahara, T. Shibauchi, T. Terashima, Y. Matsuda, M. Nakajima, S. Uchida, Y. Tomioka, T. Ito, K. Kihou, C. H. Lee, A. Iyo, H. Eisaki, H. Ikeda, R. Arita, T. Saito, S. Onari, and H. Kontani, Sci. Rep. **4**, 7292 (2014).

[38] K. Suzuki, H. Usui, and K. Kuroki, J. Phys. Soc. Jpn. **80**, 013710 (2011).

[39] T. Saito, S. Onari, and H. Kontani, Phys. Rev. B **88**, 045115 (2013).

[40] L. Chauvière, Y. Gallais, M. Cazayous, A. Sacuto, M. A. Méasson, D. Colson, and A. Forget, Phys. Rev. B **80**, 094504 (2009).

[41] M. Zbiri, H. Schober, M. R. Johnson, S. Rols, R. Mittal, Y. Su, M. Rotter, and D. Johrendt, Phys. Rev. B **79**, 064511 (2009).

[42] D. H. Torchinsky, G. F. Chen, J. L. Luo, N. L. Wang, and N. Gedik, Phys. Rev. Lett. **105**, 027005 (2010).

[43] B. Mansart, D. Boschetto, A. Savoia, F. Rullier-Albenque, A. Forget, D. Colson, A. Rousse, and M. Marsi, Phys. Rev. B **80**, 172504 (2009).

[44] L. Rettig, R. Cortés, S. Thirupathaiah, P. Gegenwart, H. S. Jeevan, M. Wolf, J. Fink, and U. Bovensiepen, Phys. Rev. Lett. **108**, 097002 (2012).

[45] I. Avigo, R. Cortés, L. Rettig, S. Thirupathaiah, H. S. Jeevan, P. Gegenwart, T. Wolf, M. Ligges, M. Wolf, J. Fink, and U. Bovensiepen, J. Phys. Condens. Matter **25**, 094003 (2013).

[46] X. Yang, L. G. Rohde, T. Rohwer, A. Stange, K. Hanff, C. Sohrt, L. Rettig, R. Cortés, F. Chen, L. Feng, D. T. Wolf, B. Kamble, I. Eremin, T. Popmintchev, M. Murnane, M. C. Kapteyn, H. L. Kipp, J. Fink, M. Bauer, U. Bovensiepen, and K. Rossnagel, Phys. Rev. Lett. **112**, 207001 (2014).

[47] L. Rettig, O. Mariager, S. A. Ferrer, S. Grübel, A. Johnson, J. J. Rittmann, T. Wolf, L. Johnson, S. G. Ingold, P. Beaud, and U. Staub, Phys. Rev. Lett. **114**, 067402 (2015).

[48] H. J. Zeiger, J. Vidal, T. K. Cheng, E. P. Ippen, G. Dresselhaus, and M. S. Dresselhaus, Phys. Rev. B **45**, 768 (1992).

[49] S. Gerber, K. W. Kim, Y. Zhang, D. Zhu, N. Plonka, M. Yi, G. L. Dakovski, D. Leuenberger, P. S. Kirchmann, R. G. Moore, M. Chollet, J. M. Glownia, Y. Feng, J. S. Lee, A. Mehta, A. F. Kemper, T. Wolf, Y. D. Chuang, Z. Hussain, C. C. Kao, B. Moritz, Z. X. Shen, T. P. Devereaux, and W. S. Lee, Nat. Commun. **6**, 7377 (2015).

[50] P. B. Allen, Phys. Rev. Lett. **59**, 1460 (1987).

[51] L. Perfetti, P. A. Loukakos, M. Lisowski, U. Bovensiepen, H. Eisaki, and M. Wolf, Phys. Rev. Lett. **99**, 197001 (2007).

[52] I. Žutić, J. Fabian, and S. Das Sarma, Rev. Mod. Phys. **76**, 323 (2004).

[53] H. Ohno, Science **281**, 951 (1998).

[54] T. Dietl, H. Ohno, F. Matsukura, J. Cibert, and D. Ferrand, Science **287**, 1019 (2000).

[55] T. Dietl and H. Ohno, Rev. Mod. Phys. **86**, 187 (2014).

[56] T. Dietl, Nat. Mater. **9**, 965 (2010).

[57] J. M. D. Coey, M. Venkatesan, and C. B. Fitzgerald, Nat. Mater. **4**, 173 (2005).

[58] A. Haury, A. Wasiela, A. Arnoult, J. Cibert, S. Tatarenko, T. Dietl, and Y. Merle d'Aubigné, Phys. Rev. Lett. **79**, 511 (1997).

[59] D. Ferrand, J. Cibert, A. Wasiela, C. Bourgognon, S. Tatarenko, G. Fishman, T. Andrearczyk, J. Jaroszyński, S. Koleśnik, T. Dietl, B. Barbara, and D. Dufeu, Phys. Rev. B **63**, 085201 (2001).

[60] H. Saito, V. Zayets, S. Yamagata, and K. Ando, Phys. Rev. Lett. **90**, 207202 (2003).

[61] T. Story, R. R. Gałązka, R. B. Frankel, and P. A. Wolff, Phys. Rev. Lett. **56**, 777 (1986).

[62] T. Slupinski, H. Munekata, and A. Oiwa, J. Cryst. Growth **237**, 1331 (2002).

[63] M. Wang, R. P. Campion, A. W. Rushforth, K. W. Edmonds, C. T. Foxon, and B. L. Gallagher, Appl. Phys. Lett. **93**, 132103 (2008).

[64] S. Sonoda, S. Shimizu, T. Sasaki, Y. Yamamoto, and H. Hori, J. Cryst. Growth **237**, 1358 (2002).

[65] S. E. Park, H.-J. Lee, Y. C. Cho, S.-Y. Jeong, C. R. Cho, and S. Cho, Appl. Phys. Lett. **80**, 4187 (2002).

[66] N. Theodoropoulou, A. F. Hebard, M. E. Overberg, C. R. Abernathy, S. J. Pearton, S. N. G. Chu, and R. G. Wilson, Phys. Rev. Lett. **89**, 107203 (2002).

[67] X. Chen, M. Na, M. Cheon, S. Wang, H. Luo, B. D. McCombe, X. Liu, Y. Sasaki, T. Wojtowicz, J. K. Furdyna, S. J. Potashnik, and P. Schiffer, Appl. Phys. Lett. **81**, 511 (2002).

[68] Y. D. Park, A. T. Hanbicki, S. C. Erwin, C. S. Hellberg, J. M. Sullivan, J. E. Mattson, T. F. Ambrose, A. Wilson, G. Spanos, and B. T. Jonker, Science **295**, 651 (2002).

[69] Y. Shuto, M. Tanaka, and S. Sugahara, Appl. Phys. Lett. **90**, 132512 (2007).

[70] Y. Matsumoto, M. Murakami, T. Shono, T. Hasegawa, T. Fukumura, M. Kawasaki, P. Ahmet, T. Chikyow, S.-y. Koshihara, and H. Koinuma, Science **291**, 854 (2001).

[71] P. Sharma, A. Gupta, K. V. Rao, F. J. Owens, R. Sharma, R. Ahuja, J. M. O. Guillen, B. Johansson, and G. A. Gehring, Nat. Mater. **2**, 673 (2003).

[72] S. B. Ogale, R. J. Choudhary, J. P. Buban, S. E. Lofland, S. R. Shinde, S. N. Kale, V. N. Kulkarni, J. Higgins, C. Lanci, J. R. Simpson, N. D. Browning, S. Das Sarma, H. D. Drew, R. L. Greene, and T. Venkatesan, Phys. Rev. Lett. **91**, 077205 (2003).

[73] J. M. D. Coey, A. P. Douvalis, C. B. Fitzgerald, and M. Venkatesan, Appl. Phys. Lett. **84**, 1332 (2004).

[74] J. Philip, A. Punnoose, B. I. Kim, K. M. Reddy, S. Layne, J. O. Holmes, B. Satpati, P. R. LeClair, T. S. Santos, and J. S. Moodera, Nat. Mater. **5**, 298 (2006).

[75] H. Ohno, A. Shen, F. Matsukura, A. Oiwa, A. Endo, S. Katsumoto, and Y. Iye, Appl. Phys. Lett. **69**, 363 (1996).

[76] F. Matsukura, H. Ohno, A. Shen, and Y. Sugawara, Phys. Rev. B **57**, R2037 (1998).

[77] C. Zener, Phys. Rev. **81**, 440 (1951).

[78] C. Zener, Phys. Rev. **82**, 403 (1951).

[79] T. Dietl, A. Haury, and Y. Merle d'Aubigné, Phys. Rev. B **55**, R3347 (1997).

[80] A. Kaminski and S. Das Sarma, Phys. Rev. Lett. **88**, 247202 (2002).

[81] J. Mašek, J. Kudrnovský, F. Máca, B. L. Gallagher, R. P. Campion, D. H. Gregory, and T. Jungwirth, Phys. Rev. Lett. **98**, 067202 (2007).

[82] Z. Deng, C. Q. Jin, Q. Q. Liu, X. C. Wang, J. L. Zhu, S. M. Feng, L. C. Chen, R. C. Yu, C. Arguello, T. Goko, F. Ning, J. Zhang, Y. Wang, A. A. Aczel, T. Munsie, T. J. Williams, G. M. Luke, T. Kakeshita, S. Uchida, W. Higemoto, T. U. Ito, B. Gu, S. Maekawa, G. D. Morris, and Y. J. Uemura, Nat. Commun. **2**, 422 (2011).

[83] Z. Deng, K. Zhao, B. Gu, W. Han, J. L. Zhu, X. C. Wang, X. Li, Q. Q. Liu, R. C. Yu, T. Goko, B. Frandsen, L. Liu, J. Zhang, Y. Wang, F. L. Ning, S. Maekawa, Y. J. Uemura, and C. Q. Jin, Phys. Rev. B **88**, 081203 (2013).

[84] K. Zhao, Z. Deng, X. C. Wang, W. Han, J. L. Zhu, X. Li, Q. Q. Liu, R. C. Yu, T. Goko, B. Frandsen, L. Liu, F. Ning, Y. J. Uemura, H. Dabkowska, G. M. Luke, H. Luetkens, E. Morenzoni, S. R. Dunsiger, A. Senyshyn, P. Bni, and C. Q. Jin, Nat. Commun. **4**, 1442 (2013).

[85] K. Zhao, B. Chen, G. Zhao, Z. Yuan, Q. Liu, Z. Deng, J. Zhu, and C. Jin, Chin. Sci. Bull. **59**, 2524 (2014).

[86] Z. Xiao, F.-Y. Ran, H. Hiramatsu, S. Matsuishi, H. Hosono, and T. Kamiya, Thin Solid Films **559**, 100 (2014).

[87] J. Lu, H. Man, C. Ding, Q. Wang, B. Yu, S. Guo, H. Wang, B. Chen, W. Han, C. Jin, Y. J. Uemura, and F. Ning, Europhys. Lett. **103**, 67011 (2013).

[88] S. Hüfner, *Photoelectron Spectroscopy: Principles and Applications* (Springer, Berlin, 2003).

[89] A. Damascelli, Z. Hussain, and Z.-X. Shen, Rev. Mod. Phys. **75**, 473 (2003).

[90] A. Abrikosov, L. Gorkov, and I. Dzyaloshinski, *Methods of quantum field theory in statistical physics* (Dover Publications, New York, 1975).

[91] J. J. Sakurai, *Modern Quantum Mechanics* (Addison Wesley, Boston, 1995).

[92] U. Fano, Phys. Rev. **124**, 1866 (1961).

[93] Y. Ishida, T. Togashi, K. Yamamoto, M. Tanaka, T. Taniuchi, T. Kiss, M. Nakajima, T. Suemoto, and S. Shin, Sci. Rep. **1**, (2011).

[94] M. Fujita, H. Hiraka, M. Matsuda, M. Matsuura, J. M. Tranquada, S. Wakimoto, G. Xu, and K. Yamada, J. Phys. Soc. Jpn. **81**, 011007 (2012).

[95] A. Kotani and S. Shin, Rev. Mod. Phys. **73**, 203 (2001).

[96] L. J. P. Ament, M. van Veenendaal, T. P. Devereaux, J. P. Hill, and J. van den Brink, Rev. Mod. Phys. **83**, 705 (2011).

[97] C. H. Lai, H. S. Fung, W. B. Wu, H. Y. Huang, H. W. Fu, S. W. Lin, S. W. Huang, C. C. Chiu, D. J. Wang, L. J. Huang, T. C. Tseng, S. C. Chung, C. T. Chen, and D. J. Huang, J. Synchrotron Radiat. **21**, 325 (2014).

[98] P. Blaha, K. Schwarz, G. K. H. Madsen, D. Kvasnicka, and J. Luitz, *WIEN2K, An Augmented Plane Wave + Local Orbitals Program for Calculating Crystal Properties* (Technische Universität Wien, Wien, Austria, 2001).

[99] A. Chubukov, Annual Review of Condensed Matter Physics **3**, 57 (2012).

[100] D. J. Scalapino, Rev. Mod. Phys. **84**, 1383 (2012).

[101] R. Thomale, C. Platt, W. Hanke, J. Hu, and B. A. Bernevig, Phys. Rev. Lett. **107**, 117001 (2011).

[102] D. Scalapino, Phys. Rep. **250**, 329 (1995).

[103] M. Khodas and A. V. Chubukov, Phys. Rev. B **86**, 144519 (2012).

[104] M. R. Norman, H. Ding, M. Randeria, J. C. Campuzano, T. Yokoya, T. Takeuchi, T. Takahashi, T. Mochiku, K. Kadowaki, P. Guptasarma, and D. G. Hinks, Nature **392**, 157 (1998).

[105] M. R. Norman, M. Randeria, H. Ding, and J. C. Campuzano, Phys. Rev. B **57**, R11093 (1998).

[106] D. L. Feng, D. H. Lu, K. M. Shen, C. Kim, H. Eisaki, A. Damascelli, R. Yoshizaki, J.-i. Shimoyama, K. Kishio, G. D. Gu, S. Oh, A. Andrus, J. O'Donnell, J. N. Eckstein, and Z.-X. Shen, Science **289**, 277 (2000).

[107] T. Kondo, R. Khasanov, T. Takeuchi, J. Schmalian, and A. Kaminski, Nature **457**, 296 (2009).

[108] C. P. Strehlow, M. Kończykowski, J. A. Murphy, S. Teknowijoyo, K. Cho, M. A. Tanatar, T. Kobayashi, S. Miyasaka, S. Tajima, and R. Prozorov, Phys. Rev. B **90**, 020508 (2014).

[109] Y. Mizukami, M. Konczykowski, Y. Kawamoto, S. Kurata, S. Kasahara, K. Hashimoto, V. Mishra, A. Kreisel, Y. Wang, P. J. Hirschfeld, Y. Matsuda, and T. Shibauchi, Nat. Commun. **5**, (2014).

[110] F. Schmitt, P. S. Kirchmann, U. Bovensiepen, R. G. Moore, L. Rettig, M. Krenz, J.-H. Chu, N. Ru, L. Perfetti, D. H. Lu, M. Wolf, I. R. Fisher, and Z.-X. Shen, Science **321**, 1649 (2008).

[111] J. C. Petersen, S. Kaiser, N. Dean, A. Simoncig, H. Y. Liu, A. L. Cavalieri, C. Cacho, I. C. E. Turcu, E. Springate, F. Frassetto, L. Poletto, S. S. Dhesi, H. Berger, and A. Cavalleri, Phys. Rev. Lett. **107**, 177402 (2011).

[112] J. Graf, C. Jozwiak, C. L. Smallwood, H. Eisaki, R. A. Kaindl, D.-H. Lee, and A. Lanzara, Nat. Phys. **7**, 805 (2011).

[113] J. C. Johannsen, S. Ulstrup, F. Cilento, A. Crepaldi, M. Zacchigna, C. Cacho, I. C. E. Turcu, E. Springate, F. Fromm, C. Raidel, T. Seyller, F. Parmigiani, M. Grioni, and P. Hofmann, Phys. Rev. Lett. **111**, 027403 (2013).

[114] S. Ulstrup, J. C. Johannsen, F. Cilento, J. A. Miwa, A. Crepaldi, M. Zacchigna, C. Cacho, R. Chapman, E. Springate, S. Mammadov, F. Fromm, C. Raidel, T. Seyller, F. Parmigiani, M. Grioni, P. D. C. King, and P. Hofmann, Phys. Rev. Lett. **112**, 257401 (2014).

[115] J. A. Sobota, S.-L. Yang, A. F. Kemper, J. J. Lee, F. T. Schmitt, W. Li, R. G. Moore, J. G. Analytis, I. R. Fisher, P. S. Kirchmann, T. P. Devereaux, and Z.-X. Shen, Phys. Rev. Lett. **111**, 136802 (2013).

[116] T. Yamamoto, Y. Ishida, R. Yoshida, M. Okawa, K. Okazaki, T. Kanai, A. Kikkawa, Y. Taguchi, T. Kiss, K. Ishizaka, N. Ishii, J. Itatani, S. Watanabe, Y. Tokura, T. Saitoh, and S. Shin, Phys. Rev. B **92**, 121106 (2015).

[117] P. C. Canfield and S. L. Bud'ko, Annu. Rev. Condens. Matter Phys. **1**, 27 (2010).

[118] D. Lu, I. M. Vishik, M. Yi, Y. Chen, R. G. Moore, and Z.-X. Shen, Annu. Rev. Condens. Matter Phys. **3**, 129 (2012).

[119] P. Dai, Rev. Mod. Phys. **87**, 855 (2015).

[120] M. Yi, D. H. Lu, J. G. Analytis, J.-H. Chu, S.-K. Mo, R.-H. He, M. Hashimoto, R. G. Moore, I. I. Mazin, D. J. Singh, Z. Hussain, I. R. Fisher, and Z.-X. Shen, Phys. Rev. B **80**, 174510 (2009).

[121] Y. R. Shen, *The principles of nonlinear optics* (Wiley-Interscience, Hoboken, 2003).

[122] K. Ishizaka, T. Kiss, T. Yamamoto, Y. Ishida, T. Saitoh, M. Matsunami, R. Eguchi, T. Ohtsuki, A. Kosuge, T. Kanai, M. Nohara, H. Takagi, S. Watanabe, and S. Shin, Phys. Rev. B **83**, 081104 (2011).

[123] Z. P. Yin, S. Lebègue, M. J. Han, B. P. Neal, S. Y. Savrasov, and W. E. Pickett, Phys. Rev. Lett. **101**, 047001 (2008).

[124] I. I. Mazin and M. D. Johannes, Nat. Phys. **5**, 141 (2009).

[125] T. Terashima, N. Kurita, M. Tomita, K. Kihou, C.-H. Lee, Y. Tomioka, T. Ito, A. Iyo, H. Eisaki, T. Liang, M. Nakajima, S. Ishida, S.-i. Uchida, H. Harima, and S. Uji, Phys. Rev. Lett. **107**, 176402 (2011).

[126] E. E. M. Chia, D. Talbayev, J.-X. Zhu, H. Q. Yuan, T. Park, J. D. Thompson, C. Panagopoulos, G. F. Chen, J. L. Luo, N. L. Wang, and A. J. Taylor, Phys. Rev. Lett. **104**, 027003 (2010).

[127] M. Sawicki, D. Chiba, A. Korbecka, Y. Nishitani, J. A. Majewski, F. Matsukura, T. Dietl, and H. Ohno, Nat. Phys. **6**, 22 (2010).

[128] H. Ohno, H. Munekata, T. Penney, S. von Molnár, and L. L. Chang, Phys. Rev. Lett. **68**, 2664 (1992).

[129] T. Jungwirth, Q. Niu, and A. H. MacDonald, Phys. Rev. Lett. **88**, 207208 (2002).

[130] G. Q. Zhao *et al.*, (unpublished).

[131] A. Hellmann, A. Löhken, A. Wurth, and A. Mewis, Z. Naturforsch. **62b**, (2007).

[132] J. P. Perdew, K. Burke, and M. Ernzerhof, Phys. Rev. Lett. **77**, 3865 (1996).

[133] J. P. Perdew, K. Burke, and M. Ernzerhof, Phys. Rev. Lett. **78**, 1396 (1997).

[134] Z. Xiao, H. Hiramatsu, S. Ueda, Y. Toda, F.-Y. Ran, J. Guo, H. Lei, S. Matsuishi, H. Hosono, and T. Kamiya, J. Am. Chem. Soc. **136**, 14959 (2014).

[135] F. Tran and P. Blaha, Phys. Rev. B **83**, 235118 (2011).

[136] J. P. Perdew, M. Ernzerhof, and K. Burke, J. Chem. Phys. **105**, 9982 (1996).

[137] I. Shein and A. Ivanovskii, J. Alloys Compd. **583**, 100 (2014).

[138] Y. Takeda, M. Kobayashi, T. Okane, T. Ohkochi, J. Okamoto, Y. Saitoh, K. Kobayashi, H. Yamagami, A. Fujimori, A. Tanaka, J. Okabayashi, M. Oshima, S. Ohya, P. N. Hai, and M. Tanaka, Phys. Rev. Lett. **100**, 247202 (2008).

[139] J. I. Hwang, M. Kobayashi, G. S. Song, A. Fujimori, A. Tanaka, Z. S. Yang, H. J. Lin, D. J. Huang, C. T. Chen, H. C. Jeon, and T. W. Kang, Appl. Phys. Lett. **91**, 072507 (2007).

[140] S. Andrieu, E. Foy, H. Fischer, M. Alnot, F. Chevrier, G. Krill, and M. Piecuch, Phys. Rev. B **58**, 8210 (1998).

[141] H. Suzuki, T. Yoshida, S. Ideta, G. Shibata, K. Ishigami, T. Kadono, A. Fujimori, M. Hashimoto, D. H. Lu, Z.-X. Shen, K. Ono, E. Sakai, H. Kumigashira, M. Matsuo, and T. Sasagawa, Phys. Rev. B **88**, 100501 (2013).

[142] T. Burnus, Z. Hu, H. H. Hsieh, V. L. J. Joly, P. A. Joy, M. W. Haverkort, H. Wu, A. Tanaka, H.-J. Lin, C. T. Chen, and L. H. Tjeng, Phys. Rev. B **77**, 125124 (2008).

[143] F. Gel'mukhanov and H. Ågren, Phys. Rep. **312**, 87 (1999).

[144] P. A. Brühwiler, O. Karis, and N. Mårtensson, Rev. Mod. Phys. **74**, 703 (2002).

[145] T. Berlijn, C.-H. Lin, W. Garber, and W. Ku, Phys. Rev. Lett. **108**, 207003 (2012).

[146] S. Ideta, T. Yoshida, M. Nakajima, W. Malaeb, T. Shimojima, K. Ishizaka, A. Fujimori, H. Kimigashira, K. Ono, K. Kihou, Y. Tomioka, C. H. Lee, A. Iyo, H. Eisaki, T. Ito, and S. Uchida, Phys. Rev. B **87**, 201110 (2013).

[147] O. Rader, C. Pampuch, A. M. Shikin, W. Gudat, J. Okabayashi, T. Mizokawa, A. Fujimori, T. Hayashi, M. Tanaka, A. Tanaka, and A. Kimura, Phys. Rev. B **69**, 075202 (2004).

[148] G. Levy, R. Sutarto, D. Chevrier, T. Regier, R. Blyth, J. Geck, S. Wurmehl, L. Harnagea, H. Wadati, T. Mizokawa, I. S. Elfimov, A. Damascelli, and G. A. Sawatzky, Phys. Rev. Lett. **109**, 077001 (2012).

[149] J.-J. Yeh and I. Lindau, At. Data Nucl. Data Tables **32**, (1985).

[150] H. Suzuki, K. Zhao, G. Shibata, Y. Takahashi, S. Sakamoto, K. Yoshimatsu, B. J. Chen, H. Kumigashira, F.-H. Chang, H.-J. Lin, D. J. Huang, C. T. Chen, B. Gu, S. Maekawa, Y. J. Uemura, C. Q. Jin, and A. Fujimori, Phys. Rev. B **91**, 140401 (2015).

[151] M. Kobayashi, I. Muneta, Y. Takeda, Y. Harada, A. Fujimori, J. Krempaský, T. Schmitt, S. Ohya, M. Tanaka, M. Oshima, and V. N. Strocov, Phys. Rev. B **89**, 205204 (2014).

[152] J. Okabayashi, T. Mizokawa, D. D. Sarma, A. Fujimori, T. Slupinski, A. Oiwa, and H. Munekata, Phys. Rev. B **65**, 161203 (2002).

[153] K. Hirakawa, S. Katsumoto, T. Hayashi, Y. Hashimoto, and Y. Iye, Phys. Rev. B **65**, 193312 (2002).

[154] K. Hirakawa, A. Oiwa, and H. Munekata, Physica E **10**, 215 (2001).

[155] J. K. Glasbrenner, I. Žutić, and I. I. Mazin, Phys. Rev. B **90**, 140403 (2014).

[156] A. Pandey, R. S. Dhaka, J. Lamsal, Y. Lee, V. K. Anand, A. Kreyssig, T. W. Heitmann, R. J. McQueeney, A. I. Goldman, B. N. Harmon, A. Kaminski, and D. C. Johnston, Phys. Rev. Lett. **108**, 087005 (2012).

[157] A. Pandey, B. G. Ueland, S. Yeninas, A. Kreyssig, A. Sapkota, Y. Zhao, J. S. Helton, J. W. Lynn, R. J. McQueeney, Y. Furukawa, A. I. Goldman, and D. C. Johnston, Phys. Rev. Lett. **111**, 047001 (2013).

[158] B. G. Ueland, A. Pandey, Y. Lee, A. Sapkota, Y. Choi, D. Haskel, R. A. Rosenberg, J. C. Lang, B. N. Harmon, D. C. Johnston, A. Kreyssig, and A. I. Goldman, Phys. Rev. Lett. **114**, 217001 (2015).

[159] B. T. Thole, P. Carra, F. Sette, and G. van der Laan, Phys. Rev. Lett. **68**, 1943 (1992).

[160] C. T. Chen, Y. U. Idzerda, H.-J. Lin, N. V. Smith, G. Meigs, E. Chaban, G. H. Ho, E. Pellegrin, and F. Sette, Phys. Rev. Lett. **75**, 152 (1995).

[161] M. Kobayashi, H. Niwa, Y. Takeda, A. Fujimori, Y. Senba, H. Ohashi, A. Tanaka, S. Ohya, N. Hai, P. M. Tanaka, Y. Harada, and M. Oshima, Phys. Rev. Lett. **112**, 107203 (2014).

[162] M. Taguchi, P. Krüger, J. C. Parlebas, and A. Kotani, Phys. Rev. B **73**, 125404 (2006).

[163] M. Blume, J. Appl. Phys. **57**, 3615 (1985).

[164] J. König, T. Jungwirth, and A. H. MacDonald, Phys. Rev. B **64**, 184423 (2001).

[165] J. König, H.-H. Lin, and A. H. MacDonald, Phys. Rev. Lett. **84**, 5628 (2000).

[166] J. König, H.-H. Lin, and A. H. MacDonald, Physica E **10**, 139 (2001).